

**Degradation of Estradiol in Water and Soil Using a New Class of Stabilized
Manganese Dioxide Nanoparticles and Hydrodechlorination of Triclosan Using
Supported Palladium Catalysts**

by

Bing Han

A dissertation submitted to the Graduate Faculty of
Auburn University
in partial fulfillment of the
requirements for the Degree of
Doctor of Philosophy

Auburn, Alabama
August 1, 2015

Keywords: Estradiol, Triclosan, Manganese dioxide nanoparticles,
Transport, In-situ degradation, Hydrodechlorination

Copyright 2015 by Bing Han

Approved by

Dongye Zhao, Chair, Professor of Civil Engineering
Mark O. Barnett, Professor of Civil Engineering
Prabhakar Clement, Professor of Civil Engineering
Yucheng Feng, Professor of Crop, Soil and Environmental Sciences
David Stanbury, Professor of Chemistry and Biochemistry

Abstract

Pharmaceuticals and personal care products (PPCPs), such as 17 β -estradiol (E2) and triclosan (TCS), are endocrine disruptors that have been found in surface water and groundwater. The low concentration of these endocrine disrupting chemicals can cause adverse effects on humans and wildlife via interactions with their endocrine system.

To facilitate in-situ remediation of E2 in groundwater, this research developed a new class of stabilized manganese oxide nanoparticles using “green” and low-cost carboxymethyl cellulose (CMC) as a stabilizer. The most mono-dispersed MnO₂ nanoparticles were obtained at a CMC/MnO₂ molar ratio of 1.39×10^{-3} , which yielded a mean hydrodynamic size of 39.5 ± 0.8 nm. The CMC-MnO₂ nanoparticles could effectively degrade E2 in both aqueous and soil phases. Column transport tests confirmed that the nanoparticles can be delivered through three natural sandy loams, although retention of the particles varied with soils. The particle retention is strongly dependent on injection pore velocity, and in-situ treatment effectiveness is strongly affected by the mass transfer rates of both the nanoparticles and contaminants. When the E2-laden soils were treated with 0.17 g/L of the MnO₂ nanoparticle suspension, 13-88% of water leachable E2 was degraded, depending on the soil type. The nanoparticles appear to be promising in terms of filling the technology gap for in-situ oxidation of endocrine disruptors in soil and groundwater.

This study also developed and tested a new class of supported Pd catalyst by immobilizing the Pd particles on two strong basic anion exchange resins (IRA-900 and

IRA-958). The resin-supported Pd catalysts could facilitate a rapid and complete hydrodechlorination (HDC) of TCS with very low concentration of chlorinated intermediates were present in the very early stage of HDC process. These resin supported catalysts showed long-term sustainability with only < 2% reactivity lost after eight exhausting runs, which contribute to the advantage of minimum Pd bleeding from the supports and high resistance to organic fouling. Catalytic HDC with resin-supported Pd catalysts have proved to be a promising solution for completely degrade the chlorinated pollutants and diminish highly toxic byproducts produced by other degradation methods.

Acknowledgments

I would like to express my sincere gratitude to my advisor Dr. Dongye Zhao, Elton Z. and Lois G. Huff Professor in Department of Civil Engineering at Auburn University, for his patient guidance, encouragement, and support throughout my PhD study as his student. I have been extremely lucky to have an advisor who has such immense professional knowledge, and who helped me to develop my skills to work independently. I gratefully acknowledge all the members of my committee, Dr. Mark Barnett, Dr. Prabhakar Clement, Dr. Yucheng Feng, and Dr. David Stanbury for their insightful comments and constructive suggestions through this work. Sincere appreciation is also to Dr. Yifen Wang, who served on the committee as the outside reader, and provided constructive criticism and great advice on this dissertation.

Best regards to all members of Dr. Zhao's research group for their friendship and helps. I gratefully acknowledge Dr. Clifford Lange and Mr. Jinling Zhuang for their patient help on GC analysis and other instruments operation in the lab. In addition, I would deeply appreciate for all my friends for their warmth to me and belief in me.

Finally, and the most important, I would like to thank my parents for their endless care, encouragement, and support to me in all my life. Their love accompanies with me to support me to succeed in finishing my PhD research work and made this dissertation possible.

Table of Contents

Abstract	ii
Acknowledgments.....	iv
List of Tables	ix
List of Figures	x
CHAPTER 1. BACKGROUND AND INTRODUCTION	1
1.1 The emergence of PPCPs in environment	1
1.2 The source and occurrence of E2 and TCS	5
1.3 Current treatment methods for PPCPs	7
1.3.1 Adsorption on activated carbon	7
1.3.2 Ozone oxidation	8
1.3.3 UV radiation	9
1.3.4 Electro-oxidation	10
1.3.5 Soil-aquifer treatment (SAT)	11
1.3.6 Microbial degradation	12
1.3.7 Nanoparticle remediation	12
CHAPTER 2. DEGRADATION OF AQUEOUS AND SOIL-SORBED ESTRADIOL USING A NEW CLASS OF STABILIZED MANGANESE OXIDE NANOPARTICLES.....	14
2.1 Introduction	14
2.2 Materials and methods	17

2.2.1 Materials	17
2.2.2 Preparation of CMC-stabilized MnO ₂ nanoparticles	20
2.2.3 Degradation of E2 in water	20
2.2.4 Soil sorption and desorption kinetics of E2	21
2.2.5 Degradation of soil-sorbed E2	23
2.2.6 Nanoparticle characterization	23
2.2.7 Analytical methods	24
2.3 Results and discussion	24
2.3.1 Effect of CMC/MnO ₂ molar ratio on particle size.....	24
2.3.2 Degradation of aqueous E2 with CMC-stabilized MnO ₂ nanoparticles	29
2.3.3 Effect of pH on E2 removal in water	40
2.3.4 Effect of CMC on E2 desorption from soil.....	41
2.3.5 Degradation of soil-sorbed E2	44
2.3.6 Effect of leachable soil components on E2 degradation.....	49
2.4 Conclusions.....	54
CHAPTER 3. IN-SITU DEGRADATION OF SOIL-SORBED 17β-ESTRADIOL USING CARBOXYMETHYL CELLULOSE STABILIZED MANGANESE OXIDE NANOPARTICLES: COLUMN STUDIES.....	56
3.1 Introduction.....	56
3.2 Materials and methods	60
3.2.1 Preparation and characterization of CMC-MnO ₂ nanoparticles	60
3.2.2 Soils and E2 sorption/desorption	60
3.2.3 Column transport tests	64
3.2.4 Column degradation tests.....	67

3.2.5 Analytical method.....	67
3.2.6 Transport modeling	68
3.3 Results and discussion	69
3.3.1 Characterization of CMC-stabilized MnO ₂ nanoparticles	69
3.3.2 Transport of CMC-MnO ₂ in three soils	71
3.3.3 Effect of flow velocity on transport behavior	79
3.3.4 Effect of nanoparticle concentration on transport behavior.....	82
3.3.5 Degradation of E2 in three soils.....	84
3.3.6 Effect of flow velocity on degradation behavior	91
3.3.7 Effect of particle concentration on degradation behavior.....	94
3.4 Conclusions.....	96
CHAPTER 4. CATALYTIC HYDRODECHLORINATION OF TRICLOSAN WITH ANION-EXCHANGE-RESIN SUPPORTED PALLADIUM.....	98
4.1 Introduction	98
4.2 Materials and methods	101
4.2.1 Materials	102
4.2.2 Catalyst preparation	104
4.2.3 Catalyst characterization.....	105
4.2.4 Catalytic hydrodechlorination of TCS.....	105
4.2.5 Catalyst lifetime.....	106
4.2.6 Analysis of hydrodechlorination byproducts	107
4.2.7 Analysis of Cl balance	107
4.3 Results and discussion	108

4.3.1 Catalysts characterization	108
4.3.2 Effect of Pd loading on the rate of hydrodechlorination reaction	114
4.3.3 Effect of support on the rate of TCS adsorption and reaction	119
4.3.4 Lifetime of the catalyst	122
4.3.5 Effect of humic acid.....	125
4.3.6 Hydrodechlorination pathway of TCS in liquid phase	128
4.4 Conclusions.....	133
CHAPTER 5. CONCLUSIONS AND SUGGESTIONS FOR FUTURE RESEARCH .	135
5.1 Summary and conclusions	135
5.2 Suggestions for future work	138
References	141
APPENDIX A.	160

List of Tables

Table 2-1. Physical and chemical properties of the soil used in this work	19
Table 2-2. CMC surface density on MnO ₂	36
Table 2-3. Retarded rate model parameters	37
Table 3-1. Physical and chemical properties of the three soils used in this work	63
Table 3-2. Experiment conditions of MnO ₂ transport tests conducted at various velocities and concentrations in saturated columns packed with different porous media	65
Table 3-3. Simulation parameters obtained by fitting breakthrough curves of column experiments to the model	75
Table 3-4. Degradation efficiency of CMC-MnO ₂ treated columns	87
Table 4-1. Salient properties of ion exchange resins used in this study	103
Table 4-2. Reaction rate constants for HDC of TCS catalyzed by resin supported Pd ...	117

List of Figures

Figure 1-1. Structure of 17 β -estradiol (E2) and triclosan (TCS)	4
Figure 2-1. (a) Hydrodynamic size distribution and mean hydrodynamic diameter of MnO ₂ nanoparticles prepared at various CMC:MnO ₂ molar ratios; (b) MnO ₂ stability measured as normalized Mn concentration (C/C ₀) as a function of time through sedimentation tests.....	27
Figure 2-2. Photographs and TEM images of: a) non-stabilized MnO ₂ , and b) CMC-stabilized MnO ₂ particles. Pictures were taken 30 minutes after synthesis. [MnO ₂] = 8 \times 10 ⁻⁴ M (0.07 g/L) for both cases, and CMC/MnO ₂ molar ratio = 1.39 \times 10 ⁻³ for case b)	28
Figure 2-3. a) Oxidative degradation of E2 in water by MnO ₂ particles prepared in the presence of various concentrations of CMC and at a fixed MnO ₂ dosage of 2 \times 10 ⁻⁵ M. b) Linearized first-order plot for non-stabilized and CMC-stabilized degradation rate data.	31
Figure 2-4. Batch kinetic profiles of E2 degradation in consecutive spikes of E2 using the same MnO ₂ : a) non-stabilized MnO ₂ ; b) CMC-stabilized MnO ₂	32
Figure 2-5. Effect of pH on oxidative removal of E2 in water by: a) Non-stabilized MnO ₂ , and b) CMC-stabilized MnO ₂	38
Figure 2-6. Comparing E2 removal rates of non-stabilized and CMC-stabilized MnO ₂ particles at pH 5, 6, 7, and 8.	39
Figure 2-7. a) E2 sorption kinetics with a sandy loam soil (initial aqueous [E2] = 4 \times 10 ⁻⁶ M). b) Effect of CMC on desorption of E2 from the soil. In figure b) M _t : E2 remaining in soil at time t.	43
Figure 2-8. Degradation of aqueous and soil-sorbed E2 at various dosages (2 \times 10 ⁻⁵ to 2 \times 10 ⁻⁴ M) of MnO ₂	45
Figure 2-9. Degradation of soil-sorbed E2 with bare and CMC-stabilized MnO ₂ particles: a) in the whole system, and b) in the aqueous phase	47
Figure 2-10. Zeta potential of three different suspensions containing: soil exudates, non-stabilized MnO ₂ and CMC-stabilized MnO ₂ , respectively	48

Figure 2-11. Oxidation kinetics of E2 in water with or without soil extracts: a) non-stabilized MnO ₂ , and b) CMC-stabilized MnO ₂	51
Figure 2-12. Degradation of E2 in water by CMC-stabilized and non-stabilized MnO ₂ in the presence of added cations: a) [Mn ²⁺] = 0.01 M, and b) [Ca ²⁺] = 0.01 M.	52
Figure 2-13. Degradation of E2 in water by CMC-stabilized and non-stabilized MnO ₂ in the presence of humic acid (HA): a) non-stabilized MnO ₂ , and b) CMC-stabilized MnO ₂	53
Figure 3-1. Column experiment setup.	66
Figure 3-2. Photographs and TEM images of: (a) non-stabilized MnO ₂ , and (b) CMC-stabilized MnO ₂ particles.	70
Figure 3-3. Measured and fitted breakthrough curves of a KBr tracer and CMC-MnO ₂ nanoparticles through: (a) SL1 soil, (b) SL2 soil, (c) SL3 soil, and nanoparticle retention profiles (c) obtained after MnO ₂ transport through the three soils.	76
Figure 3-4. Measured duplicate breakthrough curves of CMC-MnO ₂ nanoparticles through: (a) SL1 soil, (b) SL2 soil, and (c) SL3 soil.	77
Figure 3-5. MnO ₂ sorption kinetics in three soils.	78
Figure 3-6. Breakthrough curves of CMC-MnO ₂ nanoparticles through SL2 soil at different pore velocities.	81
Figure 3-7. Breakthrough curves of different concentrations of CMC-MnO ₂ nanoparticles through SL2 soil.	83
Figure 3-8. Elution histories of E2 from soils when subjected to a background CMC solution and a suspension of CMC-MnO ₂ nanoparticles: (a) SL1 soil (E2 = 0.0019 mg-E2/g-soil), (b) SL2 soil (E2 = 0.0065 mg-E2/g-soil), and (c) SL3 soil (E2 = 0.0104 mg-E2/g-soil).	88
Figure 3-9. Duplicate of elution histories of E2 from SL2 soil when subjected to a background CMC solution and a suspension of CMC-MnO ₂ nanoparticles.	89
Figure 3-10. E2 (a) sorption kinetics with three soils (initial aqueous [E2] = 4×10 ⁻⁶ M), and successive desorption kinetics in (b) SL1 soil, (c) SL2 soil, and (d) SL3 soils.	90
Figure 3-11. Elution histories of E2 from SL2 soil at different MnO ₂ injection pore velocities.	93

Figure 3-12. Elution histories of E2 from SL2 soil under different MnO ₂ injection concentrations.	95
Figure 4-1. XRD patterns of bare resins, freshly prepared resin-supported Pd catalysts, and used catalysts after 8 consecutive runs of HDC of TCS. Bragg angles (2θ) from 30° to 80° were scanned at scan rate of 4°/min.	111
Figure 4-2. SEM images of resin-supported Pd catalysts: cross-section of (a) IRA-900 and (b) IRA-958 at low magnification, and internal of (c) IRA-900 and (d) IRA-958 at high magnification.	112
Figure 4-3. Radial distribution of Pd at the cross-section of the (a) IRA-900 and (b) IRA-958 analyzed by EDXS. The R/R ₀ >0 and R/R ₀ <0 scanning positions are along the radius in right and upper direction shown in Figure 4-2. Pd distribution was plotted as Pd to Cl atomic percentage.	113
Figure 4-4. Kinetic profiles of catalytic HDC of TCS with different Pd loadings on resin (a) IRA-900 and (b) IRA-958, and linearized pseudo first-order plot for (c) IRA-900 and (d) IRA-958.	118
Figure 4-5. TCS adsorbed and degraded in the process of catalytic HDC with (a) 0.2 wt.% Pd/IRA-900, (b) 0.2 wt.% Pd/IRA-958, (c) 2.0 wt.% Pd/IRA-900, and (d) comparison of the degradation rate of TCS over catalysts of 0.2 wt.% Pd loading on two resins.	121
Figure 4-6. Catalytic HDC of TCS in eight consecutive batch tests where the Pd catalysts supported on resins (a) IRA-900 and (b) IRA-958 were repeatedly used, and linearized pseudo first-order plot for (c) IRA-900 and (d) IRA-958.	124
Figure 4-7. HDC of TCS using resin (a) IRA-900 and (b) IRA-958 supported Pd catalysts in the presence of various concentrations of humic acid, and HDC of TCS using (c) Pd/IRA-900 and (d) Pd/IRA-958 supported catalysts in presence of 30 mg/L TOC through six consecutive runs.	127
Figure 4-8. GC/MS chromatogram of TCS HDC byproducts.	130
Figure 4-9. Schematic representation for catalytic HDC of TCS.	131
Figure 4-10. Concentration histories of Cl ⁻ in aqueous phase, Cl ⁻ adsorbed on resins, and TCS-Cl (i.e., TCS-bounded Cl) during HDC of TCS using IRA-958 supported Pd catalysts.	132

CHAPTER 1. BACKGROUND AND INTRODUCTION

1.1 The emergence of PPCPs in environment

Over the last decades, pharmaceuticals and personal care products (PPCPs) have been receiving increasing attention due to their widespread usage and continuous release into the environment (Jiang et al., 2013; Kasprzyk-Hordern et al., 2009; Ternes, 1998). The most common PPCPs include anti-inflammatories, antibiotics, cardiovascular pharmaceuticals, antiepileptic drugs, and hormonal compounds. PPCPs are considered as emerging pollutants because as analytical technology improves, the ability to detect contaminants in water at very low concentration has improved. This has brought these contaminants into public view, recently. In addition, these contaminants still remain unregulated or are currently undergoing a regularization process (Pal et al., 2010). The increasing attention to PPCPs has induced interests to investigate the source, behavior, fate, risk, and control of such emerging pollutants (Drewes et al., 2003; Khanal et al., 2006; Pal et al., 2010).

Most PPCPs are known to have biological effects, but only limited information has been obtained by quantifying their potential ecotoxicological impacts. One typical approach is to conduct toxicity tests using various organisms, for instance, fish, invertebrates, algae, and also human embryonic cells (Pal et al., 2010). The sex hormones including endogenous estrone (E1), 17 β -estradiol (E2), estriol (E3), as well as synthetic 17 α -ethinylestradiol (EE2) are generally viewed to be of utmost concern (Kolpin et al., 2002; Shore and Shemesh, 2003; Diamanti-Kandarakis et al., 2009). Their associated

adverse effects include abnormal development (e.g., malformations, sex reversal in male species), reproductive disorders (e.g., declines in the quality and quantity of sperm production), and cancers (e.g., breast, prostate, and testicular).

Other PPCPs, such as antibiotics, cardiovascular drugs, and antineoplastics were also proven to have ecotoxicological effects. One of the most commonly used broad-spectrum antimicrobials, triclosan (5-chloro-2-(2,4-dichlorophenoxy)phenol, TCS), is concerned as an endocrine disrupting chemical and reported to have adverse effects on thyroid hormone homeostasis (Veldhoen et al., 2006). Moreover, TCS, which was found to accumulate in various aquatic organisms, is highly toxic to certain types of algae and fish (Orvos et al. 2002; Ishibashi et al., 2004). As an antibacterial, TCS may induce the bacterial resistance development (McMurry et al., 1998; Halden et al., 2014). Of particular concern is sewage sludge, where an abundance of pathogens and multiple antimicrobials coexist creating a large risk of drug resistance for the pathogens.

In this research, the focus was aimed toward 17β -estradiol (E2, $C_{18}H_{24}O_2$), a naturally produced steroid hormone, and triclosan (TCS, $C_{12}H_7Cl_3O_2$), a broad-spectrum antimicrobial. The molecular structures of both E2 and TCS are shown in **Figure 1-1**. E2 is the major concern within steroid hormone research because it exerts physiological effects at a lower concentration than other steroid hormones. E2 can be detected above their lowest observable effect level (LOEL) for fish (10 ng/L) in the environment (Shore and Shemesh, 2003). TCS is one of the worldwide largest consumed PPCPs, which is used as a preservative or an antiseptic agent in many personal care (e.g., toothpaste, soaps, deodorants, shampoos, and cosmetics) and household (e.g., plastic additives) products. TCS annual usage has been estimated higher than 300 t in the USA and 450 t in the

Europe (Halden and Paull, 2005; SCCS, 2010). TCS is an authorized ingredient used in cosmetic products and other household products in USA and Europe (Bedoux, et al., 2012).

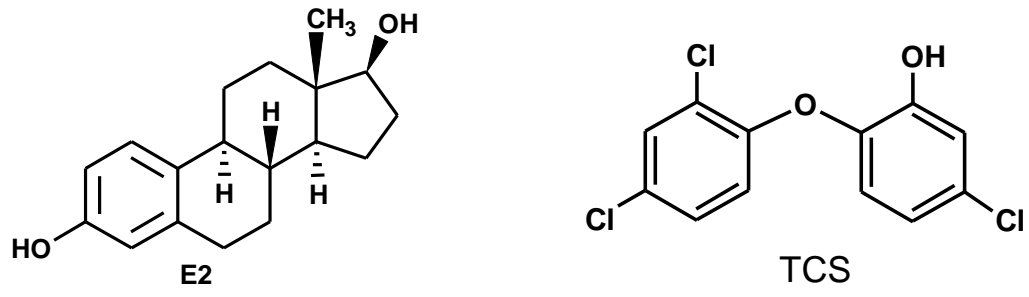


Figure 1-1. Structure of 17β-estradiol (E2) and triclosan (TCS)

1.2 The source and occurrence of E2 and TCS

PPCPs are frequently detected in waste water treatment plant effluent (WWTP) and in sewage treatment plants (STP), surface water and groundwater. Generally, the concentration of pharmaceuticals decreases from the effluent of WWTP/STP to the freshwater and groundwater (Li, 2014). This may be due to pharmaceuticals that are concentrated in WWTP/STP and the current waste water treatment could not effectively remove these contaminants. In freshwater, natural processes, such as photolysis, sorption, volatilization, and dispersion can occur to attenuate pharmaceuticals. Moreover, in groundwater, after the sand filtration, sorption, and microbiology degradation, the concentration of pharmaceuticals can be lowered (Li, 2014).

Municipal wastewater is considered one of the main sources of hormones in aquatic systems (Ternes et al., 1999), and the land application of animal wastes releases significant amounts of hormones into soil and groundwater (Shore and Shemesh, 2003). The U.S. Geological Survey reported that various reproductive hormones were detected in 40% of the 139 streams across 30 states (Kolpin et al., 2002), with maximum and median concentrations of 93 ng/L and 9 ng/L for E2, respectively. The maximum effluent concentration in German and Canadian sewage treatment plant ranged from 3 ng/L to 64 ng/L for E2 (Ternes et al., 1999). Poultry litters contain substantial amounts of estrogen and testosterone. Shore and Shemesh (2003) reported that the average concentrations of estrogen and testosterone in laying hen litter were 533 µg/kg and 254 µg/kg, respectively. The land application of broiler litter has been found to greatly increase the E2 concentration in soil to 675 ng/kg from a background value of 55 ng/kg (Finlay-Moore et

al., 2000). Shore and Shemesh (2003) also reported that leachates from chicken manure stockpiles contained 730 ng/L of estrogen and 630 ng/L of testosterone.

Most hormones are detected at very low concentrations in groundwater due to their easily binding to soil; however, low concentration of estrogens were reported to break through porous media and release into groundwater, causing long-term threats to ecosystems. Kolodziej et al. (2004) detected 6.3 ng/L of E2 in a monitoring well located downstream of a waste lagoon. The analysis of 112 samples in 59 groundwater sites in Austria detected E2 in more than 50% of the samples with a maximum concentration of 0.79 ng/L (Hohenblum et al., 2004). Following rainfall, a large amount of estrogens were found in the runoff from field discharges. Nichols et al. (1998) reported 1-3 µg/L of estrogen and testosterone in rainwater runoff.

As a pharmaceuticals and personal care products (PPCPs) ingredient, substantial amounts of TCS were discharged into WWTPs. Studies on the fate of TCS during wastewater treatment indicate that substantial TCS can be removed by wastewater treatment plants with a high efficiency of 80%-96% (Bester, 2003; Winkler et al., 2007). However, residues of TCS are still detected in effluents, leading to discharge in surface water. The U.S. Geological Survey reported that TCS was among the seven most frequently detected organic contaminants in 139 streams sampled across 30 states with the median concentration of 0.14 µg/L (Kolpin et al., 2002). In addition, the removed TCS by activated sludge was not degraded by biomass, the antimicrobials distribute themselves into carbon- and lipid-rich sewage sludge, and accumulate in the biosolids (Winkler et al., 2007; Heidler, 2007). In 2004, over seven million tons of biosolids were generated in US, and more than 55% of which were land applied in agricultural soils

(McClellan and Halden, 2010). Consequently, an excess amount of TCS were released into the soil and groundwater through biosolid application.

A US EPA National Sewage Sludge Survey reported TCS was also the most abundant PPCP in 110 biosolids samples collected from WWTPs across 32 states with its mean concentration of 12.6 mg/kg (McClellan and Halden, 2010). Biosolids application is the main source of TCS occurrence in soil and groundwater. TCS has been found relatively persistent in agricultural soil after biosolids amendment. Lozano et al. (2010) observed a half-life of 107.4 days for TCS in a biosolids applied agricultural field. Barnes et al. (2008) detected TCS in 14.9 % of 47 groundwater sites in US. Data from UK Environmental Agency show that out of 22 monitored groundwater sites, 100% contained TCS, and the maximum concentration was detected to be 2.11 $\mu\text{g/L}$ (Stuart et al., 2012).

1.3 Current treatment methods for PPCPs

1.3.1 Adsorption on activated carbon

Adsorption by activated carbons (AC) is commonly used for controlling taste and odor in drinking water. This technology has been proven to be effective in removing micropollutants and antibiotics (Ji et al., 2010; Mestre et al., 2014). There are numerous studies on the adsorption mechanisms of aromatic compounds by AC, such as the following, have been proposed: 1) dispersive interactions between π electrons of the aromatic ring and π electrons of the graphene planes, 2) coupling of the aromatic ring of the organic compound function as π -electron-acceptor with the highly polarized graphene surface function as π -electron-donor to form electron-donor-acceptor (EDA) interactions, 3) electrostatic interactions and formation of hydrogen bonds (Rivera-Utrilla et al., 2013). Due to various types of compounds being involved in the adsorption process, it is not

possible to give a general adsorption mechanism. Ji et al. (2010) studied adsorption of three antibiotics, sulfamethoxazole, tetracycline, and tylosin on synthesized micro- and mesoporous carbons and commercial microporous AC, and found the antibiotic molecule size and AC pore size, shape and structure are important factors to affect adsorption kinetics and isotherms. It was also found among the three antibiotics tested, that tetracycline obtained the strongest adsorption on AC. This result was attributed to the multiple adsorption sites (phenol, enone, and protonated amino) in the tetracycline molecule. Furthermore, Mendez-Diaz et al. (2010) studied the kinetics of adsorption of three nitroimidazole antibiotics on three ACs and found hydrophobic interactions appeared to govern the kinetics of the adsorption process.

1.3.2 Ozone oxidation

The recent interests in using ozone oxidative removal of pharmaceuticals includes application of O_3 , O_3/OH^\cdot and O_3/H_2O_2 (Huber et al., 2003; Rosal et al., 2008). Huber et al. (2003) investigated the oxidation of pharmaceuticals during conventional ozonation and advanced oxidation process (AOPs), which was based on the generation of free radicals ($\cdot OH$). Among the selected pharmaceuticals (bezafibrate, carbamazepine, diazepam, diclofenac, 17α -ethinylestradiol, ibuprofen, iopromide, sulfamethoxazole, and roxithromycin), it is found that some of the named analgesics can be completely transformed during conventional process with the second order rate constant $k_{O_3} > 5 \times 10^4 \text{ M}^{-1}\text{s}^{-1}$, while other pharmaceuticals cannot, such as diazepam ($k_{O_3} = 0.75 \pm 0.15 \text{ M}^{-1}\text{s}^{-1}$), ibuprofen ($k_{O_3} = 9.6 \pm 1.0 \text{ M}^{-1}\text{s}^{-1}$), and iopromide ($k_{O_3} < 0.8 \text{ M}^{-1}\text{s}^{-1}$). When the free radical $\cdot OH$ is involved, the rate constants k_{OH} range from 3.3 to $9.8 \times 10^9 \text{ M}^{-1}\text{s}^{-1}$, which is about two or three times faster than conventional ozonation. Rosal et al. (2008)

investigated the mineralization of wastewater from the secondary clarifier of urban and domestic WWTP. When using ozone in alkaline conditions (O_3/OH^- pH at 8), a TOC decay of 15% was obtained. Conversely, when injecting hydrogen peroxide (O_3/H_2O_2), which is AOP, the degree of mineralization reached over 90%. The results indicated the highly reactive hydroxyl radical ($\cdot OH$) can successfully attack numerous pharmaceutical molecules and achieve effective removal.

1.3.3 UV radiation

High efficiency oxidative removal of organic compounds using hydroxyl radicals has attracted researchers' interests to explore photochemical degradation. In nature, many organic compounds can decompose via photochemical reaction under solar light. The most widely used wavelength for photolysis is 200-400 nm, which falls in the ultraviolet spectrum region (Rivera-Utrilla et al., 2013). Some compounds are degraded by direct photolysis as the molecules absorb a certain type of radiation and reach an excited state, while other compounds are degraded by radical generation, known as indirect photolysis (Rivera-Utrilla et al., 2013).

Most pharmaceuticals are photolytic, as they generally contain aromatic rings, heteroatoms, and other functional groups that allow absorption of solar radiation to conduct photodegradation (Puma et al., 2010; Rosenfeldt and Linden, 2004; Ryan et al., 2011). Ryan et al. (2011) studied the photolysis of two antibiotics (sulfamethoxazole and trimethoprim) in wastewater treatment plant effluent. They suggested sulfamethoxazole and trimethoprim removal was enhanced in wastewater effluent, due to indirect photolysis. In the wastewater effluents, photolysis can be divided into direct photolysis (48% removal for sulfamethoxazole, 18% removal for trimethoprim), reaction with

hydroxyl radicals (36% and 62% for sulfamethoxazole and trimethoprim, respectively), and reaction with triplet excited effluent organic matter (16% and 20% for sulfamethoxazole and trimethoprim, respectively). Rosenfeldt and Linden (2004) investigated the degradation of three endocrine disrupting chemicals (EDCs), bisphenol A, ethinyl estradiol, and E2 by UV radiation photolysis and the UV/H₂O₂ AOP. They used both monochromatic low-pressure (LP) UV lamps and polychromatic medium-pressure (MP) UV lamps for the photolysis, and found that polychromatic MP UV radiation was more effective for direct photolysis than conventional LP VU lamps. In all cases, the EDCs were more effectively degraded using UV/H₂O₂ than direct UV photolysis treatment. Lin and Reinhard (2005) found a common anti-inflammatory medication, naproxen, can be photodegraded. However, degradation products are more toxic than original naproxen. In addition, the antibiotic triclosan and triclocarban were also found to produce highly toxic byproducts such as chlorodioxins and chloroanilines under sunlight (Aranami and Readman, 2007).

1.3.4 Electro-oxidation

Currently, one of the most popular oxidation techniques for wastewater treatment is electrochemical oxidation. This technique usually treats the pollutants in an electrolytic cell by: 1) direct electron transfer to the anode, and 2) indirect oxidation with heterogeneous radicals formed from water decompose at the anode, such as ·OH radical, and active oxygen.

For water treatment, the only disadvantage of electro-oxidation is the high energy requirement. Usually, high cell voltages are a prerequisite to achieve oxidation of both pollutants and water, maintaining the anode activity. The anode material has an important

influence on the selectivity and efficiency of the process which will result in either electrochemical conversion or electrochemical combustion. The electrochemical conversion is to transform the original organic pollutants into higher oxidative compounds by chemisorbed active oxygen. The electrochemical combustion could mineralize the organic pollutants by physisorbed $\cdot\text{OH}$.

Feng et al. (2010) used Ti/SnO_2 as an anode to electro-oxidative degradation of 17α -ethinylestradiol, conducting at 60 mA for 480 min, and achieved a 79% of 17α -ethinylestradiol removal. Yoshihara and Murugananthan (2009) studied E2 electro-oxidation on boron-doped diamond anode with a 350 mA electric current for 270 min, and detected almost 94 % of the initial E2 was transformed.

1.3.5 Soil-aquifer treatment (SAT)

The use of secondary or tertiary treated waste water effluent to recharge ground water is known as soil-aquifer treatment (SAT) (Mansell and Drewes, 2004). SAT is a way to solve the water shortage problem by pumping reclaimed wastewater from recovery wells near the recharge area and delivering to the arid part of the country for unrestricted agricultural irrigation (Arye et al., 2011). SAT removes of organic contaminants, nutrients, and pathogens through physical filtration, adsorption to soil particles, microbial biotransformation, and dilution with groundwater (Laws et al., 2011). SAT attracts more interests from researchers because it requires minimal energy and chemical input, as well as it replenishes groundwater supplies, particularly in arid and semiarid regions (Mansell and Drewes, 2004). Arye et al. (2011) investigated fate and transport of carbamazepine (CBZ) in SAT in Israel. The results showed adsorption and filtration of CBZ only occurred in the upper soil layers (0-25 cm), but not in the deeper

layers (25-150 cm). The monitoring well analysis revealed the concentration of CBZ decreased from 1094 ± 166 ng/L to 560 ± 175 ng/L after the SAT. Laws et al. (2011) studied the attenuation of 17 contaminants of emerging concern (CECs) during a surface-spreading aquifer recharge and found the concentration of all compounds were reduced after SAT, with 11 of the compounds attenuated by $> 80\%$ after 60 days of travel.

1.3.6 Microbial degradation

The potential of PPCPs to undergo biotransformation is an important pathway for them to “self-degrade” in environment. Biodegradation of PPCP compounds may have following pathways: 1) mineralization, 2) transformation to more hydrophobic compounds, which partition onto the soil, and 3) transformation to more hydrophilic compounds, which remain in the groundwater. To date, most of the studies on biodegradation of PPCPs mainly focus on laboratory studies to identify the possible biodegradation pathways for PPCPs removal (Onesios et al., 2009).

The laboratory studies of PPCP removal often result in discrepant removal efficiencies, and the influential conditions include PPCPs concentrations, primary substrate concentrations, incubation times, and microbial inoculum sources (Onesios et al., 2009). For instance, a study on biodegradation of an anticancer drug, 5-fluorouracil, with an initial concentration > 800 mg/L, yielded a removal of 2% (Kummerer and Al-Ahmad, 1997), whereas another study on the same chemical with a starting concentration > 50 μ g/L, achieved a 50% removal (Yu et al, 2006).

1.3.7 Nanoparticle remediation

Recently, application of nanoparticles for in-situ remediation of soil/groundwater has attracted significant interests. The application of nanoparticles in the environmental

field offers many advantages for in-situ remediation. First, nano-scale particles have larger surface area, thus offering more reactive sites for binding to target compounds. Because many environmental reactions (e.g. sorption, redox, ion exchange) with particles' participation are a surface-mediated process, increasing the surface area will thus increase the reaction rate and reduce remediation time. Second, nanoparticles have high transport capacity and can easily gain access to contaminant plumes deep in the ground or underneath built infrastructures, and thus, potentially reduce remediation cost. Third, injection of nanoparticles to contaminated zones is a process easy controllable and known for causation of less environmental disruption.

Similar to biodegradation, nanoparticle technology has been used in laboratory tests to degrade PPCPs (Joo and Zhao, 2008). However, no studies have been done to apply in field remediation. The most mature in-situ application is to use zero valent iron (ZVI) for remediation of chlorinated solvents (Bennett, et al., 2010; He et al., 2010; Wei et al., 2010).

**CHAPTER 2. DEGRADATION OF AQUEOUS AND SOIL-SORBED
ESTRADIOL USING A NEW CLASS OF STABILIZED MANGANESE OXIDE
NANOPARTICLES***

2.1 Introduction

Endocrine disrupting chemicals (EDCs) have been known to interfere with hormonal and homeostatic system functions (Diamanti-Kandarakis et al., 2009). In recent years, there has been a growing interest in steroidal estrogen hormones as they have been widely detected in surface and ground waters (Kolpin et al., 2002). Of particular environmental concern are endogenous estrone (E1), 17 β -estradiol (E2), and estriol (E3) released with human and animal wastes, as well as synthetic 17 α -ethinylestradiol (EE2) (Kolpin et al., 2002; Shore and Shemesh, 2003). The associated adverse effects include abnormal development (e.g., malformations, sex reversal in male species), reproductive disorders, and cancers (Diamanti-Kandarakis et al., 2009). Exposure to trace concentrations (even at ng/L) of hormones can result in serious physiological consequences for some aquatic lives. For instance, the male Japanese medaka was found to produce female specific proteins when exposed to E2 at 5 ng/L (Tabata et al., 2001).

Municipal wastewater is considered one of the main sources of hormones in the aquatic systems (Ternes et al., 1999), and the land application of animal wastes releases significant amounts of hormones into soil and groundwater (Shore and Shemesh, 2003).

* This chapter was published as Han et al., 2015. Permission for reuse in dissertation has been obtained from Elsevier.

The U.S. Geological Survey reported that various reproductive hormones were detected in 40% of the 139 streams across 30 states (Kolpin et al., 2002), with maximum and median concentrations of 93 and 9 ng/L for E2, respectively. The maximum effluent concentration in a German and Canadian sewage treatment plant ranged from 3 to 64 ng/L for E2 (Ternes et al., 1999). Poultry litters contain substantial amounts of estrogen and testosterone. Shore and Shemesh (2003) reported that the average concentrations of estrogen and testosterone in laying hen litter were 533 $\mu\text{g}/\text{kg}$ and 254 $\mu\text{g}/\text{kg}$, respectively. The land application of broiler litter has been found to greatly increase the E2 concentration in soil to 675 ng/kg from a background value of 55 ng/kg (Finlay-Moore et al., 2000). Shore and Shemesh (2003) also reported that leachates from chicken manure stockpiles contained 730 ng/L of estrogen and 630 ng/L of testosterone.

To mitigate the health and environmental impacts, researchers have explored various treatment processes to degrade these emerging contaminants, including ozonation, UV radiation, and chemical oxidation (Huber et al., 2003; Jiang et al., 2009; Rosenfeldt and Linden, 2004). Yet, knowledge has been lacking on degradation of soil-sorbed estrogen.

The conventional MnO_2 is typically a porous particulate material, which has a specific surface area from dozens to hundreds of m^2/g and a low pH of point of zero charge (PZC) of 2.25 (Murray, 1974). MnO_2 has been known to be an oxidizing agent effective for a range of organic contaminants (Clarke and Johnson, 2010; Lin et al., 2009; Zhang and Huang, 2003), and has been shown to be promising for estrogen degradation in water (Jiang et al., 2009; Xu et al., 2008). E2 oxidation by MnO_2 has been known to

proceed via Eqs. (2-1) and (2-2) to give estrone (E1) and 2-hydroxyestradiol (Jiang et al., 2009):



The oxidative transformation was shown to lower the estrogenic activities of the parent E2 (Jiang et al., 2010; Xu et al., 2008). Typically, the process involves a first rapid adsorption of the solutes on the particle surface followed by the oxidation reaction. Consequently, the degradation effectiveness can be influenced by factors that affect adsorption and reactivity of MnO₂, such as particle size, surface area, surface charge, and accessibility of the reactive sites. In addition, environmental factors (e.g. pH, temperature and co-solutes) also influence the oxidation power of MnO₂ (Xu et al., 2008; Zhang and Huang, 2003). Mashtare et al. (2011) reported that E2 strongly binds to soil, forming soil-bound residues, and E2 sorption is correlated to the soil organic carbon with a high log*K*_{OC} of 3.14±0.16. Lee et al. (2003) studied sorption and dissipation of testosterone, E2, and EE2 in soil and sediment, and found that the hormones can be transformed in aerobic soil and sediment slurries. Sheng et al. (2009) reported MnO₂ minerals in natural soil were responsible for dissipation of E2, indicating that MnO₂ holds the potential for degradation of soil-sorbed E2. In general, soil-adsorption limits the chemical availability and degradation rate, and various soil exudates may inhibit the reactivity of nanoparticles (Zhang et al., 2011).

Laboratory and field experiments have shown that stabilized nanoparticles can be delivered in soil and facilitate in-situ remediation of contaminated soil and groundwater by direct injection of the nanoparticles into contaminated source zones (e.g., He and Zhao,

2005; 2007; He et al., 2007; 2009; 2010; Xiong et al., 2009). He et al. (2009; 2010) tested the soil transportability of carboxymethyl cellulose (CMC) stabilized zero-valent iron (ZVI) nanoparticles through bench-scale and field experiments. They observed that the stabilized nanoparticles can be directly injected into a sandy aquifer (hydraulic conductivity 1.98×10^{-3} cm/s) under field conditions at an injection pressure less than 5 psi. They found that for a given soil, the maximum travel distance is a function of the injection pressure, and the delivered nanoparticles become virtually immobile under natural groundwater flow conditions. The delivered nanoparticles were able to effectively degrade soil-sorbed TCE and PCE in the aquifer (He et al., 2010; Su et al., 2012). To facilitate in-situ degradation of soil-sorbed E2 in aquifers, the desired MnO₂ nanoparticles will need to meet some key criteria: 1) they must be soil deliverable, 2) they must be reactive toward the target contaminants, and 3) they must be environmental friendly.

The overall goal of this work was to develop and test a new class of stabilized MnO₂ nanoparticles toward in-situ oxidation of soil-sorbed E2. The specific objectives were to: 1) Synthesize and characterize a new class of stabilized MnO₂ nanoparticles using CMC as a stabilizer, 2) Test the effectiveness of the nanoparticles for oxidation of aqueous and soil-sorbed E2, 3) Determine the effects of pH, CMC concentration, soil exudates on oxidation of E2, and elucidate the underlying mechanisms, and 4) Demonstrate the soil transportability of the nanoparticles.

2.2 Materials and methods

2.2.1 Materials

The following chemicals of analytical or higher grade were used as received: 17 β -estradiol (C₁₈H₂₄O₂, E2, purity >97%, Spectrum Chemical Mfg Corp., New Brunswick, NJ, USA), manganese chloride tetrahydrate (MnCl₂·4H₂O, Alfa Aesar, Ward Hill, MA, USA), potassium permanganate (KMnO₄, Acros Organics, Morris Plains, NJ, USA), sodium carboxymethyl cellulose (M.W. = 90,000, Acros Organics), sodium acetate trihydrate (C₂H₃NaO₂·3H₂O, Mallinckrodt Pharmaceuticals, St. Louis, MO, USA) and sodium phosphate monobasic monohydrate (NaH₂PO₄·H₂O, Fisher scientific, Fairlawn, NJ, USA). Methanol (CH₄O, Alfa Aesar), acetonitrile (CH₃CN, EMD Millipore, Billerica, MA, USA) and acetic acid glacial (C₂H₄O₂, EMD Millipore) were of HPLC grade (>99% purity). A stock solution of 17 β -estradiol was prepared at 5×10⁻³ M in methanol. All other solutions were prepared using deionized water (18.2 M Ω -cm).

A sandy loam soil was used in all soil-related tests in this study. The soil was obtained from the E.V. Smith Research Center of Auburn University at Shorter, AL. Before use, the soil was screened through a standard 2 mm sieve, and then washed with tap water ten times (5 days) to remove the fine colloids and portion of water soluble compositions that were hardly separated from water by normal centrifugation. The washed soil sample was then air-dried, thoroughly mixed, and then stored at room temperature (20±1°C) for use. Soil texture, pH, compositions and cation exchange capacity (CEC) were analyzed by the Auburn University Soil Testing Laboratory. **Table 2-1** provides detailed soil properties and analytical methods.

Table 2-1. Physical and Chemical Properties of the Soil Used in This Work

Sample		Taxonomy ^a		CEC ^b		OM ^c ,	S ^c ,	PZSE ^d	Ca ^e	K	Mg	P	
				meq/100g		%	%		ppm	ppm	ppm	ppm	
Smith Research		Sandy											
Center soil		Loam		3.2		0.4	0.02	5.2	234	51	71	11	
Al ^f	Cu	Fe	Mn	Zn	Na	As	Ba	Cd	Cr	Mo	Ni	Pb	B
ppm	ppm	ppm	ppm	ppm	ppm	ppm	ppm	ppm	ppm	ppm	ppm	ppm	ppm
72	3	25	22	2	4	<0.1	5	<0.1	<0.1	<0.1	<0.1	<0.1	<0.1

^a Soil textural analysis was conducted following the Bouyoucos hydrometer method (Bouyoucos, 1962).

^b CEC: Cation exchange capacity, measured per EPA Method 9081.

^c Organic carbon and sulfur were determined following the combustion method (Kirsten, 1979).

^d The pH at point of zero salt effect (PZSE) of the soil was measured following the potentiometric titration method (Marcano-Martinez and McBride, 1989).

^e Soil potassium, calcium, magnesium and sodium were extracted following Melich I procedure.

^f Soil metal contents were acid digested following EPA method 3230.

2.2.2 Preparation of CMC-stabilized MnO₂ particles

CMC-stabilized MnO₂ particles were synthesized by modifying to the classical Murray's method (Murray, 1974) in the presence of CMC. In brief, a 55.6 mg/L CMC solution and a 4 mM MnCl₂ solution were prepared separately and purged with purified N₂ gas for 20 minutes to remove dissolved oxygen (DO). Then, 3 mL of the MnCl₂ solution was added into 45 mL of the CMC solution under N₂ purging to yield a mixture containing the CMC-Mn²⁺ complex. Then, 2 mL of a stock solution containing 4 mM of KMnO₄ and 8 mM of NaOH was added into the mixture dropwise while the reactor was shaken at 250 rpm. After continued mixing/reaction for 20 min, the resulting 50 mL, 4×10⁻⁴ M MnO₂ nanoparticles were allowed to stay still and grow for 24 h at room temperature (21±1°C) before subsequent tests. For comparison, non-stabilized MnO₂ particles were also prepared following the same procedure but without the stabilizer. Our XRD analysis indicated the synthesized non-stabilized and CMC-stabilized MnO₂ are all largely amorphous, which agrees with the reported observations (Lin et al., 2009; Zhang and Huang, 2003). According to Murray (1974), the MnO₂ particles are amorphous birnessite (δ-MnO₂).

2.2.3 Degradation of E2 in water

Batch experiments were conducted to test the effectiveness of the nanoparticles for oxidation of E2 in the aqueous phase. The tests were carried out in duplicate in 1 L glass flasks sealed with rubber stoppers (the stoppers had no contact with the solution). Each reactor contained 50 mL of CMC-stabilized or non-stabilized MnO₂ suspension (MnO₂ = 4×10⁻⁴ M), which was then diluted by adding 950 mL of a solution buffered by NaAc/HAc (Ac⁻ = 0.0053 M), yielding a final solution containing 2×10⁻⁵ M of MnO₂ and

0.005 M of Ac^- at pH 5. Oxidation of E2 was initiated by injecting 80 μL of an E2 stock solution into the reactors, resulting in an initial E2 concentration of 4×10^{-6} M. The flasks were covered by aluminum foil to avoid photolysis and mixed on a plate shaker at 200 rpm and at room temperature ($20 \pm 1^\circ\text{C}$). At selected times, 4 mL each sample was taken from the reactors using a glass pipette and transferred into a glass tube containing 1 mL of 0.4 g/L ascorbic acid, which was able to completely dissolve the MnO_2 particles, and thus terminate the reaction. The effectiveness of ascorbic acid for dissolution of MnO_2 has been evaluated by Xu et al. (2008) and was confirmed in this work. The samples were then filtered through an Anotop 10 filter (0.22 μm pore size aluminum-oxide membranes (Whatman, GE Healthcare Life Sciences, Piscataway, NJ, USA), and 1 mL each of the filtrate was transferred to 2 mL amber sample vials and analyzed for E2 by HPLC. The E2 retention by the filters was negligible ($< 1.2 \pm 0.7\%$, mean \pm SD). To investigate the pH effect, the same experiments were also conducted at pH 6, 7 and 8 buffered by $\text{NaH}_2\text{PO}_4/\text{NaOH}$ (total PO_4^{3-} was 0.005 M). Control tests indicated that these buffers themselves had negligible effect on E2 oxidation. Additional control tests showed that the presence of 2.5 mg/L of CMC did not degrade any significant E2 without MnO_2 . To investigate the effect of soluble soil organic matter, batch kinetic tests were carried out using a soil-amended background solution, which was prepared by mixing soil with DI water at a soil: solution ratio of 1(g):10 (mL) for 3 days, and then collecting the supernatant upon centrifugation followed by filtration through a 0.22 μm membrane.

2.2.4 Soil sorption and desorption kinetics of E2

Soil sorption and desorption kinetic tests of E2 were conducted in 65 mL amber glass vials sealed with open-top screw caps and PTFE-lined septa. The tests were

designed to gauge the sorption/desorption rates and reversibility, and how physical availability of soil-sorbed E2 affects the subsequent oxidation of E2. Soil samples of 6 g each were placed in the vials and then wet-autoclaved to eliminate bioactivities (confirmed through control tests) in the subsequent tests following the method of Mashtare et al. (2011). Autoclaving had less impact on soil sorption and desorption properties than chemical sterilization methods (Hildebrand et al., 2006). Our tests indicated that sodium azide (NaN_3), a commonly used bio-inhibiting agent, inhibited E2 oxidation by MnO_2 , and thus, was avoided in our tests. The sorption tests were initiated by adding 60 mL of 4×10^{-6} M of an E2 solution to each of autoclaved vials at a soil-to-solution mass ratio of 1:10. The methanol content in the solution was less than 0.1% (v/v), at which no co-solvent effect is expected on the sorption (Rao et al., 1990). The mixtures were mixed on an end-over-end rotator (40 rpm) and placed in an incubator at $21 \pm 1^\circ\text{C}$. At predetermined times, duplicate vials were sacrificially centrifuged at 2000 rpm (805 g-force) for 20 min, and the supernatants were then filtered using 0.1 μm Anotop syringe filters and analyzed for E2 remaining in the aqueous phase by HPLC. Desorption kinetic tests were carried out with the same batch reactors. Following the sorption equilibrium (which took one week), the soil and solution were separated through centrifugation at 805 g-force, and desorption of E2 was initiated by replacing ~ 57 mL (95%) of the supernatant with the same volume of soil-amended water (prepared by mixing the soil and water at the same soil:solution ratio). The vials were then mixed on the rotator at 40 rpm in an incubator. At selected times, duplicate vials were sacrificially sampled and analyzed for E2 in water following the same procedure as in the sorption tests. To assure mass balance, E2 remaining in soil was extracted using 40 mL methanol in a hot water

bath at 70°C for 4 hours. The recovery of E2 from the sorption and desorption tests was 94±4%.

2.2.5 Degradation of soil-sorbed E2

Following the sorption equilibrium, which resulted in an uptake of E2 of 0.0019 mg/g-soil, the soil and solution were separated by centrifugation. Then, the degradation kinetic tests for the soil-sorbed E2 were initiated by replacing ~95% (57 mL) of the supernatant in each vial with the same volume of a MnO₂ particle suspension. The mixtures were then placed on an end-over-end rotator (40 rpm) in an incubator at 21±1°C. At selected sampling times, duplicated vials were centrifuged and the supernatants were sampled and analyzed for E2 in water in the same manner as described above. E2 remaining in the soil phase was extracted by the hot-methanol method. Duplicate control tests were conducted under identical conditions but without MnO₂.

2.2.6 Nanoparticle characterization

TEM images of the nanoparticles were obtained using a Zeiss EM10 transmission electron microscope (Zeiss, Thornwood, NJ, USA) operated at 60 kV. To this end, the nanoparticle samples were prepared by placing 30 µL each of a freshly synthesized nanoparticle suspension on a formvar/carbon coated copper grid and then air-dried overnight. The hydrodynamic particle size and zeta potential of CMC-stabilized MnO₂ nanoparticles were determined by dynamic light scattering (DLS) (Zetasizer Nano ZS, Malvern Instruments Ltd, Malvern, Southborough, MA, USA) at 25°C, where the resultant intensity data were converted to the volume-weighted hydrodynamic diameter.

The physical stability of CMC-stabilized MnO₂ nanoparticles were tested through gravitational sedimentation experiments. The particles were prepared at a fixed MnO₂

concentration of 17.4 mg/L but with various concentrations (1-250 mg/L) of CMC. After preparation, the particles suspensions were allowed to standstill, and samples were taken at predetermined times from the top 2 cm of the suspensions and analyzed for the total Mn using an atomic-absorption spectrophotometer following proper acid dissolution (0.4 g/L ascorbic acid) of the particles.

2.2.7 Analytical methods

E2 was analyzed using an HP Agilent 1100 high-performance liquid chromatography (HPLC) system equipped with a ZORBAX SB-C18 column (4.6×150mm, 3.5 μm) and by modifying the method by (Havlikova et al., 2006). The mobile phase was a mixture of 40:60 (v/v) of acetonitrile and phosphoric acid (0.085%) at a flow rate of 1 mL min⁻¹. A UV detector (G1314A VWD) was operated at a wavelength of 210 nm, giving a detection limit of 1×10^{-7} M. Manganese was analyzed with a flame atomic-absorption spectrophotometer (AAS) (220FS, Varian, Palo Alto, CA). Bromide was analyzed using a Dionex Ion Chromatography (DX-120, Dionex, Sunnyvale, CA), with a detection limit <0.05 mg/L.

2.3 Results and discussion

2.3.1 Effect of CMC/MnO₂ molar ratio on particle size

Based on our prior work, CMC molecules can be adsorbed onto the surface of various kinds of iron-based nanoparticles such as zero-valent iron (He and Zhao, 2007; He et al., 2007), FeS (Xiong et al., 2009), Fe₃O₄ (An et al., 2011), and the sorbed CMC was able to stabilize the nanoparticles through concurrent steric and electrostatic repulsions that prevent the nanoparticles from aggregation. However, the critical stabilization concentration (i.e., the minimum CMC concentration required to fully

stabilize the nanoparticles) varied for different types of nanoparticles. As the uptake of a stabilizer by nanoparticles varies with the stabilizer concentration, it is expected the stabilizer concentration will affect the resultant particle size. To test the effectiveness of CMC for stabilizing MnO₂ particles, MnO₂ nanoparticles were synthesized at CMC:MnO₂ molar ratios from 5.56×10^{-5} to 1.39×10^{-2} with a fixed concentration of MnO₂ of 2×10^{-4} M (17.4 mg/L). **Figure 2-1(a)** shows the volume weighted hydrodynamic size distributions of the nanoparticles at various CMC:MnO₂ molar ratios, and **Figure 2-1(b)** shows the stability of the nanoparticles measured by normalized Mn concentration changes (C/C_0) over time when the MnO₂ suspensions were subjected to gravity sedimentation. At CMC:MnO₂ molar ratios of $\geq 8.33 \times 10^{-4}$, fully stabilized MnO₂ nanoparticles were obtained, and the mean hydrodynamic diameter of the nanoparticles was smaller than 40 nm and the size distribution was relatively narrow (>80% of the particles fall between 20 and 50 nm, **Figure 2-1(a)**). Lower CMC concentrations resulted in larger particles. When the CMC:MnO₂ ratio was lowered to 2.78×10^{-4} , the mean hydrodynamic size increased to 60 ± 2 nm and more (~30%) larger particles (>100 nm) were found, yet the particles remain stable in the suspension during the one week sedimentation tests (**Figure 2-1(b)**). Further lowering the CMC:MnO₂ ratio to 5.56×10^{-5} increased the mean diameter to 131 ± 2 nm, and resulted in rapid sedimentation of the particles after 3 days, and more than 90% of the particles settled in 7 days (**Figure 2-1(b)**). The smallest and the most uniform (monodisperse) nanoparticles were obtained at the CMC:MnO₂ ratio of 1.39×10^{-3} , where 88% of the nanoparticles were between 20-50 nm. Consequently, this molar ratio was held as the norm in the subsequent experiments. Gong et al. (2012) used a CMC:FeS molar ratio of 0.001 to obtain well stabilized FeS

nanoparticles, and He and Zhao (2007) used a CMC:Fe²⁺ of 0.0124 to stabilize ZVI nanoparticles.

Figure 2-2 shows TEM images of non-stabilized versus CMC-stabilized MnO₂ particles. The CMC stabilization resulted in fully stabilized discrete nanoparticles with a mean size of 37±10 nm, which remained suspended in water for more than 10 months. In contrast, the non-stabilized MnO₂ particles appeared as irregular, inter-bridged aggregates, which settled under gravity within 1 hour. The anisotropic shape of the CMC-MnO₂ particles may result from the differing affinities of the stabilizers to the exposed crystal faces during particle growth. Note the DLS-based particle size included both the core MnO₂ and the CMC coating while the TEM-based particle size measured only electron dense metal oxide core.

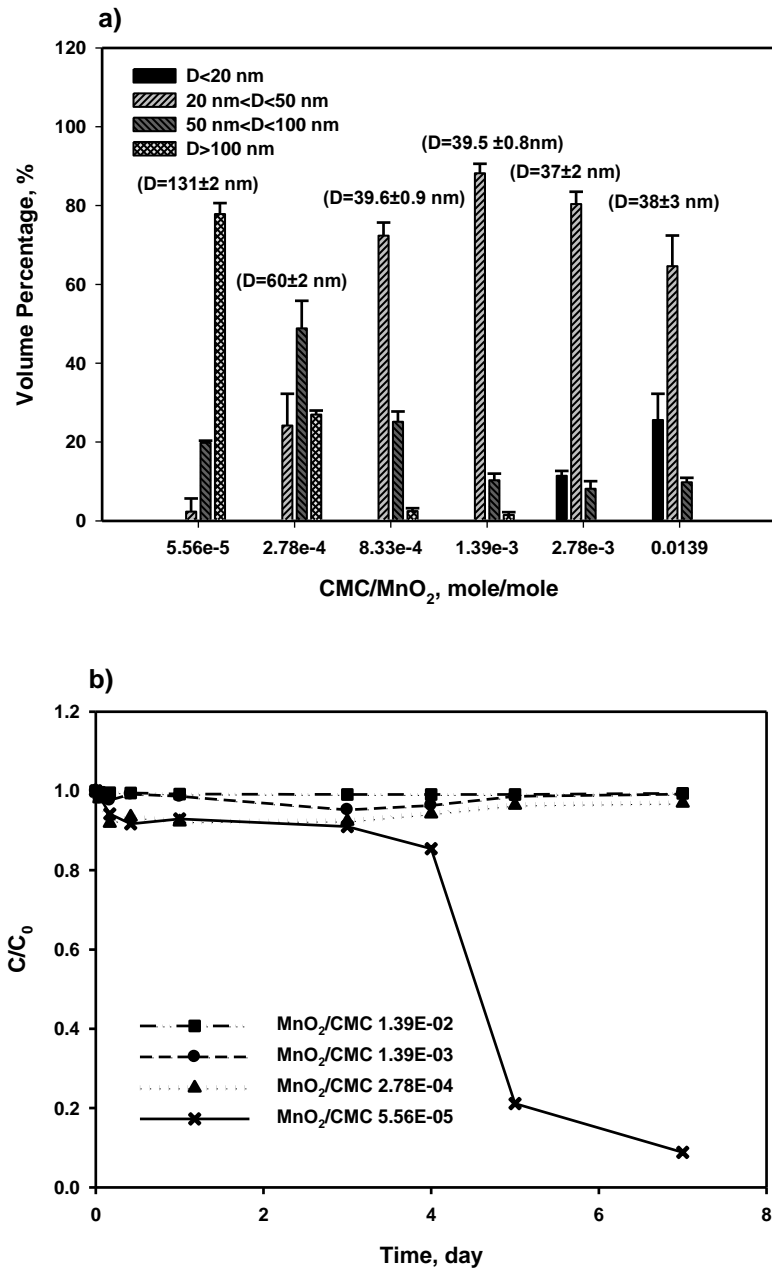


Figure 2-1. a) Hydrodynamic size distribution and mean hydrodynamic diameter of MnO₂ nanoparticles prepared at various CMC:MnO₂ molar ratios; b) MnO₂ stability measured as normalized Mn concentration (C/C_0) as a function of time through sedimentation tests. Note: $[MnO_2] = 2 \times 10^{-4}$ M (17.4 mg/L), $[CMC] = 1.1 \times 10^{-8}$ - 2.8×10^{-6} M (1-250 mg/L); D: mean hydrodynamic diameter, C: Mn concentration in the top 2 cm of the suspension at time t, and C_0 : total Mn concentration; Error bars indicate standard deviation from the mean. Data are plotted as mean of duplicates.

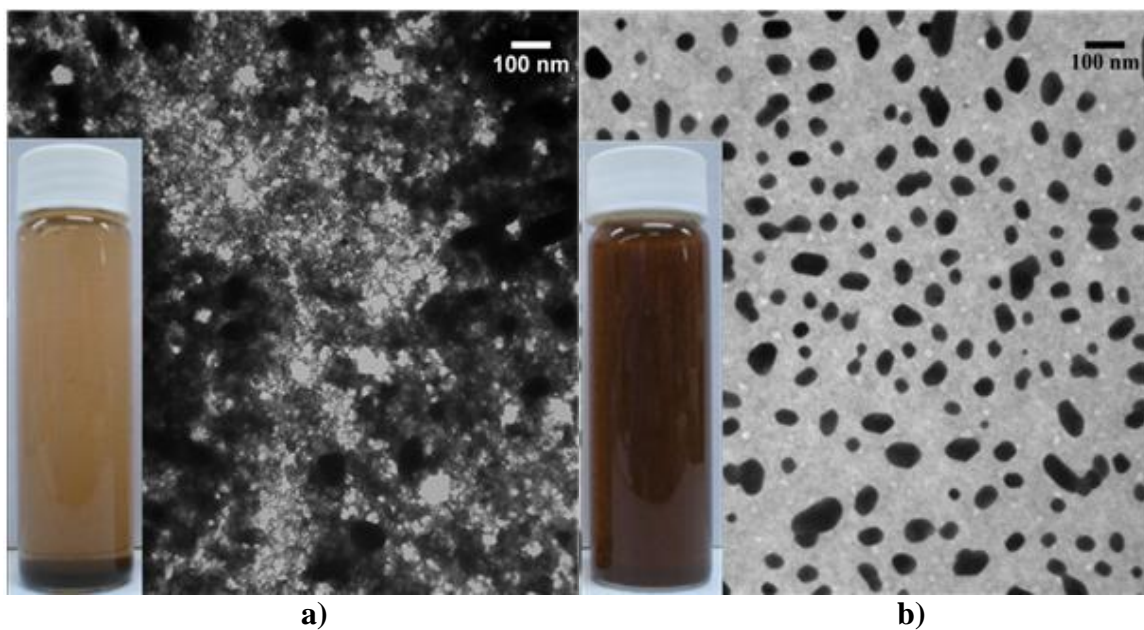


Figure 2-2. Photographs and TEM images of: **a)** non-stabilized MnO₂, and **b)** CMC-stabilized MnO₂ particles. Pictures were taken 30 minutes after synthesis. [MnO₂] = 8×10^{-4} M (0.07 g/L) for both cases, and CMC/MnO₂ molar ratio = 1.39×10^{-3} for case b).

2.3.2 Degradation of aqueous E2 with CMC-stabilized MnO₂ nanoparticles

Figure 2-3 compares E2 degradation kinetics using non-stabilized (bare) MnO₂ particles and CMC-stabilized MnO₂ nanoparticles prepared with various CMC concentrations. Control tests showed that in the absence of MnO₂, the E2 concentration remained constant, indicating no mass loss of E2 in the experimental system and in the analytical processes. Control tests also indicated that the stabilizer did not react with E2, and the reaction of CMC with MnO₂ was negligible during the E2 degradation (release of Mn²⁺ was <0.05 mg/L when MnO₂ reacted with CMC for 48 h). Effective degradation of E2 was observed for both stabilized and non-stabilized MnO₂ particles. In both cases, 4×10⁻⁶ M E2 in the solution was completely degraded by 2×10⁻⁵ M of MnO₂ within 2 days at pH 5, and increasing CMC from 2.5 to 25 mg/L had virtually no effect on the reaction kinetics.

The kinetic profiles showed a fast initial degradation rate with a slower and gradual long-term rate. Similar kinetic profiles were also observed by other researchers (Lin et al., 2009; Xu et al., 2008; Zhang and Huang, 2003), who studied oxidation of tetrabromobisphenol A, steroid estrogens, triclosan, and chlorophene using synthetic δ-MnO₂ powders. Despite the apparently larger sizes, non-stabilized MnO₂ particles displayed a faster initial degradation rate, with ~50% of E2 degraded in the first 20 minutes. In contrast, CMC-stabilized MnO₂ nanoparticles exhibited a much slower initial rate, with ~10% of E2 degraded in 20 minutes, but displayed a faster longer-term rate and caught up with non-stabilized MnO₂ particles at ~24 h.

To further compare the degradation lifetime of bare and CMC-stabilized MnO₂ particles, consecutive degradation batch tests were conducted. **Figure 2-4** shows kinetic

profiles of E2 degradation in consecutive spikes of E2 with non-stabilized and CMC-stabilized MnO₂. When the same MnO₂ particles were exposed to repeated spikes of E2 (E2 = 4×10⁻⁶ M in each spike), CMC-stabilized MnO₂ remained effective in three consecutive runs and degraded cumulatively 1.21×10⁻⁵ (±0.3%) M of E2, whereas bare MnO₂ exhausted at the end of the second run and degraded a total of 7.50×10⁻⁶ (±0.01%) M of E2. This observation confirms that the CMC stabilization resulted in greater surface area, more reactive surface sites, and longer reactive lifetime of the nanoparticles.

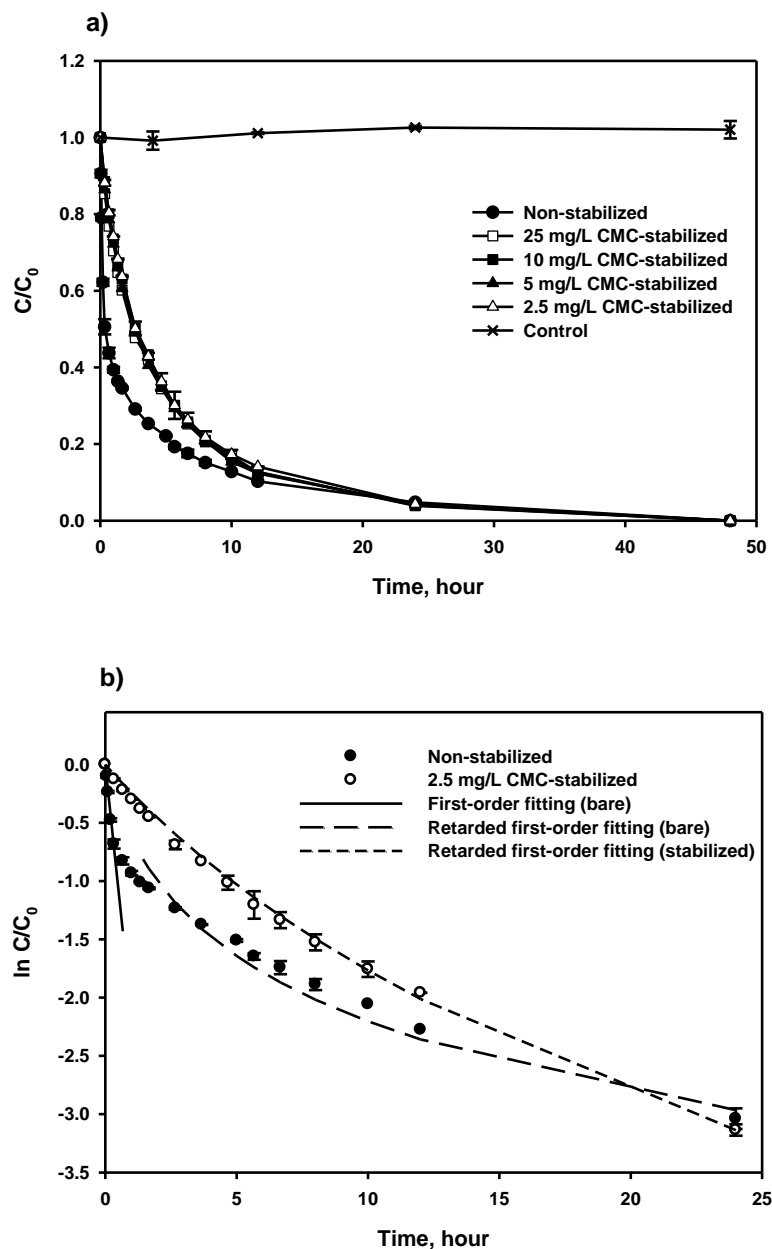


Figure 2-3. a) Oxidative degradation of E2 in water by MnO_2 particles prepared in the presence of various concentrations of CMC and at a fixed MnO_2 dosage of 2×10^{-5} M. b) Linearized first order plot for non-stabilized and CMC-stabilized degradation rate data. Initial $[\text{E2}] = 4 \times 10^{-6}$ M, $[\text{CMC}] = 2.5$ mg/L (CMC/ MnO_2 molar ratio = 1.39×10^{-3}), 5 mg/L (CMC/ $\text{MnO}_2 = 2.78 \times 10^{-3}$), 10 mg/L (CMC/ $\text{MnO}_2 = 5.56 \times 10^{-3}$) and 25 mg/L (CMC/ $\text{MnO}_2 = 0.0139$). All tests were buffered at pH 5 by HAc/NaAc. Data plotted as mean of duplicates and errors calculated as standard deviation.

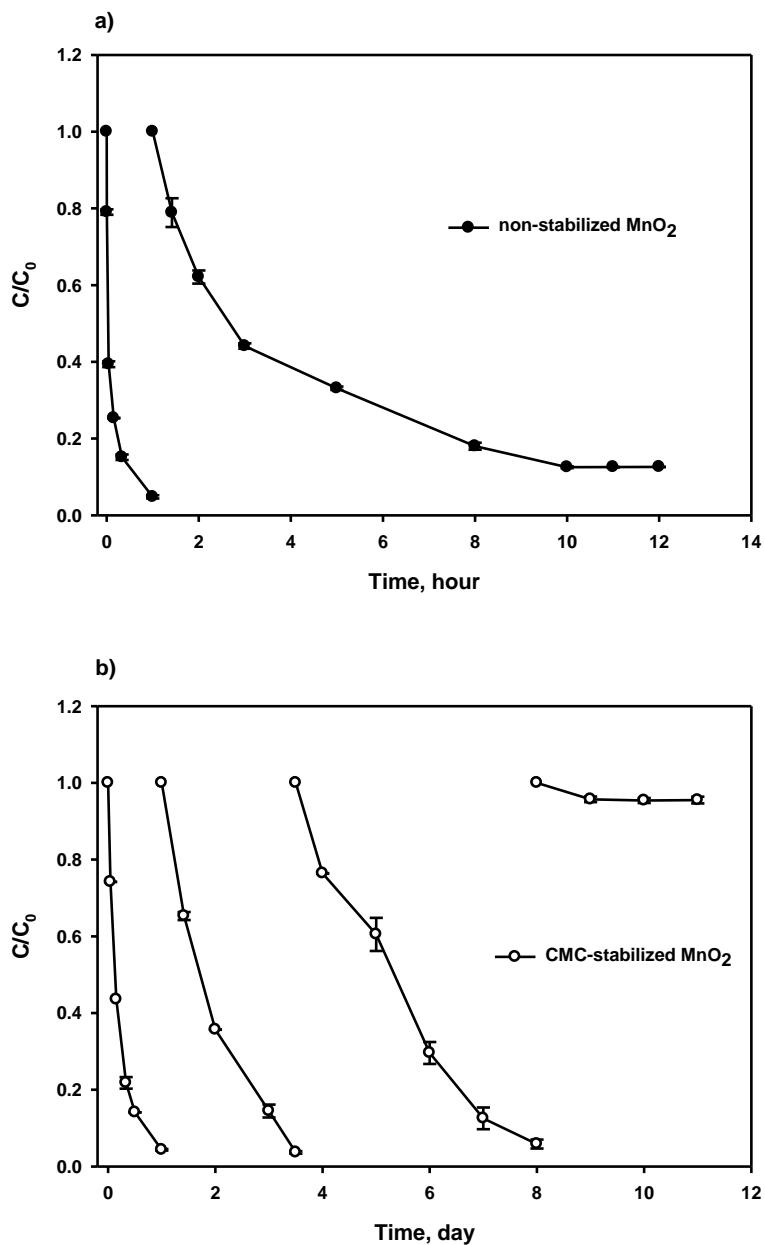


Figure 2-4. Batch kinetic profiles of E2 degradation in consecutive spikes of E2 using the same MnO₂: **a)** non-stabilized MnO₂; **b)** CMC-stabilized MnO₂. In both cases, [MnO₂] = 2×10⁻⁵ M, [CMC] = 2.5 mg/L, [E2] in each spike = 4×10⁻⁶ M, pH = 5 (buffered by HAc/NaAc). At the end of each run there is still trace of amount of E2 residual. C₀: Initial E2 concentration in each run. For Case a), the initial E2 concentration for the first run and second run was 4×10⁻⁶, and 4.19×10⁻⁶ M, respectively; For case b), the initial E2 concentration for the four runs was 4×10⁻⁶, 4.18×10⁻⁶, 4.20×10⁻⁶, and 4.35×10⁻⁶ M, respectively.

Based on work on synthetic or mineral MnO₂, researchers (Jiang et al., 2010; Lin et al., 2009; Rubert and Pedersen, 2006; Zhang and Huang, 2003) described the oxidation of organic contaminants on surface of MnO₂ as a two-step process: 1) adsorption of E2 onto the MnO₂ surface, forming a precursor surface complex, and 2) electron transfer from E2 to MnO₂ and release of the organic products and Mn²⁺.

For both stabilized and non-stabilized MnO₂, the reaction rate decreases over time, indicating a gradual loss of the reactive sites or the reactivity. Several factors can cause the reactivity loss, including accumulation of degradation products and Mn²⁺ onto the MnO₂ particles (i.e., an auto-inhibiting effect) and poisoning of the MnO₂ surface by the reaction products (Rubert and Pedersen, 2006). The oxidation potential of MnO₂ decreases as more reduction products (e.g., Mn²⁺) are formed (Eqs. 1-2) (Lin et al., 2009; Zhang and Huang, 2003). For non-stabilized MnO₂, the bare particle surface offers easier accessibility of the reactive sites (i.e., less mass transfer resistance), resulting in the observed faster initial rate. For stabilized nanoparticles, the CMC coating on the nanoparticles plays some opposing roles. First, the CMC stabilization resulted in smaller particles sizes of the core MnO₂, which gives higher specific surface area and thus favors E2 removal. Second, the CMC coating adds a mass transfer barrier, which inhibits the accessibility of the reactive sites and limits the formation of the precursor complex for E2 degradation. The added mass transfer resistance is revealed by comparing the initial degradation rates for bare and CMC-stabilized particles (**Figure 2-3**) and by the fact in **Figure 2-4** that CMC-stabilized MnO₂ degraded more E2 but with a slower initial rate than the bare particles. Previous studies also showed coating a polymer or dissolved organic matter on nanoparticles could inhibit the mass transfer rate (Sakulchaicharoen et

al., 2010; Zhang et al., 2011). Lastly, the CMC layer may also prevents adsorption of the reaction products (e.g., Mn^{2+}) on the nanoparticles, thereby mitigating the auto-inhibitive effects of the by-products. Fig. S3 in SI shows that the inhibitive effect of Mn^{2+} was much alleviated for CMC-MnO₂ than the bare particles. It is noteworthy from **Figure 2-3** that the presence of various concentrations of CMC (from 2.5 to 25 ppm) resulted in nearly identical degradation rates. This observation suggests that the opposing effects of CMC are counteracting. On the one hand, higher CMC concentration gives smaller nanoparticles; on the other hand, the mass transfer resistance increases with increased CMC uptake. For example, the CMC surface excess on MnO₂ was measured to be 0.042 ± 0.003 , 0.044 ± 0.007 , and 0.057 ± 0.007 g/m² for 2.5, 5 and 25 mg/L CMC, respectively (**Table 2-2**). For auto-inhibitive reaction kinetics, researchers have proposed a two-stage modeling approach to interpret the oxidation kinetics of organic compounds by conventional bare MnO₂, namely, using a pseudo-first-order kinetic equation (Eqn. 2-3) for the initial reaction rate, and a retarded first-order model (Eqn. 2-4) for the longer-term kinetics (Lin et al., 2009; Rubert and Pedersen, 2006):

$$-\frac{dC_t}{dt} = k_1 C_t \text{ or } C_t = C_0 \cdot e^{-k_1 \cdot t} \quad (2-3)$$

$$-\frac{dC_t}{dt} = \frac{k_a}{1+\alpha t} C_t \text{ or } C_t = C_0 (1 + \alpha t)^{-k_a/\alpha} \quad (2-4)$$

where C_0 and C_t are E2 concentrations (μ M) at time 0 and t, respectively, k_1 is the pseudo-first-order rate constant (h^{-1}) in the initial stage (first 20 minutes), k_a is the apparent rate constant (h^{-1}), which is analogous to the initial pseudo first order rate constant adapted to the retarded rate equation, and α is the retardation factor indicating the extent of departure from the pseudo-first-order behavior (Weber, 2001). The retarded first-order model accommodates a gradual deviation from the first-order reaction in an

empirical way by incorporating a “sliding” factor in the reaction rate constant (Lin et al., 2009).

Figure 2-3(b) shows that the pseudo-first-order kinetic equation adequately interpreted the rapid initial (first 20 minutes) degradation kinetics ($R^2 = 0.988$), but failed to fit the long-term kinetics ($R^2 = 0.371$) for non-stabilized MnO_2 , while the first-order retarded model was able to interpret the longer-term rate ($R^2 = 0.955$). Interestingly, for CMC-stabilized MnO_2 , the retarded model was able to well simulate the entire oxidation kinetics ($R^2 = 0.997$), suggesting that the CMC coating may have mitigated the auto-inhibitive effects, and diffusion through the surface layer is an important step throughout the reaction course. The same good fitting was also observed for CMC-stabilized MnO_2 at pH 5, 6, 7, and 8 (**Figure 2-5** and **Figure 2-6**), where the retarded first-order model was able to nicely simulate the entire kinetic data with a coefficient of determination (R^2) > 0.97 (**Table 2-3**). For bare MnO_2 , the two-stage model was necessary to simulate the kinetics at pH 5, where a much rapider initial degradation rate was evident. However, at elevated pH (6-8), the retarded equation alone was able to adequately simulate the degradation data for bare MnO_2 as well ($R^2 > 0.98$). **Table 2-3** gives the best-fitted retarded first-order model parameters. In all cases, the k_a values decreased with increasing pH, and CMC-stabilized nanoparticles showed a lower k_a and also a lower α value than non-stabilized MnO_2 , which is consistent with the observed rate data.

Table 2-2. CMC Surface Density on MnO₂

Con. of CMC, mg/L	C_{ads}^a , mg/L	r^b , nm	δ^c , g/m ²
2.5	1.3±0.1	19.8±0.4	0.042±0.003
5	1.4±0.2	18.3±0.8	0.044±0.007
25	1.8±0.2	19±1	0.057±0.007

^aCMC concentration adsorbed on the particle surface, is determined by measuring the differences between the initial and final CMC concentrations in the aqueous phase using a TOC analyzer. ^bMean particle radius, is obtained from the DLS measurement. ^c δ is CMC surface density on MnO₂ calculated by $\delta = C_{ads} \cdot a_s$, where average specific area of MnO₂ nanoparticles $a_s = 3(\rho r)^{-1}$.

Table 2-3. Retarded Rate Model Parameters.

MnO ₂ particles	pH	k_a (hour ⁻¹)	α (hour ⁻¹)	Model fit (R ²)
Non-stabilized	5	0.70±0.08	0.77±0.08	0.891
CMC-stabilized	5	0.25±0.02	0.096±0.007	0.997
Non-stabilized	6	0.49±0.09	1.2±0.2	0.986
CMC-stabilized	6	0.28±0.03	0.24±0.02	0.973
Non-stabilized	7	0.067±0.008	0.065±0.007	0.995
CMC-stabilized	7	0.071±0.005	0.034±0.002	0.999
Non-stabilized	8	0.019±0.003	0.046±0.007	0.994
CMC-stabilized	8	0.015±0.007	0.03±0.01	0.981

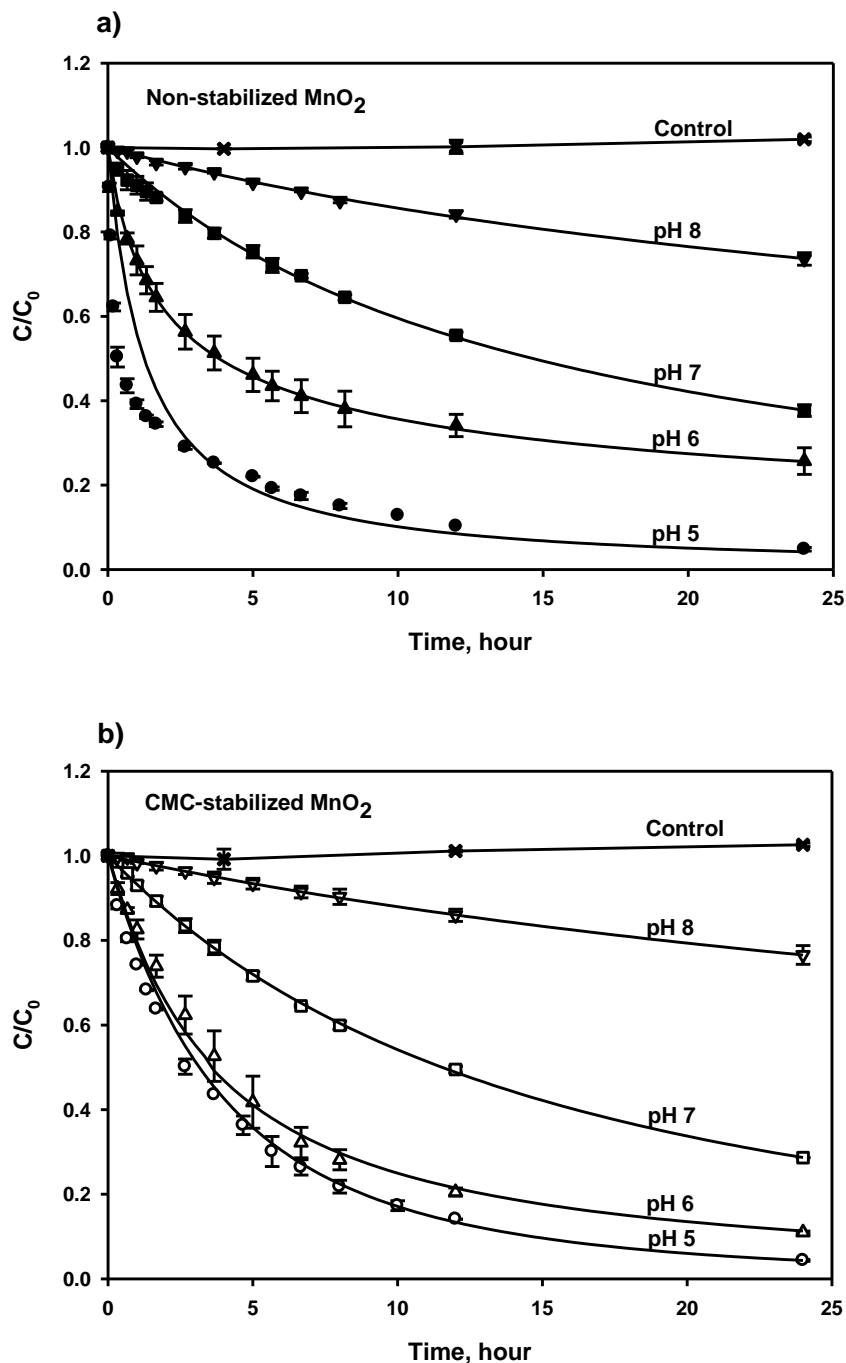


Figure 2-5. Effect of pH on oxidative removal of E2 in water by: **a)** Non-stabilized MnO₂, and **b)** CMC-stabilized MnO₂. Initial [E2] = 4×10⁻⁶ M, [MnO₂] = 2×10⁻⁵ M, [CMC] = 2.5 mg/L, pH 5 buffered by HAc/NaAc, pH 6-8 buffered by NaH₂PO₄/NaOH. Symbols: experimental data; lines: retarded first-order model fittings.

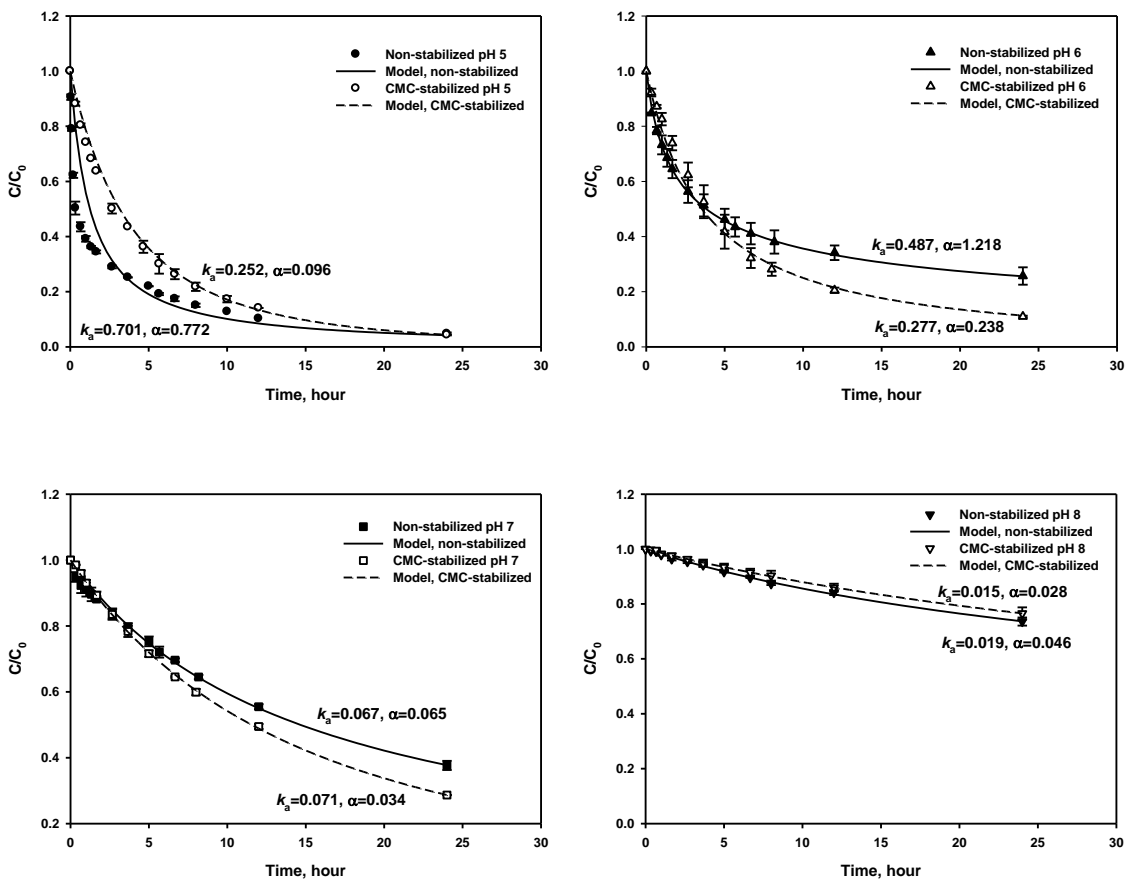
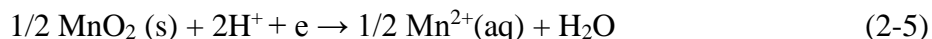


Figure 2-6. Comparing E2 removal rates of non-stabilized and CMC-stabilized MnO_2 particles at pH 5, 6, 7, and 8. Symbols: experimental data; lines: retarded first-order model fittings.

2.3.3 Effect of pH on E2 removal in water

Researchers have reported that the MnO₂-mediated oxidation of various organic compounds (triclosan, chlorophene, oxytetracycline, tetrabromobisphenol A, and E2) is pH dependent (Lin et al., 2009; Rubert and Pedersen, 2006; Xu et al., 2008; Zhang and Huang, 2003). **Figure 2-5** shows oxidation rates of E2 by stabilized and non-stabilized MnO₂ particles at pH 5-8. Overall, the lower pH favors the reaction. Increasing pH from 5 to 8 decreased the k_a value from 0.70 ± 0.08 to 0.019 ± 0.003 hour⁻¹, and 0.25 ± 0.02 to 0.015 ± 0.007 hour⁻¹ for non-stabilized and stabilized MnO₂, respectively (**Table 2-3**). With a pK_a of 10.71, E2 is present in the undissociated neutral form within the pH range. The observed pH-dependent removal rate can be attributed to several factors. First, protons catalyze reduction of MnO₂ (Zhang and Huang, 2003), i.e.,



According to (Stumm and Morgan, 1996), lowering pH from 8 to 4 increases the reduction potential of MnO₂ from 0.76 to 0.99 V. Second, given that the pH at PZC for MnO₂ is 2.25 (Murray, 1974), the surface of MnO₂ is largely negatively charged under the experiment conditions. Zeta potential analysis showed that when pH decreased from 8 to 5, the MnO₂ particle surface potential varied from -33 mV to -28 mV for CMC-stabilized MnO₂ and from -29 mV to -24 mV for bare MnO₂ (analyzed upon sonication). The higher surface charge at higher pH renders the surface less favorable toward the hydrophobic E2 ($\log K_{OC}$ is 2.96), forming less precursor complexes. In addition, the oxide surface is less likely to adsorb cations (e.g., Mn²⁺) at lower pH, which liberates more reactive surface sites for E2.

It is noteworthy that the pH effects are notably different for bare and CMC-stabilized MnO₂ particles, especially in the pH range of 5-7. **Figure 2-6** compares E2 removal rates for bare and CMC-stabilized MnO₂ in the pH range from 5 to 8. In all cases, bare MnO₂ displayed faster initial reaction rates. However, CMC-stabilized MnO₂ nanoparticles caught up and even surpassed the bare MnO₂ at longer times, and the catch-up time was shortened with increasing pH. For instance, at pH 6, CMC-MnO₂ started exceeding bare MnO₂ at 4 h, while at pH 7 the turning point was shortened to ~2 h. In the end, CMC-stabilized MnO₂ degraded 15% and 9% more E2 at pH 6 and 7, respectively. At pH 8, both reactions became very slow and the difference was insignificant. The mean hydrodynamic size of CMC-stabilized MnO₂ particles were 42.8±0.2, 44±1, 45±2, and 45±1 nm for pH 5, 6, 7, and 8 before the degradation tests, respectively. Therefore, pH had little effect on the particle size. The much (9%-15%) better performance of CMC-stabilized MnO₂ suggests that the CMC coating renders the surface reactive sites less vulnerable to the aforementioned unfavorable effects of elevated pH.

2.3.4 Effect of CMC on E2 desorption from soil

As mentioned earlier, the primary purpose to stabilize the nanoparticles is to facilitate particle delivery into the subsurface (i.e., to promote particle mobility) toward in-situ remediation of soil-sorbed E2. As sorption/desorption often limits chemical and biological availabilities, soil sorption and desorption of E2 in the presence of CMC were tested. **Figure 2-7(a)** shows the sorption kinetic data of E2 by the sandy loam soil. The equilibrium was reached in 1 week, and the equilibrium uptake was 0.0019 mg-E2/g-soil. The sorption partition coefficient of E2 ($\log K_{OC}$) was determined to be 2.96±0.03 based on the soil organic carbon (organic matter = 1.724 organic carbon). The relatively low E2

uptake is consistent with the low SOM (soil organic matter) content (0.4%) of the soil (**Table 2-1**).

Following the sorption equilibrium, desorption kinetic tests were carried out with the same E2-loaded soil. **Figure 2-7(b)** shows E2 desorption kinetics without CMC and in the presence of 25 mg/L CMC. The data showed a rapid initial (<3 hours) desorption rate followed by a much slower rate. Approximately 33% of E2 was desorbed in the initial 3 hours, and another 15% was desorbed in the following 7 days. Similar two-phase desorption profiles have been widely reported. Rapid desorption happens in the labile domain where the adsorption sites are easily accessible, while slow desorption is associated with slow diffusion from soil micropores.

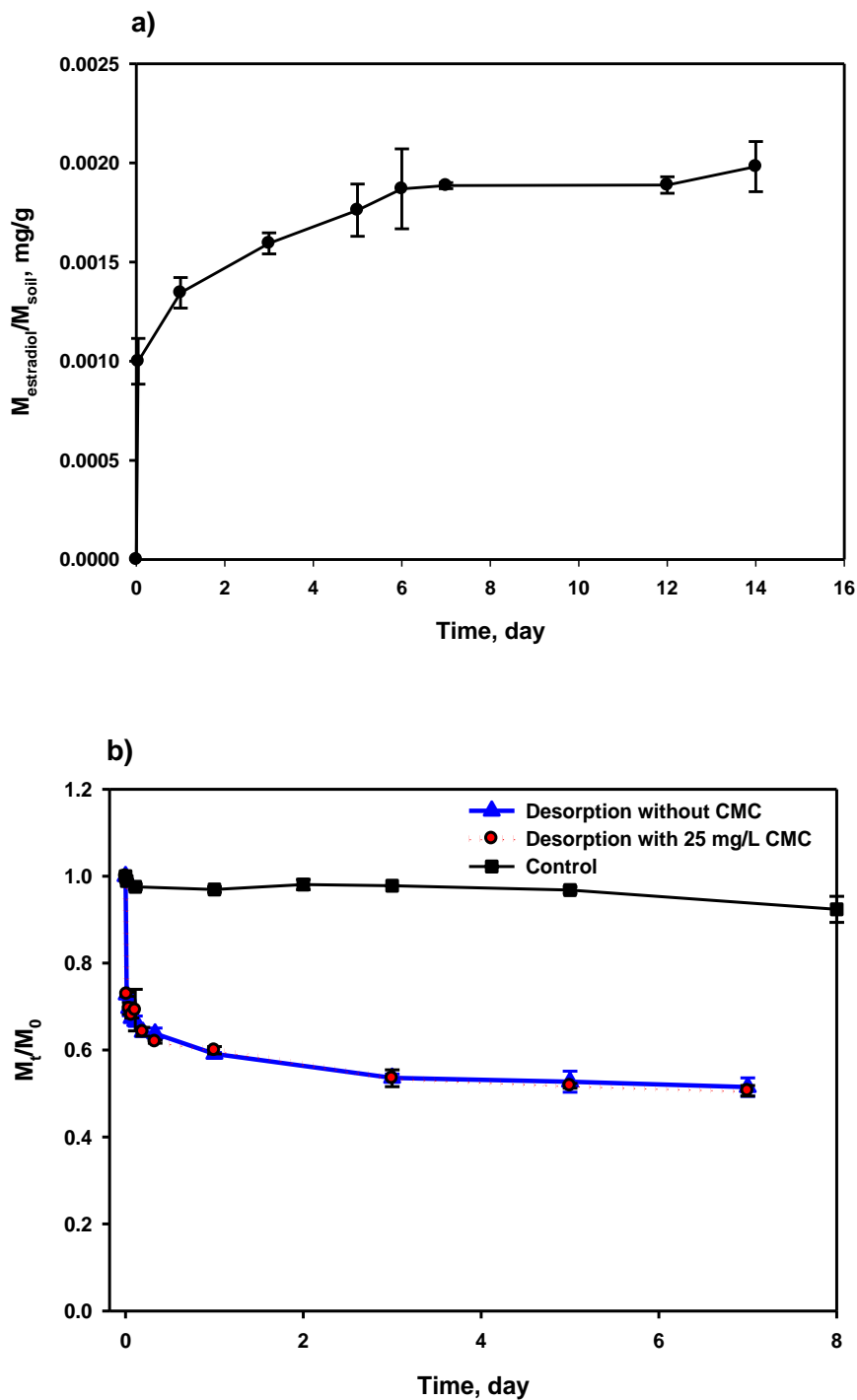


Figure 2-7. a) E2 sorption kinetics with a sandy loam soil (initial aqueous $[E2] = 4 \times 10^{-6}$ M). **b)** Effect of CMC on desorption of E2 from the soil. In figure b) M_t : E2 remaining in soil at time t; M_0 : initial E2 in soil (0.0019 mg/g); pH was 5.65-5.98. Control tests were carried out without soil under otherwise identical conditions.

2.3.5 Degradation of soil-sorbed E2

Figure 2-8 compares the degradation kinetics of E2 in water and E2 that was pre-loaded on the sandy loam at various dosages of CMC-stabilized MnO₂ nanoparticles. More than 97% of aqueous E2 (1.09 mg/L) was degraded in 48 hours by 2×10^{-5} M (1.74 mg/L) CMC-stabilized MnO₂. In contrast, <5% of soil-sorbed E2 (0.0019 mg/g) was degraded with the same dosage of CMC-MnO₂. When the nanoparticle dosage was increased to 8×10^{-5} M and 2×10^{-4} M, 20% and 80% of soil-sorbed E2 were degraded, respectively.

Evidently, the presence of the soil inhibited the oxidation of E2 by the nanoparticles. Several factors can contribute to this effect. First, soil desorption of E2 can limit the degradation kinetics, especially in the later stage of the oxidation process. Second, the nanoparticles can be adsorbed or become associated with the soil, which not only reduces particle mobility and accessibility, but also loses part of the reactive sites. In addition, the dissolved organic matter (DOM) (e.g., humic acid) and metal ions (e.g., Ca²⁺, Mn²⁺) released from soil may also competitively react with MnO₂ (Xu et al., 2008). As a result, larger dosages of MnO₂ particles may be required to treat E2 in contaminated soil.

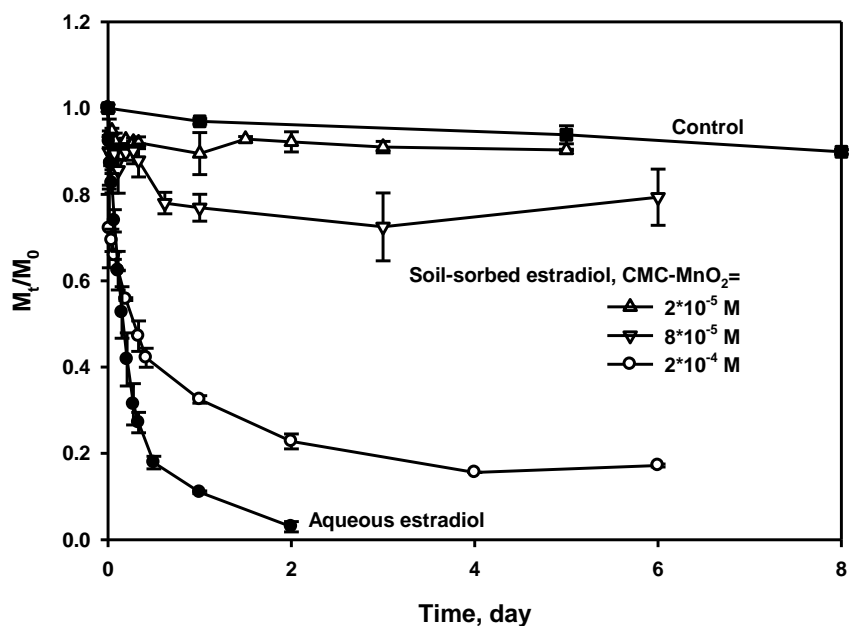


Figure 2-8. Degradation of aqueous and soil-sorbed E2 at various dosages (2×10^{-5} to 2×10^{-4} M) of MnO_2 . Initial [E2] in soil = 0.0019 mg/g, CMC/ MnO_2 molar ratio = 1.389×10^{-3} in all cases, pH = 6.0 ± 0.2 (buffered by $\text{NaH}_2\text{PO}_4/\text{NaOH}$). M_0 = Initial E2 in the reactor system (77.6% in soil); M_t = E2 remaining in the system at time t. Soil mass = 6 g, Solution/suspension volume = 60 mL.

Figure 2-9 compares the effectiveness of non-stabilized MnO₂ and CMC-stabilized MnO₂ nanoparticles in degradation of soil-sorbed E2. To gauge the effects of desorption and the inhibition of soil components, **Figure 2-9** is plotted in terms of E2 remaining in the whole reactor system (both aqueous and soil phases) (**Figure 2-9(a)**) and that in the aqueous phase only (**Figure 2-9(b)**). After 96 hours of reaction, 83% and 70% of E2 were degraded in the heterogeneous system by 2×10⁻⁴ M of CMC-stabilized and non-stabilized MnO₂ particles, respectively (**Figure 2-9(a)**). Unlike in the homogeneous solution systems (**Figure 2-3**), CMC-stabilized MnO₂ clearly outperformed bare MnO₂ particles for degrading soil-sorbed E2 in both degradation rate and extent, and the soil system inhibits the bare MnO₂ more than CMC-MnO₂.

A comparison of the desorption rate (**Figure 2-7(b)**) and degradation data (**Figure 2-9(b)**) reveals that the presence of CMC-stabilized MnO₂ lowered the equilibrium E2 concentration in the aqueous phase from 47% to 8%, and bare MnO₂ from 47% to 17%. At any given time during the experiment, E2 in the aqueous phase accounted for more than 50% of total E2 remaining in the system, indicating that desorption was not the rate-limiting step.

As stated before, soil sorption of the nanoparticles may render some of the reactive sites inaccessible. At day 6, only 7% of CMC-stabilized nanoparticles remained suspended (i.e., 93% attached to soil). **Figure 2-10** shows the zeta potential of soil exudates and the two types of particle suspensions at pH 6 (note the soil pH_{PZC} was 5.2). The less negative zeta potential of bare MnO₂ forecasts a more favorable sorption potential to the soil, i.e., more reactivity loss.

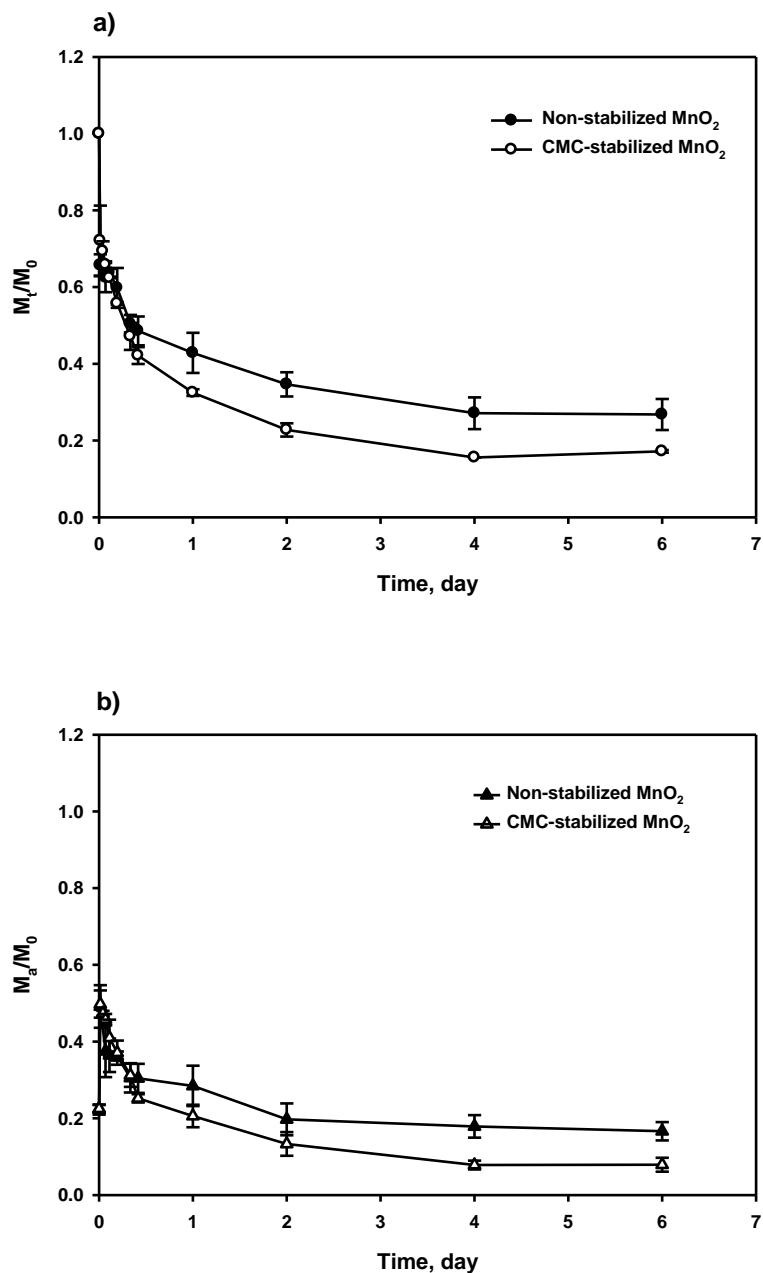


Figure 2-9. Degradation of soil-sorbed E2 with bare and CMC-stabilized MnO_2 particles: **a)** in the whole system, and **b)** in the aqueous phase. Initial [E2] in soil = 0.0019 mg/g, MnO_2 concentration = 2×10^{-4} M, CMC/ MnO_2 molar ratio = 1.389×10^{-3} for stabilized particles, Soil mass = 6 g, Suspension volume = 60 mL, pH = 6.0 ± 0.2 (buffered by $NaH_2PO_4/NaOH$). M_0 : Initial E2 in the reactor system (77.6% in soil), M_t and M_a : E2 remaining in the whole system and the aqueous phase, respectively.

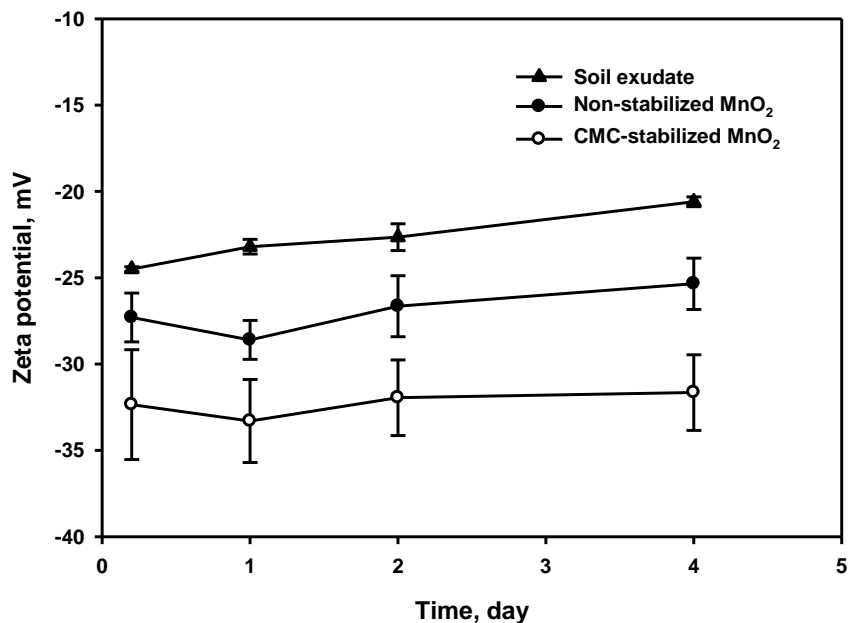


Figure 2-10. Zeta potential of three different suspensions containing: soil exudates, non-stabilized MnO₂ and CMC-stabilized MnO₂, respectively. MnO₂ concentration was 2×10^{-4} M, CMC/MnO₂ molar ratio was 1.389×10^{-3} for stabilized particles, pH was buffered to 6 by NaH₂PO₄/NaOH. Non-stabilized MnO₂ was sonicated for 30 min at 40 kHz using a sonicator (Fisher Scientific, Model FS28, 225W). The time scale indicates aging time under standstill and ambient conditions.

2.3.6 Effect of leachable soil components on E2 degradation

Figure 2-11 shows the aqueous phase E2 degradation kinetics with or without soil extracts by bare and CMC-stabilized MnO₂. The soil extracts contained 6±2 mg/L DOM measured as TOC, 2.5±0.5 mg/L Ca²⁺ and 1.9±0.3 mg/L Mn²⁺. The presence of the soil extracts inhibited the reaction rate in the initial stage (12-16 h), but facilitated the longer term reaction rate. At the end of 24 h experiments, E2 removal was increased from 74% (no soil extracts) to 90% (with soil extracts) by bare MnO₂ and from 89% to 96% by CMC-stabilized MnO₂. Xu et al. (2008) investigated E2 removal rate affected by coexisting metal ions including Fe³⁺, Cu²⁺, Zn²⁺ and Mn²⁺ as well as humic acid, and found that the metal ions inhibited E2 removal but humic acid at low concentrations (1 mg/L) enhanced E2 removal rate. The metal ions were considered competing for the active surface sites with E2 by adsorption to the MnO₂ surface, whereas humic acid can bind with Mn²⁺ and thus, alleviate its inhibitive effects as Mn²⁺ is continuously produced during the redox reaction. **Figure 2-12** shows that the presence of 0.01 M Mn²⁺ or Ca²⁺ remarkably inhibited the degradation rates for both bare and CMC-stabilized MnO₂. The inhibitive effects are attributed to: 1) cation-induced coagulation that destabilized the particles (which was observed in a few minutes), and thus decrease the reactive sites; 2) blockage of the reactive sites due to uptake of the cations; and 3) product (Mn²⁺) auto-inhibition/poisoning of the MnO₂ reduction. Nonetheless, it was clearly evident from **Figure 2-12(a)** that CMC shielded the nanoparticles from the auto-inhibitive effects of Mn²⁺: while Mn²⁺ almost ceased the reaction for bare MnO₂, nearly 50% E2 degradation was achieved by CMC-stabilized MnO₂. In contrast, Ca²⁺ exerted nearly the same effects for both forms of MnO₂ (**Figure 2-12(b)**), suggesting that Ca²⁺ exerted similar inhibitive

effects (site blockage and enhanced aggregation of the particles) on the two forms of MnO₂. **Figure 2-13** shows that the addition of 5 mg/L humic acid (as TOC) increased the reaction rates, resulting in comparable E2 degradation for the two forms of MnO₂. In the presence of soil extracts (**Figure 2-11**), the early inhibitive effect was due to the rapid initial uptake of the soil extracts (DOM, Ca²⁺, Mn²⁺ and their complexes), which diminishes the reactive sites and increases the mass transfer resistance at the particle surface. However, as more Mn²⁺ is produced, the exuded DOM acts as a scavenger of Mn²⁺, thereby alleviating further inhibitive effects. It is noteworthy that the soil extracts exhibited less impact on CMC-stabilized MnO₂ than bare MnO₂, which can be attributed to the protective effect of the sorbed CMC that reduces the accessibility of soil released components to MnO₂ particles and to the ability of CMC molecules to complex with the metal ions.

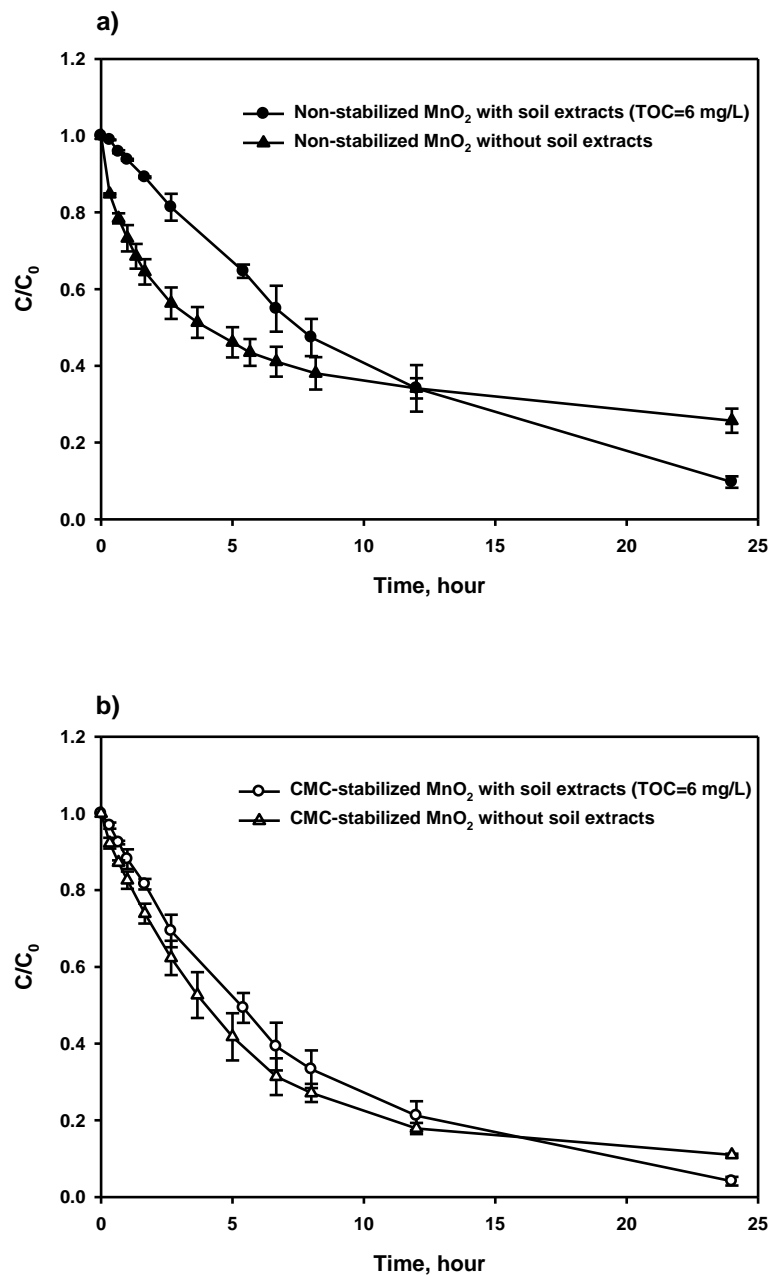


Figure 2-11. Oxidation kinetics of E2 in water with or without soil extracts: **a)** non-stabilized MnO₂, and **b)** CMC-stabilized MnO₂. Initial [E2] = 4×10^{-6} M, [MnO₂] = 2×10^{-5} M, [CMC] = 2.5 mg/L, pH = 6 (buffered by NaH₂PO₄/NaOH). Data plotted as mean of duplicates and errors calculated as standard deviation.

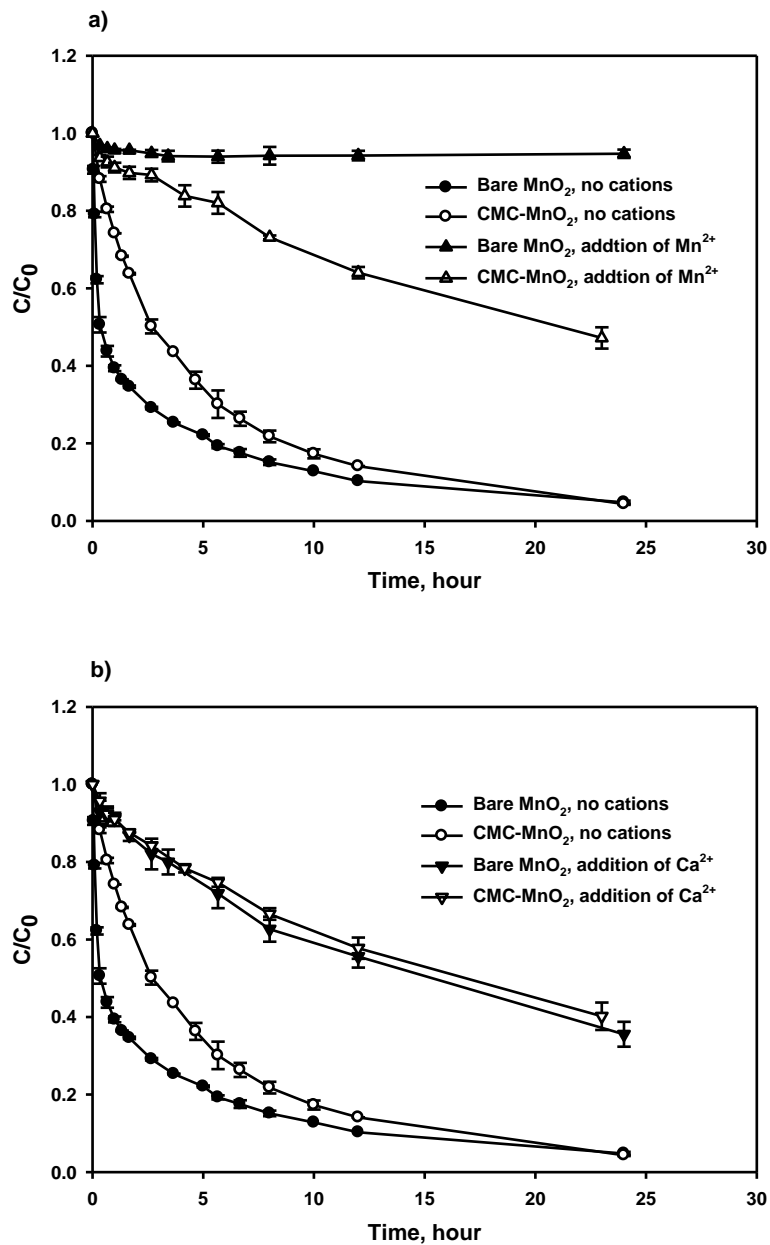


Figure 2-12. Degradation of E2 in water by CMC-stabilized and non-stabilized MnO₂ in the presence of added cations: **a)** [Mn²⁺] = 0.01 M, and **b)** [Ca²⁺] = 0.01 M. [E2] = 4×10⁻⁶ M, [MnO₂] = 2×10⁻⁵ M, [CMC] = 2.5 mg/L, pH = 5 (buffered by HAc/NaAc).

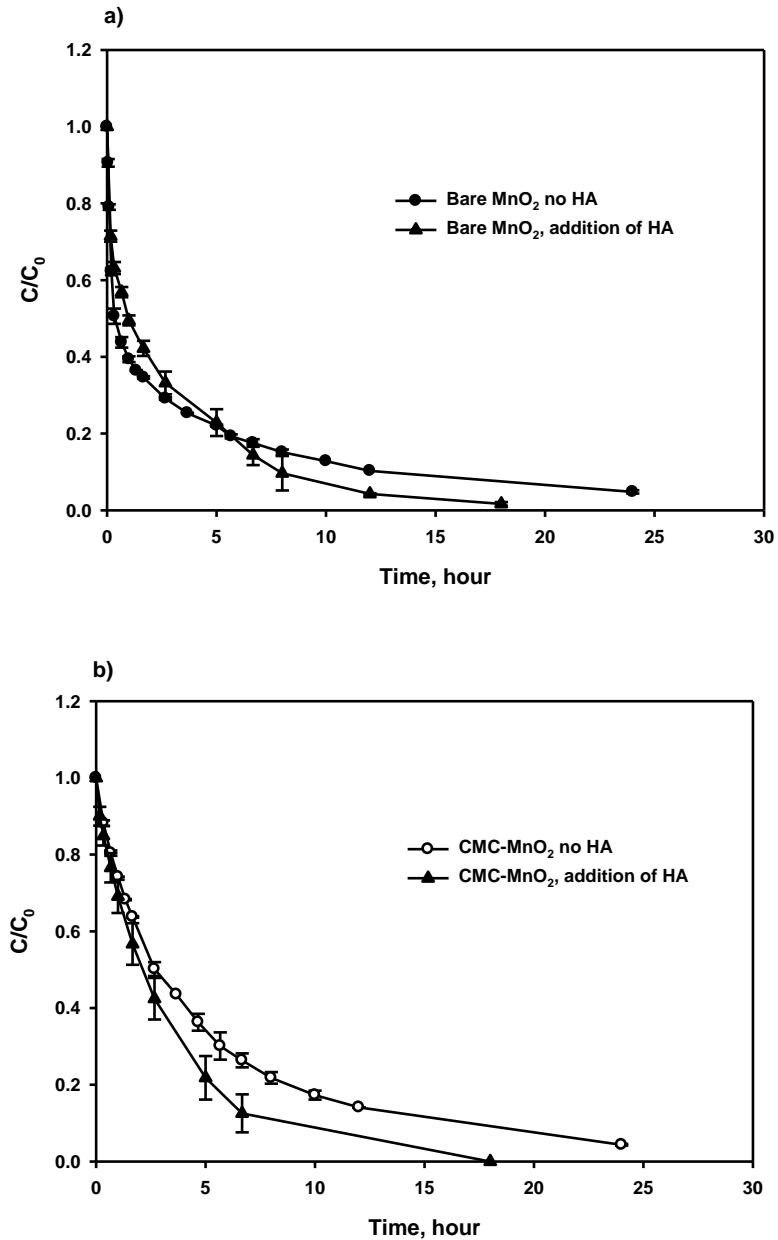


Figure 2-13. Degradation of E2 in water by CMC-stabilized and non-stabilized MnO₂ in the presence of added humic acid (HA): **a)** non-stabilized MnO₂, and **b)** CMC-stabilized MnO₂. [E2] = 4×10^{-6} M, [MnO₂] = 2×10^{-5} M, [CMC] = 2.5 mg/L, pH = 5 (buffered by HAc/NaAc), [HA] = 5 mg/L as TOC.

2.4 Conclusions

This work prepared and tested a new class of CMC-stabilized MnO₂ nanoparticles for oxidative degradation of water-dissolved as well as soil-sorbed E2. The major findings are summarized as follows:

- 1) CMC was able to act as a low-cost and green stabilizer for synthesizing well-stabilized birnessite (δ -MnO₂) nanoparticles. While conventional non-stabilized MnO₂ particles aggregate rapidly, and thus lose their soil deliverability and mobility, CMC-stabilized nanoparticles remain well-dispersed in aqueous suspension for months. The most desired particles (highest reactivity and soil deliverability) were obtained at a CMC/MnO₂ molar ratio of 1.39×10^{-3} , which yielded a mean hydrodynamic size of 39.5 nm and a narrow size distribution (SD=0.8 nm).
- 2) At typical aquatic pH (6-7), CMC-stabilized MnO₂ exhibited faster degradation kinetics for oxidation of 17 β -E2 than non-stabilized MnO₂. This reactivity advantage becomes more evident when used for treating soil-sorbed E2 owing to the ability of CMC to complex with metal ions and shield the reactive sites from binding with soil extracts that inhibit E2 oxidation.
- 3) The retarded first-order kinetic model was able to interpret the E2 oxidation kinetics for CMC-stabilized MnO₂, however, a two-stage model is needed for bare MnO₂ particles.
- 4) When used for degrading soil-sorbed E2, several factors may inhibit the oxidation effectiveness, including desorption rate, soil-MnO₂ interactions, soil-released metals and reductants. CMC-stabilized MnO₂ displayed much greater resistance to the soil inhibitive effects than non-stabilized MnO₂.

Based on the findings, CMC-stabilized MnO₂ nanoparticles hold the potential to be used for facilitating in-situ oxidative degradation of various emerging contaminants in soil and groundwater.

**CHAPTER 3. IN-SITU DEGRADATION OF SOIL-SORBED 17 β -ESTRADIOL
USING CARBOXYMETHYL CELLULOSE STABILIZED MANGANESE OXIDE
NANOPARTICLES: COLUMN STUDIES**

3.1. Introduction

Steroidal hormones are a class of endocrine disrupting chemicals (EDCs), and have been used in almost all combined oral contraceptive pills (Kolpin et al., 2002; Shore and Shemesh, 2003). Exposure to even ng/L levels of the chemicals can cause adverse effects on wildlife and humans via interactions with the endocrine systems, such as abnormal development (e.g., malformations, sex reversal in male species), reproductive disorders, and cancers (Colborn, 1993; Diamanti-Kandarakis, 2009). Over the last decade or so, numerous endogenous and synthetic hormones have been detected in sewage treatment effluents, septic system effluents, surface waters, ground water, and soils worldwide (Kolpin et al., 2002; Shore and Shemesh, 2003; Desbrow et al., 1998; Drewes et al., 2003; Finlay-Moore et al., 2000; Ternes et al., 1999). Municipal wastewater is considered one of the main sources of hormones discharged in the water bodies (Ternes et al., 1999). In addition, animal manure contains large quantities of endogenous hormones (such as estrone (E1), 17 β -estradiol (E2), and testosterone), and application of animal waste as a fertilizer contributes significant amounts of hormones to soil and groundwater (Shore and Shemesh, 2003).

In general, estrogens are subjected to adsorption by soil. As a result, the concentrations in groundwater are lower than in surface waters. However, soil-sorbed

estrogens can be slowly released into groundwater, causing a long-term threat to ecosystems. Kolodziej et al (2004) detected 6.3 ng/L of E2 in a monitoring well located downstream of a waste lagoon. The analysis of 112 samples in 59 groundwater sites in Austria detected E2 in more than 50% of the samples with a maximum concentration of 0.79 ng/L (Hohenblum et al., 2004). Nichols et al. (1998) reported 1-3 µg/L of estrogen and testosterone in rainwater runoff. Yet, there has been no in-situ technology available for degrading estrogens in the subsurface.

Conventional manganese oxide (MnO_2) powder particles have been found effective for oxidizing EDCs such as E2, Tetrabromobisphenol A (TBBPA), and bisphenol A in water (Xu et al., 2008; Jiang et al., 2009; Lin et al., 2009a; Lin et al., 2009b). However, these aggregated particles are not deliverable in contaminated soil/groundwater systems. To facilitate soil deliverability and in-situ remediation of soil, Han et al. (2015) prepared a new class of stabilized MnO_2 (CMC- MnO_2) nanoparticles using a low-cost, food-grade carboxymethyl cellulose (CMC) as a stabilizer, and preliminary batch tests indicated that the new nanoparticles can effectively degrade aqueous and soil-sorbed E2. However, there remains a dearth of pertaining to: 1) detailed transport and deposition behaviors of the nanoparticles in different soils, 2) effectiveness of the nanoparticles when applied in column settings (i.e., under conditions of simulated in-situ soil treatment), and 3) factors that govern the effectiveness of the technology.

Although transport of colloids has been studied for decades, there is limited knowledge of nano-scale particle transport behavior in real natural soils. Studies on the transport of engineered nanoparticles showed that the presence of the polymer and polyelectrolyte coatings can improve particle deliverability in porous media due to their

stabilization of the particles and the increased electrostatic repulsive forces created by carboxylic and phenolic groups (He et al., 2009; Quevedo and Tufenkji, 2012; Wang et al., 2012). In general, laboratory nanoparticle transport tests were conducted in columns using glass beads or pure quartz sand as a model porous matrix. However, variability in the nanoparticles (NPs) breakthrough and retention could be obtained when using a more complex porous media such as natural soil. The composition of soil (e.g., mineral content and organic matter content) differs from locations, and NPs exhibit varying affinity to different soil components. The inherent geochemical and charge heterogeneity of the natural soil is a key factor controlling the nanoparticle deposition. Quevedo and Tufenkji (2012) compared three engineered nanoparticle attachment efficiencies (α) obtained from the breakthrough of loamy sand packed column with quartz sand packed column, and found α values are much higher in the loamy sand than quartz sand. Basnet et al. (2015) observed a notably reduced transport potential of modified Pd-nZVI nanoparticles in loamy sand, and they suggested the high deposition was attributed to the heterogeneities created by the clay fraction. The complex heterogeneity of natural soils presents challenges to develop a correlation between the nanoparticle transport behavior and physicochemical properties of the porous media. Nevertheless, to investigate in-situ remediation efficiency using nanoparticles, studies on nanoparticle transport behavior in natural soils are needed to identify the links between the particle transport and contaminant removal.

Recently, application of nanoparticles for in-situ remediation of soil/groundwater has attracted significant interest. Among various nanoparticles, nano-scale zero-valent iron (nZVI) have been extensively studied and used for in-situ dechlorination of

chlorinated solvents in groundwater aquifers (Bennett et al., 2010; He et al., 2010; Wei et al., 2010). He et al. (2010) tested stabilized ZVI nanoparticles for in-situ destruction of chlorinated ethenes in south US. After two serial injections, the iron nanoparticles that moved five feet down-gradient from the injection well were achieved 70% of recovery (compared with the tracer bromide). After 596 days, the total chlorinated ethenes were decreased by 40% and 61% five and ten feet down-gradient of injection wells, respectively. Although the synthesis method is the same, sometimes the in-situ remediation consequent was quite different. For instance, Zhang and Zhao (2013) synthesized the nZVI particles with the same method as He et al. (2010), and they used the nanoparticles in remediation of chlorinated contaminants in Utah. However, the ZVI deliverability and chlorinated contaminant removal efficiency in their tests were much lower than reported by He et al. (2010) in the sandy aquifer. They suggested that the different soil components and low permeability were the reason that caused significant reduction of the particle deliverability and contaminant removal.

The overall goal of this study was to test the feasibility of the CMC-MnO₂ nanoparticles for in-situ degradation of E2 in soil and groundwater. The specific objectives were to: 1) test and simulate the transport of CMC-MnO₂ through 1-D column tests with three model soils of different properties; 2) determine the effectiveness of CMC-MnO₂ for in-situ degrading soil-sorbed E2; 3) examine the effects of injection velocity and particle concentration on treatment effectiveness; and 4) test effects of soil properties, adsorption/desorption, mass transfer, and particle deposition and identify the key constraints and optimal conditions for the technology.

3.2. Materials and methods

3.2.1 Preparation and characterization of CMC-MnO₂ nanoparticles

CMC-MnO₂ was synthesized following a modified manganese redox method using CMC as a stabilizer. Detailed information on the preparation of CMC-stabilized MnO₂ is provided in 2.2.2 of Chapter 2. The resulting CMC-MnO₂ nanoparticles were aged for one day at room temperature (20±1°C) to allow for full growth before all tests.

TEM images of the nanoparticles were obtained using a Zeiss EM10 transmission electron microscope (Zeiss, Thornwood, NJ, USA). The hydrodynamic particle size and ζ-potential were determined by dynamic light scattering (DLS) (Zetasizer Nano ZS, Malvern Instruments Ltd, Malvern, Southborough, MA, USA). Details of TEM and DLS analyses have been described in 2.2.6 of Chapter 2.

3.2.2 Soils and E2 sorption/desorption

Three sandy loam soils (SL1, SL2, and SL3) were obtained from the bamboo field, corn farm, and wood field, respectively, of the E.V. Smith Research Center of Auburn University in Shorter, AL, USA. Before use, the soils were screened through a standard 2 mm sieve, and then washed with tap water five times to remove debris, fine colloids and water soluble compositions that cannot be separated from water by normal centrifugation. The soil samples were then air-dried, thoroughly mixed, and stored at room temperature (20±1°C) for use. Soil texture, pH, total organic carbon, metal contents, and cation exchange capacity (CEC) were analyzed by the Auburn University Soil Testing Laboratory. Detailed results and analytical methods are described in **Table 3-1**. The pH at point of zero charge (PZC) was determined following the potentiometric titration method (Marcano-Martinez and McBride, 1989), and the particle size distribution was determined following the hydrometer and sieve analysis (Bouyoucos,

1962). **Table 3-1** presents the salient physical and chemical properties of the soils. The key different properties of the soils are the clay content, organic matter (OM) content, and PZC value of the soils. Although the three soils are all sandy loam, the clay content is higher for SL1 (18%) than SL2 (15%) and SL3 (16%). The organic matter content order is SL3 (5.9%) > SL2 (1.3%) > SL1 (0.4%), and the pH of the PZC of the three soils are SL3 (5.9) > SL1 (5.2) > SL2 (4.5).

E2 was pre-loaded on the soils through soil sorption tests of E2. Soil sorption tests of E2 were conducted in 65 mL amber glass vials sealed with open-top screw caps and PTFE-lined septa. Six gram of soil each was weighed in the vials and then wet-autoclaved to eliminate bioactivities in the subsequent tests following the method of Mashtare et al. (2011). The sorption tests were initiated by adding 60 mL of 4×10^{-6} M of an E2 solution to each of autoclaved vials at a soil-to-solution mass ratio of 1:10. After mixing on an end-over-end rotator (40 rpm) for 7 days, the sorption equilibrium for the three soils was reached. The sorption tests resulted in an E2 loading of 0.0019, 0.0065 and 0.0104 mg/g for SL1, SL2 and SL3, respectively, based on initial and final concentrations in the solution. The E2-laden soils were then dried under N₂ atmosphere. The E2 loadings were determined per hot methanol extraction, where the soil is mixed with methanol at a soil-to-methanol ratio of 3 (g):20 (ml) and in a hot water bath at 70°C for 4 hours. The recovery of using this hot methanol method to extract E2 was determined to be 94±4%, 91±4% and 86±4%, for SL1, SL2, and SL3, respectively.

To probe the desorption rates of the soil-sorbed E2, desorption kinetic tests were carried out following the successive desorption method. Successive desorption kinetic tests were conducted with the same batch reactors. Following the sorption equilibrium,

the soil and solution were separated through centrifugation at 805 g-force, and desorption of E2 was initiated by replacing ~57 mL (95%) of the supernatant with the same volume of soil-amended water (prepared by mixing the soil and water at the same soil:solution ratio). The vials were then mixed on the rotator at 40 rpm in an incubator. At selected times, duplicate vials were sacrificially sampled and analyzed for E2 in water following the same procedure as in the sorption tests. Upon equilibrium, the soil and solution were separated again through centrifugation, and the second run of desorption was initiated by replacing ~57 mL of the supernatant with the same volume of E2 free soil-amended water. At selected times, E2 in the supernatant was analyzed following the same procedure.

Table 3-1. Physical and Chemical Properties of the Three Soils Used in This Work

Soil	Taxonomy ^a	Clay ^a , %	CEC ^b meq/100g	OM ^c , %	pH	PZSE ^e	Ca ^f ppm	K ppm	Mg ppm	P ppm	Al ^g ppm	Cu ppm	Fe ppm	Mn ppm	Zn ppm	Na ppm	As ppm	Cd ppm	Cr ppm	Pb ppm
SL1	Sandy Loam	18	3.20	0.4	6.7	5.2	234	51	71	11	72	3	25	22	2	4	<0.1	<0.1	<0.1	<0.1
SL2	Sandy Loam	15	3.69	1.3	5.9	4.5	392	18	50	12	130	4	24	18	2	33	<0.1	<0.1	<0.1	<0.1
SL3	Sandy Loam	16	28.94	5.9	7.8	5.9	4612	77	497	109	3	<0.1	<0.1	31	1	53	<0.1	<0.1	<0.1	<0.1

^a Soil texture analysis was conducted following the Bouyoucos hydrometer method (Bouyoucos, 1962).³

^b CEC: Cation exchange capacity, measured per EPA Method 9081.

^c Organic carbon was determined following the combustion method (Kirsten, 1979).

^d pH of soil was analyzed in a soil-to-DI water volume ratio of 1:1.

^e The pH at point of zero salt effect (PZSE) of the soil was measured following the potentiometric titration method (Marcano-Martinez and McBride, 1989).

^f Soil potassium, calcium, magnesium, phosphate and sodium were extracted following Melich I procedure.

^g Soil metal contents were acid digested following EPA method 3230.

3.2.3 Column transport tests

The transport behavior of CMC-MnO₂ in the model soils was examined through column breakthrough tests using a glass column (ID = 1 cm, L = 15 cm) with adjustable headspace (Omnifit, Cambridge, England). A layer of 0.3-cm thick glass wool was packed at the bottom and top of the soil bed. In each test, a dry mass of 12 grams of a soil was packed in the column with a constant porosity. Each column was slow flushed (0.03 ml/min) with ~10 pore volumes (PVs) of a nitrogen-sparged background solution (0.84 mM NaCl+0.16 mM NaHCO₃, pH=7.5) in the up-flow mode to avoid air entrapment and achieve complete water saturation. The breakthrough test was then initiated by pumping a suspension of CMC-MnO₂ through the soil bed in the up-flow mode using a HPLC pump (Acuflow series II pump, Lab Alliance, USA) with Teflon tubing. The effluent samples were collected by a fraction collector (Eldex, CA, USA), then each 2 mL of the samples was mixed with 0.5 mL of ascorbic acid (0.05 M) to completely dissolve the nanoparticles, and the CMC-MnO₂ effluent history was obtained by measuring the total Mn concentration. Following the full breakthrough, the influent reservoir was switched to the background solution at the same flow rate to elute the retained nanoparticles. Bromide tracer (KBr as 30 mg/L) tests were conducted under the same condition of breakthrough tests to acquire the hydrodynamic parameters of the column. To investigate the spatial distribution of the nanoparticles delivered in the soil, the soil beds were sectioned into 5 segments, and the concentration of the nanoparticles in each section was obtained via EPA Method 3050B (acid digestion). A summary of experiment conditions is provided in **Table 3-2**, and the column experiment setup is shown in **Figure 3-1**.

Table 3-2. Experiment conditions of MnO₂ transport tests conducted at various velocities and concentrations in saturated columns packed with different porous media

Soil	Bed depth cm	Flow rate mL/min	Pore velocity cm/min	EBCT ^a min	Injection MnO ₂ conc. g/L	Pulse Duration PV	Grain size ^b mm	Bulk density g/cm ³	Porosity	Saturated hydraulic conductivity ^c cm/day
SL1	9.4	0.05	0.167	147.7	0.017	9.9	0.101	1.60	0.38	5.69±0.08
SL2	8.4	0.05	0.202	131.9	0.017	11.9	0.098	1.80	0.32	6.16±0.07
	8.4	0.2	0.808	33.0	0.017	14.8	0.098	1.80	0.32	6.16±0.07
	8.4	0.03	0.121	219.9	0.017	11.4	0.098	1.80	0.32	6.16±0.07
	8.4	0.01	0.040	659.7	0.017	11.8	0.098	1.80	0.32	6.16±0.07
	8.4	0.05	0.202	131.9	0.087	12.3	0.098	1.80	0.32	6.16±0.07
	8.4	0.05	0.202	131.9	0.174	12.3	0.098	1.80	0.32	6.16±0.07
SL3	10.6	0.05	0.153	166.5	0.017	7.2	0.083	1.44	0.42	3.50±0.05

^a EBCT is the empty bed contact time. ^b Mean grain diameter is determined following the hydrometer and sieve analysis (Bouyoucos, 1962). ^c Saturated hydraulic conductivity is determined following the constant head method.

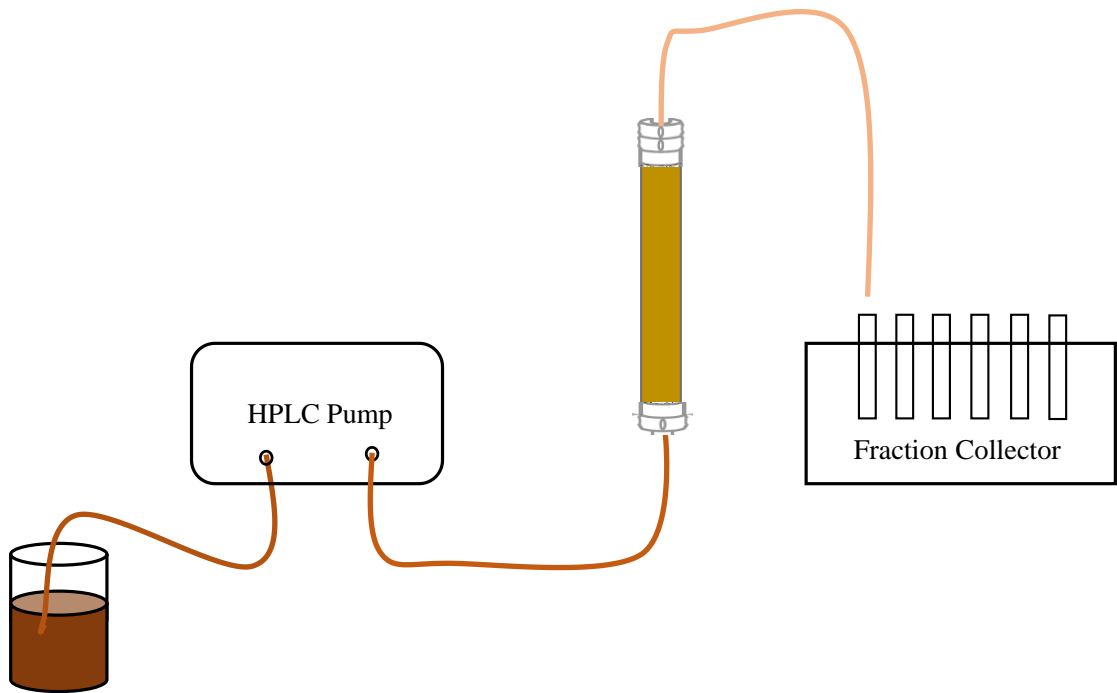


Figure 3-1. Column experiment setup

3.2.4 Column degradation tests

Column tests were carried out to simulate in-situ treatment of E2-contaminated soil. In each case, 12 grams of a soil were dry-packed in the column under constant patting with a glass bar, with the soil porosity (bed height) being kept the same as in the transport tests. Column degradation tests were initiated by pumping a CMC-MnO₂ suspension through the column at a constant rate, and effluent was collected immediately into a glass tube containing 1 mL of 10 g/L ascorbic acid. The effectiveness of ascorbic acid for dissolution of MnO₂ and termination of the reaction has been shown by Xu et al. (2008). Upon filtration through an Anotop 10 syringe filter (0.22 μm alumina membrane), the filtrate was analyzed by HPLC for E2. The control tests were conducted by pumping through the same concentration of CMC solution as in degradation tests, but without MnO₂ nanoparticles, and the other experiment conditions were kept identical as degradation tests. E2 remaining in the soils after column degradation tests was determined through the hot methanol extraction method.

3.2.5 Analytical method

Bromide concentration was measured using a Dionex Ion Chromatography (DX-120, Dionex, Sunnyvale, CA), with a detection limit <0.05 mg/L. Total manganese was analyzed with a flame atomic-absorption spectrophotometer (AAS) (220FS, Varian, Palo Alto, CA) with a detection limit of 0.05 mg/L. E2 was analyzed using an HP Agilent 1260 Infinity HPLC system equipped with a Poroshell 120 EC-C18 column (4.6×50mm, 2.7 μm) and by modifying the method by Havlikova et al (2006). The mobile phase was a mixture of 40:60 (v/v) of acetonitrile and phosphoric acid (0.085%) at a flow rate of 1

mL min⁻¹. A UV detector (G1365D 1260 MWD VL) was operated at a wavelength of 210 nm, giving a detection limit of 5×10⁻⁸ M.

3.2.6 Transport modeling

The one-dimensional advection-dispersion equation (ADE) that accounts for advection, dispersion, and solid-phase deposition was used to simulate the transport behavior of CMC-MnO₂ through the water-saturated soils (Wang et al., 2008):

$$\frac{\partial C}{\partial t} = \lambda v_p \frac{\partial^2 C}{\partial z^2} - v_p \frac{\partial C}{\partial z} - \frac{\rho_b}{\theta_w} \frac{\partial S}{\partial t} \quad (3-1)$$

where C is the MnO₂ concentration in the aqueous phase (N_cL⁻³), N_c is the number of particles, S is the MnO₂ concentration in the solid phase (N_cM⁻¹), M is the mass of solid phase (only in chapter 3.2.6), z is the distance along the column from the inlet (L), t is the time (T), λ is the dispersivity (L), v_p is the average pore velocity (LT⁻¹), ρ_b is the soil bulk density (ML⁻³), and θ_w is the water content, which is equal to porosity under saturation condition. The accumulation of CMC-MnO₂ onto the soil is given by (Bolster et al., 1999):

$$\frac{\rho_b}{\theta_w} \frac{\partial S}{\partial t} = k_{dep} \psi C - \frac{\rho_b}{\theta_w} k_{det} S \quad (3-2)$$

where k_{dep} is the first-order deposition coefficient of CMC-MnO₂ [T⁻¹], k_{det} is first-order detachment coefficient [T⁻¹], and ψ is a dimensionless blocking function to describe the change of the available fraction of deposition surface sites.

A simple Langmuirian blocking function, which was derived from the Langmuir adsorption model, was used to account for the dynamic blocking (Adamczyk et al., 1994):

$$\psi = \frac{S_{max} - S}{S_{max}} \quad (3-3)$$

where S_{max} is the maximum MnO_2 deposition capacity [N_cM^{-1}]. In case of negligible release of nanoparticles from sand grains, detachment coefficient k_{det} approaches zero, and Eqn (3-2) reduces to an irreversible deposition kinetic. The HYDRUS-1D code was used to solve Eqs (3-1)-(3-3) (Simunek et al., 2005). The details of parameters used in this chapter were provided in **Appendix A**.

3.3. Results and discussion

3.3.1 Characterization of CMC-stabilized MnO_2 nanoparticles

Figure 3-2 shows digital photographs and TEM images of non-stabilized MnO_2 particles and CMC-stabilized particles prepared at a molar ratio of $CMC/MnO_2 = 1.39 \times 10^{-3}$. The CMC stabilization resulted in fully stabilized discrete nanoparticles which could be well suspended for several months, with a TEM image based average diameter of 36 ± 10 nm. In addition, DLS measurements gave a mean volume weighted hydrodynamic size of 39.5 ± 0.8 nm, and a zeta-potential of -34 ± 2 mV ($MnO_2 = 0.017$ g/L, $pH = 5.1$, $I \cong 2.4 \times 10^{-4}$ M) for CMC- MnO_2 which indicate a good stabilization of the nanoparticles due to electrostatic repulsion. In the experiment concentration range of 2×10^{-4} M (0.017 g/L) to 2×10^{-3} M (0.174 g/L), the hydrodynamic size and zeta-potential of MnO_2 nanoparticle did not vary much, the average hydrodynamic size was within 42 ± 2 nm to 39.5 ± 0.8 nm, and the zeta-potential was within -34 ± 2 mV to -32 ± 3 mV. The X-ray Diffraction (XRD) analysis showed the synthesized non-stabilized and CMC-stabilized MnO_2 are all largely amorphous, and indicated the synthesized MnO_2 particles are birnessite (δ - MnO_2) (Murray, 1974; Zhang and Huang, 2003).

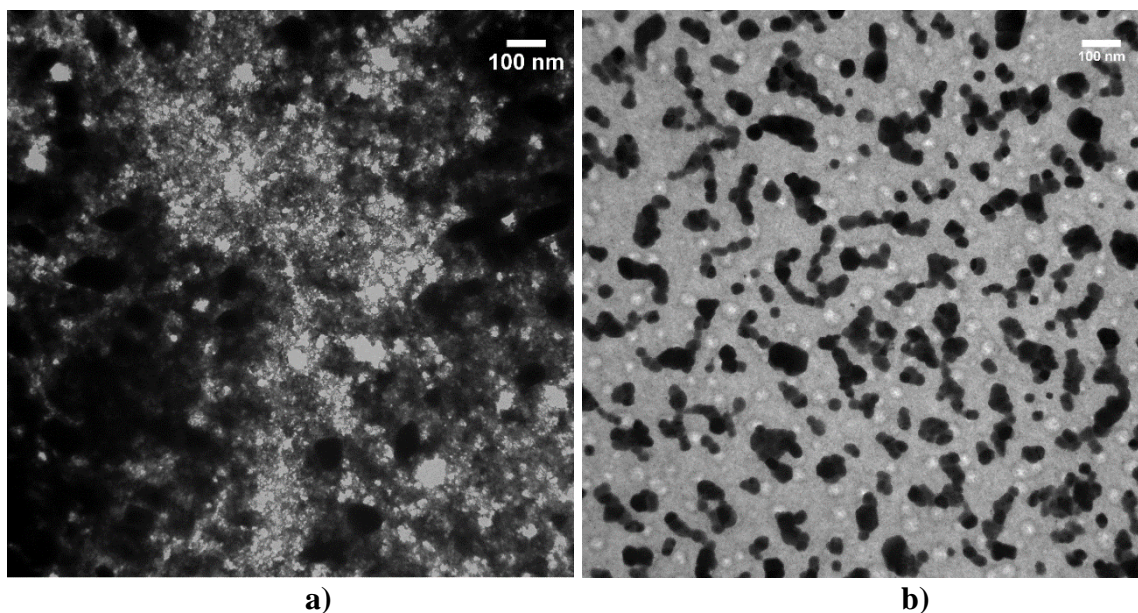


Figure 3-2. Photographs and TEM images of: (a) non-stabilized MnO₂, and (b) CMC-stabilized MnO₂ particles. Pictures were taken 30 minutes after synthesis. [MnO₂] = 8×10^{-4} M (0.07 g/L) for both cases, and CMC/MnO₂ molar ratio = 1.39×10^{-3} for case b).

3.3.2 Transport of CMC-MnO₂ in three soils

Figure 3-3(a)-(c) shows the measured and fitted breakthrough curves (BTCs) of tracer (KBr) and CMC-MnO₂ transport through the three sandy loam soils. **Table 3-2** summarizes experiment conditions of the transport tests. The results of duplicate experiments under identical conditions are presented in **Figure 3-4** to demonstrate the reproducibility of the experimental system. In all cases, the effluent bromide concentration rapidly reached influent concentration at ~ 1.3 PVs (the number of pore volumes (PVs) is equivalent to a dimensionless time), and decrease sharply to zero upon pumping through background solution. For MnO₂ nanoparticles, the effluent concentrations were increased more gradually after breakthrough and then reached a plateau, although the plateau relative concentration (C/C_0) was different for the three soils. For SL1 soil, MnO₂ breakthrough at ~5 PVs with the average plateau C/C_0 was 0.90, and the plateau exhibited a slightly ascent until the influent was switched to background solution. For SL2 soil, the average plateau C/C_0 was 0.93 with a fast breakthrough at ~2 PVs. For SL3 soil, the breakthrough of MnO₂ occurred at also ~2 PVs, but the effluent plateau relative concentration was the lowest, with a C/C_0 of 0.66. This behavior suggested that although MnO₂ could attach to different soils by a different extent, the synthesized nanoparticles were deliverable in natural sandy loam soils. **Table 3-3** shows the simulation parameters obtained by fitting BTCs of column experiments and calculated MnO₂ retention parameters. The longitudinal dispersivity λ for each medium was obtained by fitting the classic ADE (no deposition term) to tracer BTCs. The deposition coefficient k_{det} and maximum deposition concentration S_{max} are obtained by fitting the modified ADE (include deposition term) to MnO₂ BTCs. The

numerical model was able to nicely simulate the tracer and MnO₂ nanoparticle BTCs with a coefficient of determination (R^2) > 0.98.

The retention profiles of MnO₂ nanoparticles are presented in **Figure 3-3(d)** as a function of distance from the inlet. The result showed that the retention of CMC-MnO₂ nanoparticles was about one order of magnitude lower in SL2 than in SL1 and SL3. Consistent with the retention profile, compared the integrated area of BTCs (effluent MnO₂ mass) with the total injected mass of nanoparticles showed the retention of CMC-MnO₂ was 37.1 %, 4.3 % and 36.4 % for SL1, SL2 and SL3 soil, respectively, of the total injected mass of MnO₂ (**Table 3-3**). Comparing the retained plus eluted mass with the total mass injected, the total measured mass balance of MnO₂ for the three experiments was ranged from 93.5% to 111.4% which confirms the mass balance closure of the transport experiments (**Table 3-3**).

From **Figure 3-3**, it was noted that the deposition of MnO₂ is higher in SL1 and SL3 soils, and breakthrough of CMC-MnO₂ was apparently retarded in SL1 soil than other two soils. While the breakthrough occurred at ~2 PVs for SL2 and SL3 soils, it occurred at ~5 PVs for SL1 soil. Such a time delay of the BTCs was also observed in other engineered nanoparticles transport in porous media (Jones and Su, 2014; Li et al., 2008). The deposition rate of nanoparticles in porous media depends on 1) the available solid surface area that is favorable for deposition (related to S_{max}^*); and 2) the mass transfer rate of the nanoparticles to the favorable sites where deposition can occur (related to k_{dep}) (Ko and Elimelech, 2000; Sasidharan et al., 2014; Torkzaban et al., 2010). Under the experiment conditions presented here (i.e., the pH of influent MnO₂ suspension was 5.1-5.3), the MnO₂ nanoparticles (pH of point of zero charge

($\text{pH}_{\text{pzc}}=2.25$) were negatively charged, which was confirmed by the highly negative zeta-potential (-34 mV). As the pH_{pzc} for soil SL1, SL2, and SL3 was measured to be 5.2, 4.5, and 5.9 respectively, the soil surface is negatively charged for SL2, partially positively charged for SL1 and positively charged for SL3, which indicates SL1 and SL3 soil provided more favorable surfaces for the deposition of the negatively charged MnO_2 NPs. Consistent with the PZC value, the deposition of MnO_2 was apparently higher for SL1 (37.1 %) and SL3 (36.4 %) soils than SL2 (4.3 %) soil. In addition, the model fitted data shows the maximum deposition sites S_{max}^* for SL3 soil ($1.42 \times 10^{-1} \text{ m}^3/\text{g}$) is two orders of magnitude larger than SL1 ($1.51 \times 10^{-3} \text{ m}^3/\text{g}$) and SL2 ($1.28 \times 10^{-3} \text{ m}^3/\text{g}$) soils. These findings clearly indicate that the large favorable solid surface area contributes most for MnO_2 deposition in SL3 soil, which resulted in a low plateau relative concentration ($C/C_0=0.66$) in effluent.

The observed delays in the BTCs for SL1 soil suggested a higher initial MnO_2 deposition (attachment) rate. The high initial rates may be explained by the high mass transfer rate of the nanoparticles from bulk solution to the favorable solid surface sites (Torkzaban et al., 2010). The diffusive mass transfer rate of the colloids was considered relevant to the deposition coefficient (Sasidharan et al., 2014; Torkzaban et al., 2010). The first-order deposition coefficient k_{det} fitted in the model for SL1 (0.252) is two orders of magnitude larger than SL2 (0.001) and SL3 (0.004), indicating a faster deposition rate. To further study the deposition kinetics of MnO_2 nanoparticles to the three soils, batch soil adsorption experiments were conducted, and the CMC- MnO_2 sorption kinetics are shown in **Figure 3-5**. Although batch adsorption kinetics could not fully represent column deposition kinetics, they could illustrate the interaction energies between the

particles and soils. **Figure 3-5** shows that the initial MnO₂ adsorption is faster in SL1 soil than the other two soils, while the adsorption extent in SL3 is the highest. At equilibrium, MnO₂ adsorption was 0.139 mg/g, 0.119 mg/g, and 0.145 mg/g for SL1, SL2, and SL3, respectively. This observation also demonstrates that the MnO₂ mass transfer from solution to solid surface is fastest for SL1 soil, and the favorable surface area for deposition is biggest in SL3 soil.

The results suggested MnO₂ deposition is much higher in the soil that offer more favorable deposition sites than those that are unfavorable for deposition which could be predicted based on the collector (grain) average surface potential (PZC value) (Torkazaban et al., 2010). In addition, the surface charge heterogeneity on mineral surfaces is considered to play an important role in colloid deposition (Sasidharan et al., 2014; Johnson et al. 1996; Rizwan and Bhattacharjee, 2009). Torkazaban et al. (2010) found the gold nanoparticles deposited only on the clay surfaces, and did not deposit on the sand removed of clay particles. They suggested surface charge heterogeneities on clay particles are key factors controlling the deposition of nanoparticles on solid surface. In our case, the soil analysis (**Table 3-1**) showed the clay content is 18%, 15%, and 16%, suggesting a high surface charge heterogeneities for SL1 soil.

Table 3-3. Simulation parameters obtained by fitting breakthrough curves of column experiments to the model.

Soil	v_p^a	C_0^b	Ret. ^c	MB ^d	λ^e	k_{dep}^f	S_{max}^{*g}	R ²
	cm/min	g/L	%	%	cm	min ⁻¹	m ³ /g	
SL1	0.169	0.017	37.1	93.5	0.359	0.252	1.51×10^{-3}	0.992
SL2	0.202	0.017	4.3	111.4	0.207	0.001	1.28×10^{-3}	0.991
	0.808	0.017	0.7	-	0.423	0.001	1.86×10^{-4}	0.987
	0.121	0.017	33.1	-	0.070	0.003	5.75×10^{-1}	0.995
	0.040	0.017	81.1	-	-	-	-	0.612
	0.202	0.087	6.8	-	0.207	0.001	3.29×10^{-3}	0.998
	0.202	0.174	6.9	-	0.207	0.001	4.22×10^{-3}	0.998
SL3	0.153	0.017	36.4	96.0	0.395	0.004	1.42×10^{-1}	0.981

^a Pore velocity. ^b Injection MnO₂ concentration. ^c Retention of CMC-MnO₂, Ret.= $1-M_{eff}/M_{inj}$, where M_{eff} is the effluent mass of MnO₂ calculated by integrating the BTCs, M_{inj} is the total injected mass of MnO₂. ^d Mass balance of MnO₂. ^e Longitudinal dispersivity.

^f First-order deposition coefficient. ^g $S_{max}^*=S_{max}/C_0$, where S_{max} is the maximum MnO₂ deposition concentration.

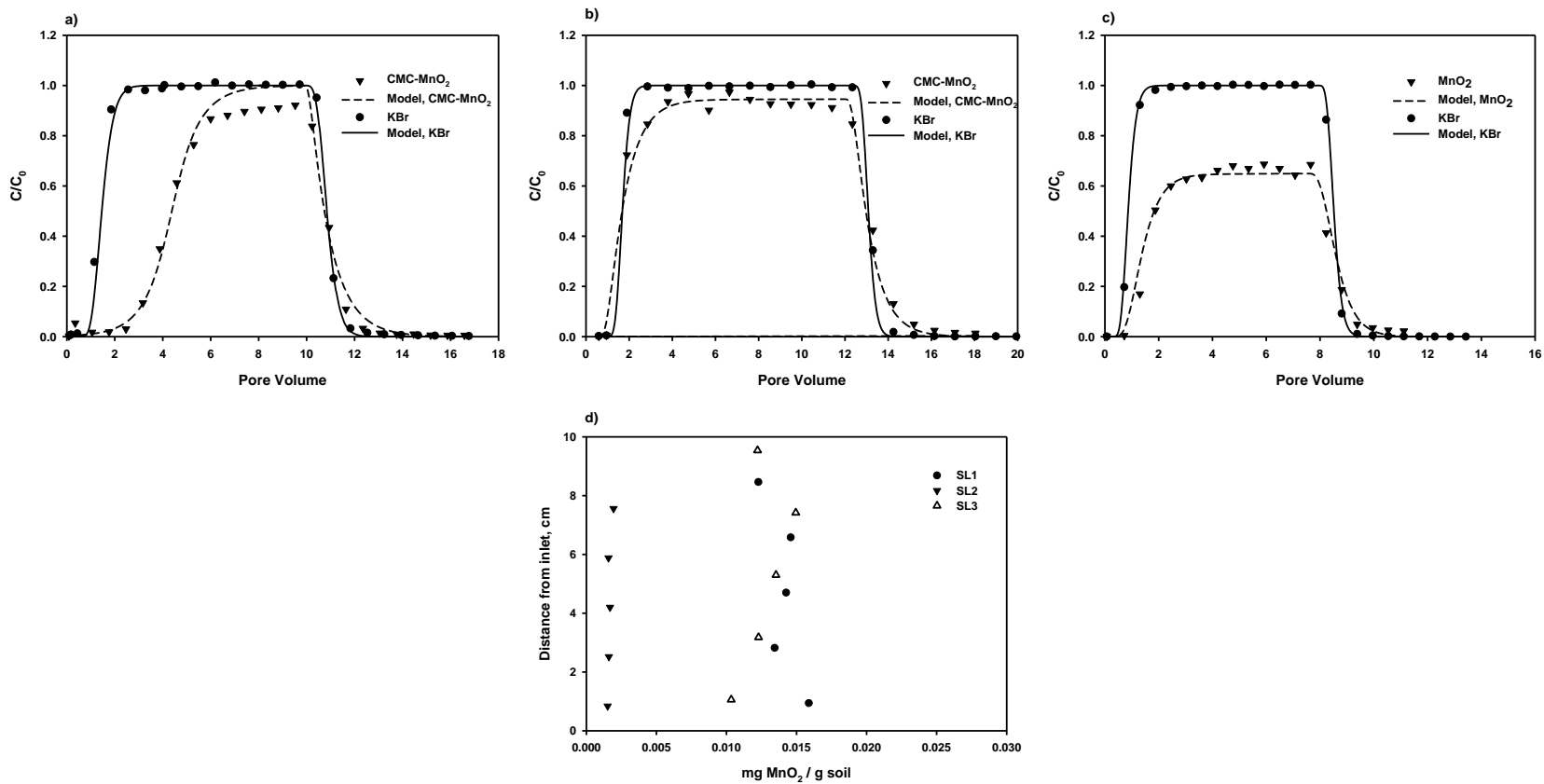


Figure 3-3. Measured and fitted breakthrough curves of a KBr tracer and CMC-MnO₂ nanoparticles through: (a) SL1 soil, (b) SL2 soil, (c) SL3 soil, and nanoparticle retention profiles (c) obtained after MnO₂ transport through the three soils. Experiment conditions: [KBr] = 30 mg/L, [MnO₂] = 0.017 g/L (2×10^{-4} M), [CMC] = 25 mg/L, inlet flow rate = 0.05 ml/min, soil = 12 g. Following full breakthrough, the influent was switched to the tracer (nanoparticle) free background solution. The number of pore volumes (PVs) is equivalent to a dimensionless time. One pore volume (1 PV) = bed volume of the 12 g soil \times porosity, and PVs = volume of influent suspension (flow rate \times time) / 1 PV.

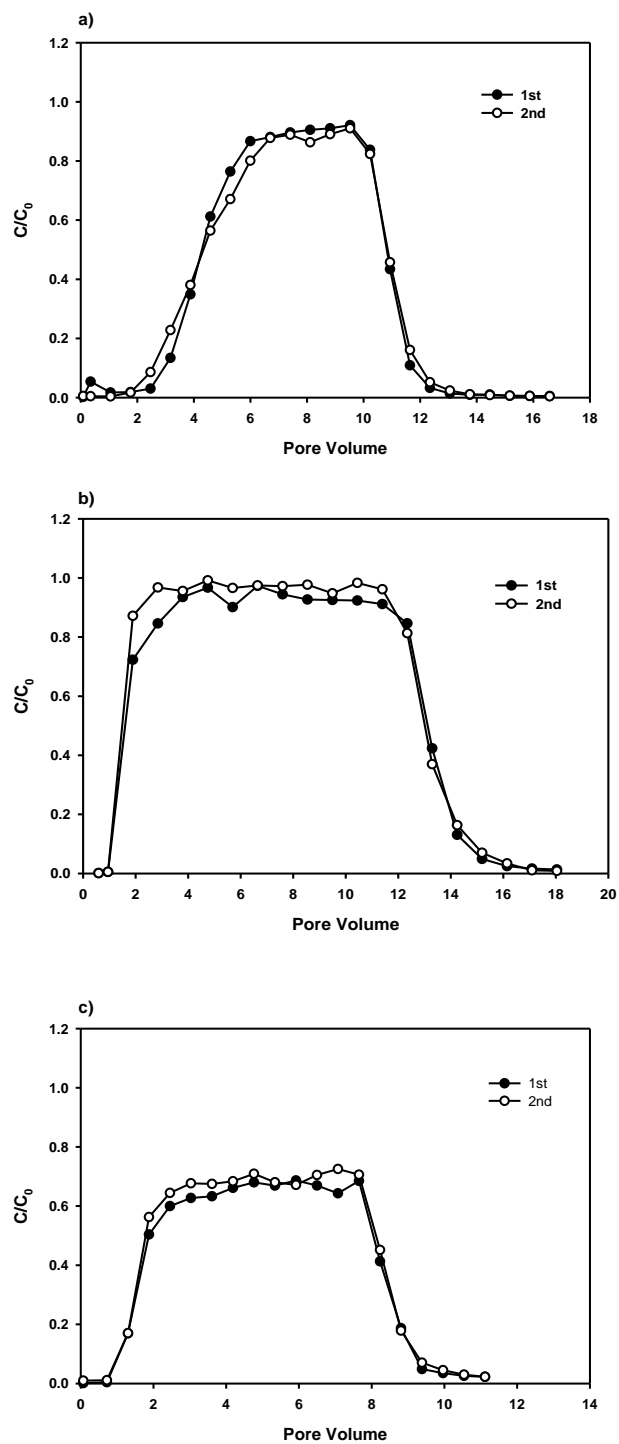


Figure 3-4. Measured duplicate breakthrough curves of CMC-MnO₂ nanoparticles through: (a) SL1 soil, (b) SL2 soil, and (c) SL3 soil. Experiment conditions: [MnO₂] = 0.017 g/L (2×10^{-4} M), [CMC] = 25 mg/L, inlet flow rate = 0.05 ml/min, soil = 12 g.

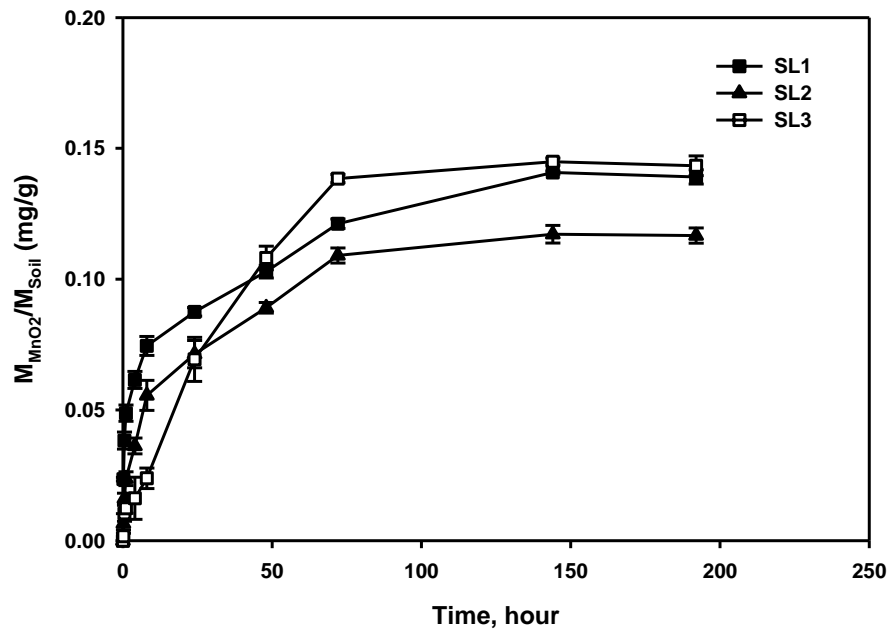


Figure 3-5. MnO₂ sorption kinetics in three soils. Experiment conditions: [MnO₂] = 0.017 g/L (2×10^{-4} M), [CMC] = 25 mg/L, soil-to-MnO₂ suspension ratio of 1 (g):10 (mL).

3.3.3 Effect of flow velocity on transport behavior

The effect of flow velocity on CMC-MnO₂ transport was investigated for the SL2 soil. **Figure 3-6** shows the BTCs of CMC-MnO₂ nanoparticles under different pore velocities ranging from 0.040 to 0.808 cm/min. Results in **Figure 3-6** and **Table 3-3** show that when the velocity increase from 0.202 cm/min to 0.808 cm/min, the breakthrough occurred almost simultaneous at ~2PV, however, the full breakthrough level C/C_0 was increased from 0.93 to almost 1.0. Consistent with BTCs, the model fitting reduces S_{max}^* from 1.28×10^{-3} m³/g to 1.86×10^{-4} m³/g and keeps k_{dep} at 0.001 min⁻¹. The small retention value (0.7%) indicates negligible deposition of the nanoparticles at this velocity. Conversely, when the velocity was reduced from 0.202 cm/min to 0.121 cm/min, 28.8% more nanoparticles were retained, which can be attributed to the increase in S_{max}^* (5.75×10^{-1} m³/g) and k_{dep} (0.003 min⁻¹). Meanwhile, the BTCs of MnO₂ was delayed to ~4 PVs and the full breakthrough level C/C_0 was decreased to 0.63. According to Darcy's law, when the injection velocity is 0.202 cm/min and 0.121 cm/min, the injection pressure needs to be 2.14 psi and 1.29 psi, respectively, which suggests that the CMC-stabilized MnO₂ nanoparticles are deliverable in natural soils under relatively low injection pressure.

When the velocity was reduced furthermore to 0.040 cm/min the applied model could not fit the data well, as it seems the effect of deposition is beyond the classical filtration theory which considers attachment of particles is primarily a function of solution chemistry and colloid properties. Decreasing the flow velocity will decrease the magnitude of lift and drag force acting on the particles near solid surfaces and increase particle contact time with solid surfaces. As a result, low flow rate will promote particle

deposition in small pores (Bergendahl and Grasso, 2000). Once a large amount of particles has been deposited in the small pores near the inlet, they will block other particles from passing, as the particles are accumulated, the large pores become smaller and smaller, and the effluent of MnO_2 was decreased (**Figure 3-6**). When the nanoparticles completely block the inlet, the nanoparticle effluent becomes zero. This result suggests that under groundwater flow velocity, the natural transport of CMC- MnO_2 is rather confined.

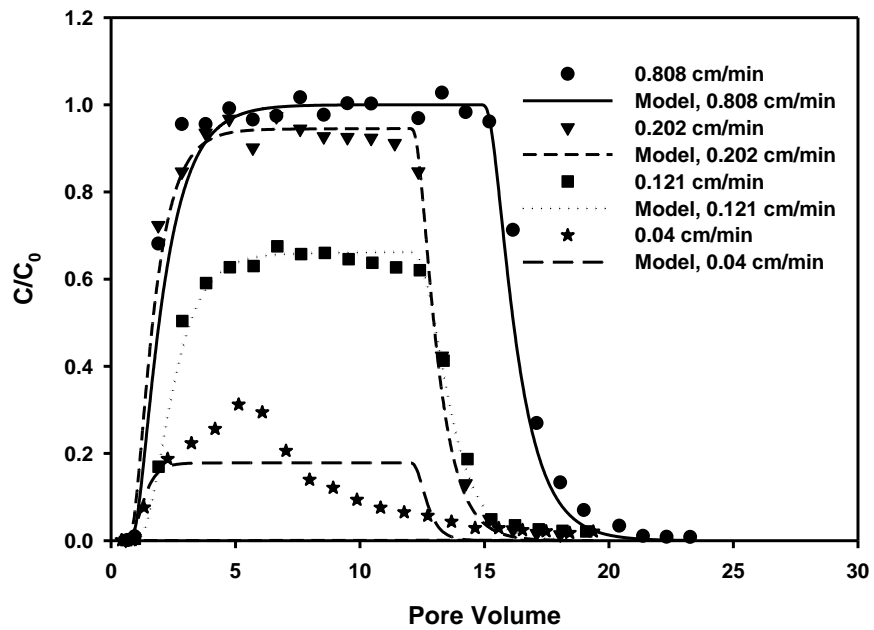


Figure 3-6. Breakthrough curves of CMC-MnO₂ nanoparticles through SL2 soil at different pore velocities. Experiment conditions: [MnO₂] = 0.017 g/L (2×10^{-4} M), [CMC] = 25 mg/L, soil = 12 g.

3.3.4 Effect of nanoparticle concentration on transport behavior

Figure 3-7 shows the BTCs of CMC-MnO₂ nanoparticles under different MnO₂ concentrations ranging from 0.017 g/L to 0.17 g/L. The result shows that the normalized effluent concentration C/C_0 was almost unchanged with the elevated inlet concentrations. In the concentration range of the experiment, the breakthroughs of MnO₂ all occurred at ~2 PVs, and the full breakthrough level C/C_0 were all approximately to 0.93. Consistent with the BTCs, the model fitted k_{dep} values were similar in the three tests (**Table 3-3**). The normalized S_{max}^* value ($S_{max}^* = S_{max}/C_0$) is increased slightly with increasing initial MnO₂ concentration, and the S_{max}^* is 1.28×10^{-3} , 3.29×10^{-3} , and 4.22×10^{-3} for initial concentration C_0 of 0.017 g/L, 0.087 g/L, and 0.174 g/L respectively. The DLS measurement showed the particle size was 39.5 ± 0.8 nm, 40 ± 1 nm, and 42 ± 2 nm, and δ -potential was -34 ± 2 mV, -32 ± 3 mV, and -33 ± 2 mV for the particle concentration of 0.017 g/L, 0.085 g/L, and 0.17 g/L, respectively. This result agreed with clean bed filtration theory, which means that once the particle size and potential energy of the nanoparticles are identical, the concentration of particle did not influence the deposition behavior. These results thereby suggest that the synthesized CMC stabilized nanoparticles deliver well in soil even at higher MnO₂ concentration which may be required for site remediation.

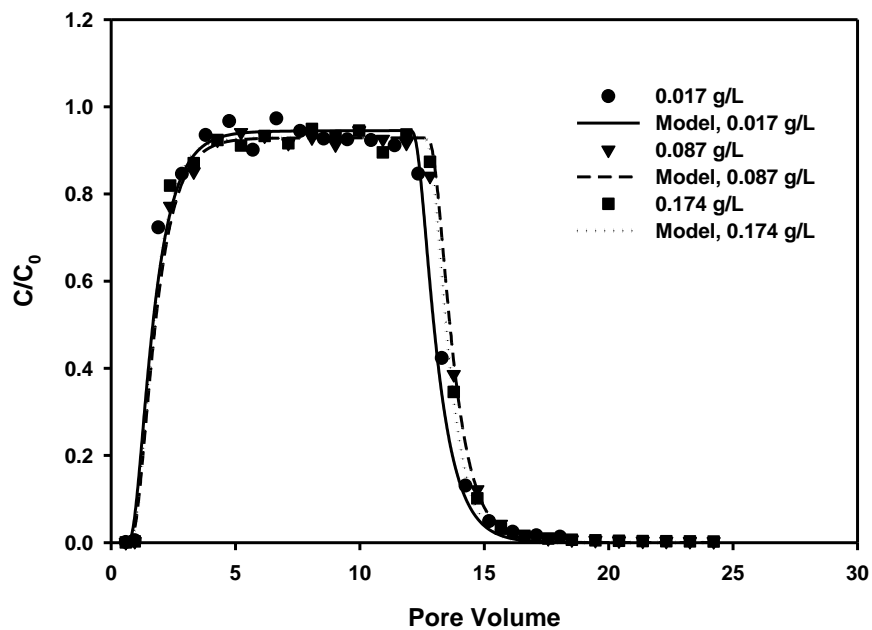


Figure 3-7. Breakthrough curves of different concentrations of CMC-MnO₂ nanoparticles through SL2 soil. Experiment conditions: [MnO₂] = 0.017 g/L (2×10^{-4} M), [CMC] = 25 mg/L, soil = 12 g.

3.3.5 Degradation of E2 in three soils

The effectiveness of the CMC-stabilized MnO₂ nanoparticles for in-situ degradation of E2 in soil was investigated through a series of 1D column experiments. **Figure 3-8(a)-(c)** shows the elution histories of E2 from SL1, SL2, and SL3 soil during the nanoparticle treatments. For comparison, the same elution test was also carried out using a CMC solution without the nanoparticles under otherwise identical conditions (control). To confirm the reproducibility of the experimental system, duplicates were conducted and results are shown in **Figure 3-9**. **Figure 3-8** shows that under identical conditions, nanoparticle suspension eluted less E2 than particle-free solution through the three soils. Han et al. (2015) demonstrated soil-sorbed E2 could be oxidatively destroyed by CMC-stabilized MnO₂ nanoparticles through batch tests. The decreasing of E2 elution in MnO₂ treated columns were due to oxidative degradation of E2 by the nanoparticles.

The E2 degradation efficiency in different soils are shown in **Table 3-4**. For SL1, the CMC solution eluted ~72% of E2 initially sorbed in the soil, while the nanoparticle suspension eluted ~56% of E2 during the 20 PVs of the column runs (**Figure 3-8(a)**), i.e., the nanoparticle treatment degraded ~22% of the water leachable E2. For SL2, after nanoparticle treatment, leachable E2 was reduced from ~67% to ~8% (**Figure 3-8(b)**), i.e., the nanoparticles were able to degrade ~88% of water leachable E2 from SL2. For SL3 soil (**Figure 3-8(c)**), after treatment, leachable E2 was reduced from ~8% to ~7%, i.e., the nanoparticles degraded ~13% of the water leachable E2. To investigate total E2 degradation by nanoparticles, E2 remaining in the soil was extracted and analyzed. For SL1, after CMC solution flushing, E2 residual in soil was ~20% of E2 initially sorbed in the soil, while E2 residual was reduced to ~17% after treatment with nanoparticles

(Table 3-4), i.e., the nanoparticle treatment degraded ~15% of the non-leachable E2 during the 20 PVs of the column runs. For SL2, E2 remaining in the soil was reduced from ~24% to ~14% after nanoparticle treatment, i.e., the nanoparticles degraded 42% of the non-leachable E2. For SL3, E2 remaining in the soil was reduced from 75% to 61% after degradation with nanoparticle suspension, i.e., the nanoparticles were able to degrade 19% of the non-leachable E2. Based on mass balance, addition of E2 eluted and remaining in soil, E2 recovery was 92%, 91%, and 83% for SL1, SL2, and SL3 when pumping through CMC solution (control test), respectively. The loss of E2 in the control test was probably due to adsorption of E2 in the PTFE tubing and soil loss in the process of transfer from column to extraction bottles. These results indicate pumping through MnO₂ nanoparticles could not only degrade water-leachable E2 but also soil immobilized E2.

The E2 sorption capacity for the three soils are different. The E2 sorption was the lowest in SL1 with a loading mass of 0.0019 mg-E2/g-soil compared to SL2 (0.0065 mg-E2/g-soil) and SL3 (0.0104 mg-E2/g-soil). In contrast, when flushing with CMC solution, the elution of E2 was highest for SL1 soil with an elution concentration >1 mg/L in first 2.5 PVs (Figure 3-8). These results indicate a weak binding of E2 to SL1. Compared to SL1, E2 elution is much slower in SL2 and SL3, and the highest elution concentration was 0.43 mg/L and 0.05 mg/L, respectively. To further study the E2 mass transfer from the soils, E2 successive desorption batch tests were conducted and results are shown in Figure 3-10. Consistent with the E2 elution history, E2 desorption was highest in SL1, and ~30% of initial sorbed E2 was able to desorb from soil in 20 min. After the second desorption batch, ~70% of the initial E2 was desorbed from SL1 soil which corresponds

with 68% elution of E2 by CMC solution. For SL2, ~15% of initial sorbed E2 was desorbed in 20 min, and ~40% of the initial E2 was desorbed from soil after the second desorption run. For SL3 soil, only ~4% of the initial loaded E2 was desorbed from soil after two runs of desorption batch. The disparate sorption affinity of E2 to soils is due to the different organic matter (OM) content of the soils, for instance, the OM content is 0.4%, 1.3%, and 5.9% for SL1, SL2, and SL3, respectively. The dominant E2 sorption mechanism is reported to be hydrophobic partitioning (Lee et al. 2003), thus higher OM content soil have higher affinity to this hormone.

It is noted from **Figure 3-8** that the MnO₂ degradation efficiency of water leachable E2 is much higher for SL2 than SL1 and SL3. The results indicate that the effectiveness of the stabilized MnO₂ nanoparticles is affected by both mass transfer of E2 and MnO₂, i.e., the desorption rate of E2 from soil and transport of the nanoparticles through the soil. SL1 has a much lower adsorption capacity for E2, but a much faster desorption rate (as indicated by the high elution peak in **Figure 3-8(a)**), and SL1 has a quicker adsorption rate for MnO₂. When the nanoparticle influent passed through the soil bed, MnO₂ nanoparticles were quickly adsorbed on the soil and resulted in a retarded transport of the nanoparticles relative to water (**Figure 3-3(a)**); thus the adsorbed E2 was eluted by water before contacting with the nanoparticles, resulting in the observed lower degradation rate. In contrast, SL2 has a greater E2 sorption capacity and a slower desorption rate, and on the other hand, MnO₂ had a faster breakthrough with almost no retardation (**Figure 3-3(b)**), which allowed sufficient contact and reaction time to complete the degradation. The E2 sorption affinity is too high in SL3 to elute out, so the adsorbed E2 can hardly leach to groundwater.

Table 3-4. Degradation efficiency of CMC-MnO₂ treated columns.

Soil	M _{E2} ^a	v _p ^b	C ₀ ^c	C _{E2} ^d		S _{E2} ^e		T _{E2} ^f		Degradation of leachable E2 ^g
	mg	cm/min	g/L	%	%	%	%	%	%	%
				MnO ₂	control	MnO ₂	control	MnO ₂	control	MnO ₂
SL1	0.023	0.169	0.174	56	72	17	20	73	92	22
SL2	0.078	0.202	0.174	8	67	14	24	22	91	88
	0.078	0.808	0.174	24	59	21	28	45	87	59
	0.078	0.202	0.017	42	67	23	24	65	91	37
SL3	0.167	0.153	0.174	7	8	61	75	68	83	13

^a Initial loaded E2 mass in soil (extractable using hot methanol). ^b Pore velocity. ^c Injection MnO₂ concentration. ^d Elution E2 mass percentage compared to M_{E2}. ^e Extractable E2 mass percentage remaining in soil compared to M_{E2}. ^f Total detected E2 (elution add extractable) mass percentage compared to M_{E2}. ^g Degradation of leachable E2 = 1 - C_{E2} (CMC-MnO₂ treated)/ C_{E2}(control)

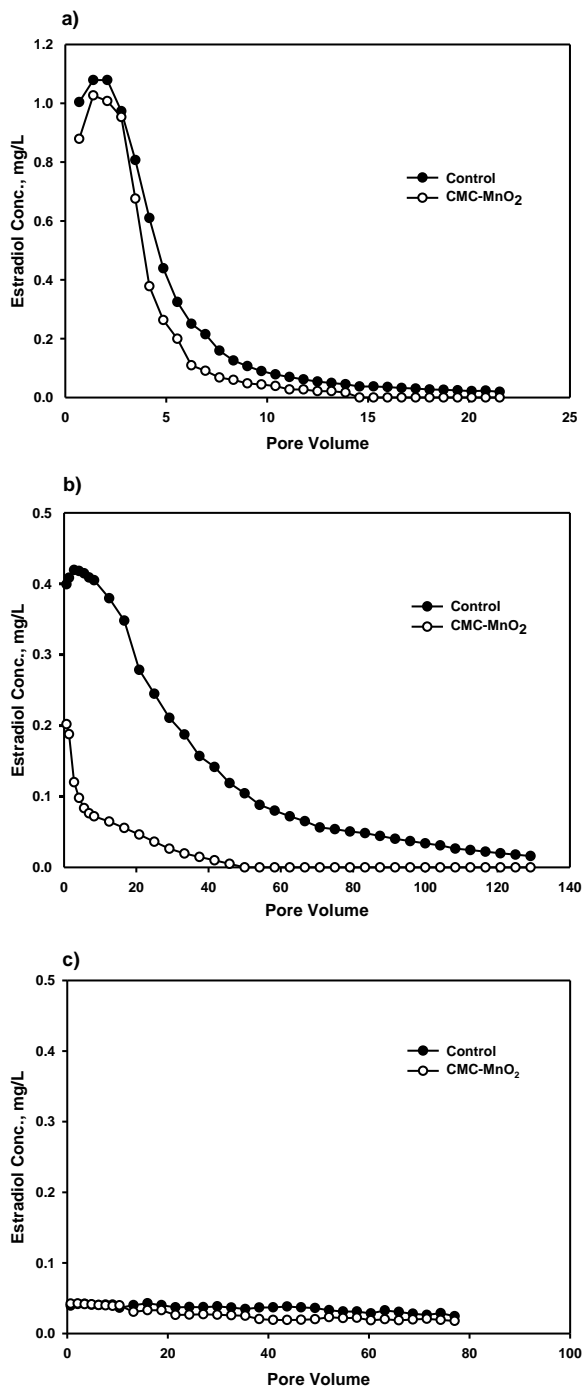


Figure 3-8. Elution histories of E2 from soils when subjected to a background CMC solution and a suspension of CMC-MnO₂ nanoparticles: (a) SL1 soil (E2 = 0.0019 mg-E2/g-soil), (b) SL2 soil (E2 = 0.0065 mg-E2/g-soil), and (c) SL3 soil (E2 = 0.0104 mg-E2/g-soil). Experiment conditions: MnO₂=0.174 g/L (2×10^{-3} M), CMC=250 mg/L, inlet flow rate=0.05 ml/min, soil =12 g.

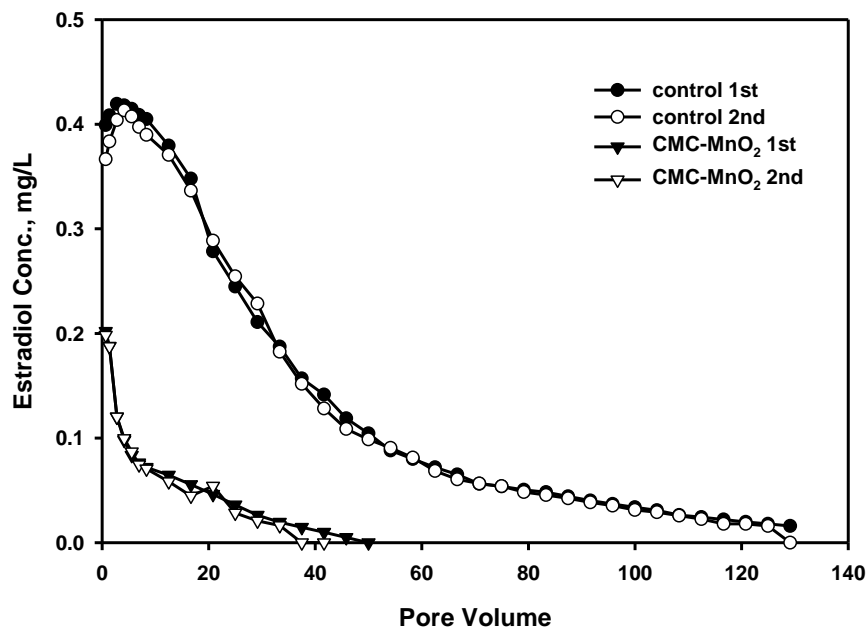


Figure 3-9. Duplicate of elution histories of E2 from SL2 soil when subjected to a background CMC solution and a suspension of CMC-MnO₂ nanoparticles. Experiment conditions: [E2] = 0.0019 mg-E2/g-soil, [MnO₂] = 0.174 g/L (2×10^{-3} M), [CMC] = 250 mg/L, inlet flow rate=0.05 ml/min, soil =12 g.

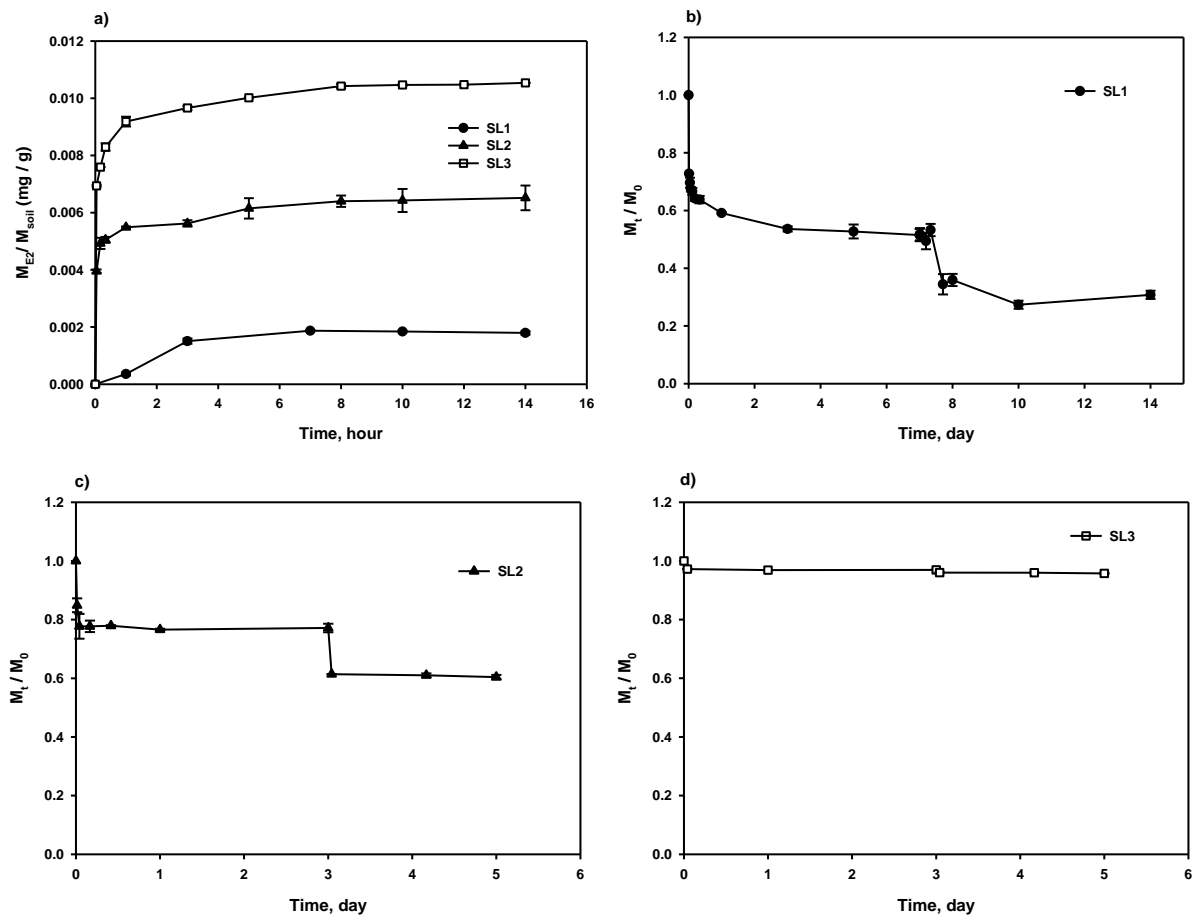


Figure 3-10. E2 (a) sorption kinetics with three soils (initial aqueous $[E2] = 4 \times 10^{-6} M$), and successive desorption kinetics in (b) SL1 soil, (c) SL2 soil, and (d) SL3 soils. In figure (b)-(d) M_t : E2 remaining in soil at time t ; M_0 : initial E2 in soil (0.0019 mg/g for SL1, 0.0065 mg/g for SL2, and 0.0104 mg/g for SL3).

3.3.6 Effect of flow velocity on degradation behavior

The effect of flow velocity on CMC-MnO₂ degradation was investigated for the SL2 soil. **Figure 3-11** shows the elution histories of E2 under different pore velocities of 0.202 and 0.808 cm/min for injection of nanoparticles and particle-free solution. **Figure 3-11** and **Table 3-4** show that when the injection velocity of nanoparticles was increased from 0.202 cm/min to 0.808 cm/min, the elution of E2 was increased from 8% of the initial loaded E2 to 24%. In the same way, E2 remaining in soil was increased from 14% to 21%. These results indicate a less degradation of both water-leachable and soil-sorbed E2 under higher injection velocity of nanoparticles.

Under injection of particle free solution (control), when the velocity was increased from 0.202 cm/min to 0.808 cm/min, the elution of E2 was first increased dramatically in initial 5 PVs and then decreased in the following 70 PVs, and the total elution was reduced slightly from 67% to 59%. It is noted that the nanoparticle treatment elution curves of two velocities showed significant discrepancy in the first 5 PVs, and the E2 elution was significant higher under the velocity of 0.808 cm/min. Comparing the control and MnO₂ elution curves indicate that the faster desorption of E2 in initial several PVs was one reason that caused the less degradation of E2 in high velocities. The MnO₂ nanoparticle transport behavior (**Figure 3-6**) showed a simultaneous breakthrough of the particles under the two velocities, and even a higher retention of the particle in lower velocities. Although the breakthrough occurred at the same pore volume, the empty bed contact time (BECT) of the particles is inversely proportional to velocities, which means the life-time of the particle in the column is three times longer at 0.202 cm/min than 0.808 cm/min. The faster MnO₂ transport rate at high velocity shortened the nanoparticles

from contacting with the contaminants, resulting in the observed lower degradation rate. In contrast, the nanoparticle transport was slower at a low velocity, which allowed sufficient contact and reaction time to degrade E2.

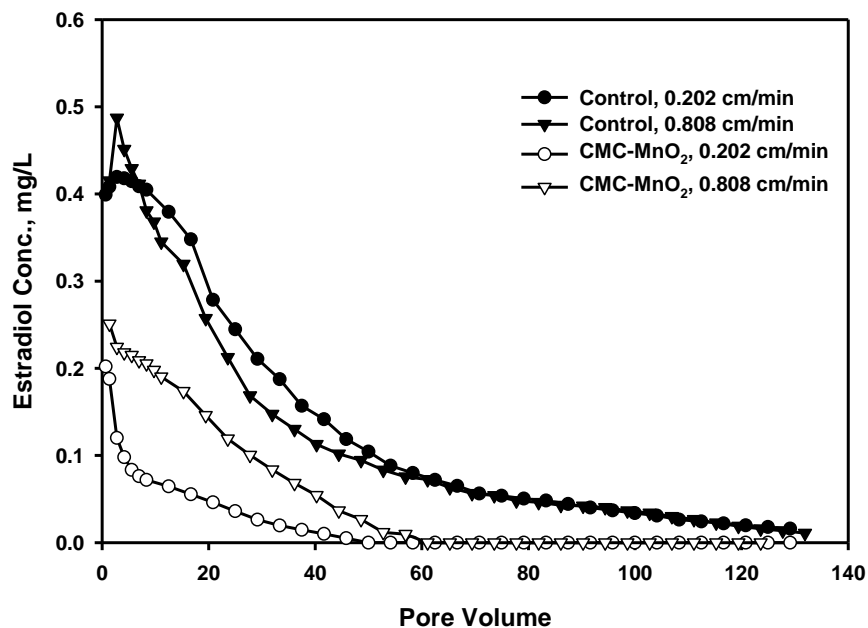


Figure 3-11. Elution histories of E2 from SL2 soil at different MnO₂ injection pore velocities. Experiment conditions: [E2] = 0.0019 mg-E2/g-soil, [MnO₂] = 0.174 g/L (2×10^{-3} M), [CMC] = 250 mg/L, soil = 12 g.

3.3.7 Effect of particle concentration on degradation behavior

Figure 3-12 shows the elution histories of E2 under different MnO₂ injection concentrations of 0.17 g/L and 0.017 g/L. When the injection MnO₂ concentration was decreased from 0.174 g/L to 0.017 g/L, the elution of E2 was increased significantly from 8% to 42%. Comparing to the control test, the degradation of leachable E2 was decreased from 88% to 37% when the injection particle concentration was reduced to one tenth (**Table 3-4**). After treatment with 0.017 g/L MnO₂ for 120 PVs, there is still 23% of initial E2 remaining in the soil, which showed almost no degradation for non-leachable E2 comparing to control test (24% remaining) (**Table 3-4**). The lower than anticipated degradation of E2 in the soil is probably due to the small amount of retention of CMC-MnO₂ by SL2 soil (**Table 3-3**). The high mobility and small amount of retention of CMC-MnO₂ in soil resulted in a difficult access of nanoparticles to soil immobilized E2. Han et al. (2015) reported several factors such as soil-MnO₂ interactions and soil-released metals and reductants could inhibit the oxidation effectiveness, so high dosage of MnO₂ is needed for effective field remediation of E2.

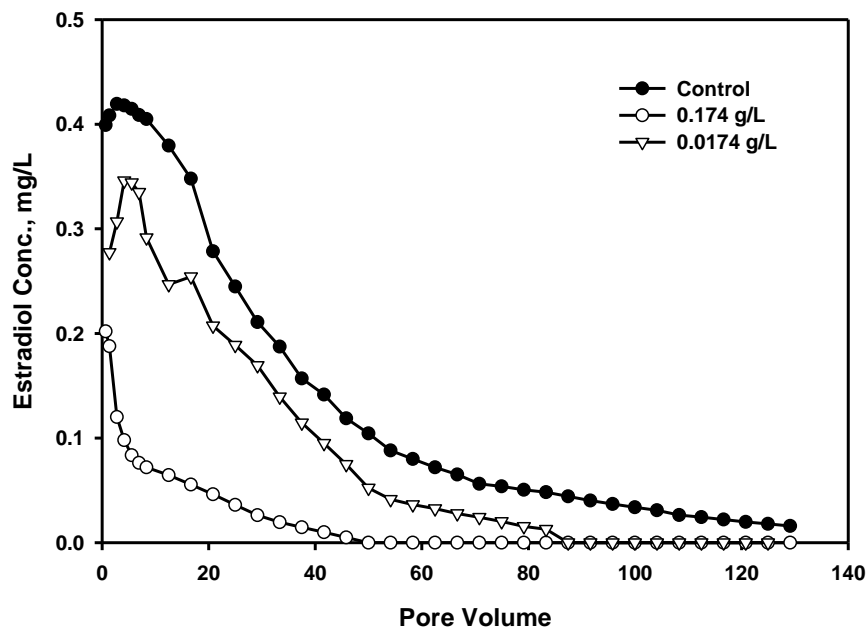


Figure 3-12. Elution histories of E2 from SL2 soil under different MnO₂ injection concentrations. Experiment conditions: [E2] = 0.0019 mg-E2/g-soil, inlet flow rate=0.05 ml/min, soil =12 g.

3.4. Conclusions

The direct injection of nanoparticles into contaminated aquifers has been suggested as a promising technology for in-situ remediation of contaminants. This work tested CMC-stabilized MnO₂ nanoparticles for in-situ oxidative degradation of soil-sorbed E2 in saturated aquifers. The CMC-stabilized MnO₂ nanoparticles exhibited high deliverability in natural soils; however, the mobility of the nanoparticles may be influenced by several factors concerning 1) nanoparticle surface chemistry, 2) soil surface chemistry and geochemical heterogeneities, and 3) groundwater hydrology. Well controlled column transport tests were conducted using three natural soils to address the transport behavior in porous media of varied complexities. Our results suggested MnO₂ deposition is much higher in soils that offer more favorable deposition sites than those that are unfavorable for deposition, which could be predicted based on the collector average surface potential. Surface charge heterogeneity which is related to the clay fraction is also a key factor controlling the deposition of nanoparticles onto soil surface.

The shape of the BTCs of the nanoparticles was determined by both the available favorable solid surface area and the mass transfer rate of the nanoparticles to the favorable sites. The former influences the fully breakthrough concentration level (C/C_0) and the latter influences the breakthrough time. The BTCs were successfully simulated using an advection-dispersion equation that accounted for irreversible deposition and blocking. Results showed that the S_{max}^* values reflected the available favorable deposition sites on the solid surface, and k_{dep} values reflected the mass transfer rate of the nanoparticles to deposition sites, which are two parameters predicting the nanoparticle deposition rate. The S_{max}^* and k_{dep} values are both increasing with

decreasing flow velocity. The results indicate the transport of the NPs can be controlled by manipulating the injection pressure or pore velocity. Under natural groundwater conditions, the delivered CMC-MnO₂ nanoparticles will remain in a confined domain facilitating in-situ oxidation of the contaminants.

This study first simulates the in-situ degradation of soil-sorbed E2 through column tests, and provides insights into MnO₂ nanoparticle degradation behavior in real natural conditions. Results showed the degradation efficiency of the nanoparticles may be influenced by several factors, such as soil properties, particle injection velocity, and particle injection concentration. The combination of these factors affects the nanoparticle degradation behavior in one key aspect, i.e., the contact time of the nanoparticles with the contaminants. The nanoparticles are more effective for soils of moderate or high organic contents that offer slow E2 desorption rate and a less delayed MnO₂ breakthrough which allow sufficient contact and reaction time to complete the degradation. For the same soil, reducing injection velocity could increase particle and contaminant contact time, but on the other aspect, reducing velocity could also increase nanoparticle retention by soil. Therefore, choosing an optimal nanoparticle injection velocity is important. Compared to water treatment, high dosage of MnO₂ is needed to effective degradation of soil-sorbed E2. This study provides a frame work for lab test of in-situ degradation of soil-sorbed contaminants using nanoparticle treatment, and confirmed this in-situ remediation technology may provide a powerful strategy to degrade E2 and other endocrine disruptors in soil and groundwater.

CHAPTER 4. CATALYTIC HYDRODECHLORINATION OF TRICLOSAN WITH ANION-EXCHANGE-RESIN SUPPORTED PALLADIUM

4.1 Introduction

Triclosan (5-chloro-2-(2,4-dichlorophenoxy)phenol, TCS) is a broad-spectrum antimicrobial used worldwide, as a preservative or an antiseptic agent in many personal care (e.g., toothpaste, soaps, deodorants, shampoos, and cosmetics) and household (e.g., plastic additives) products. Being a pharmaceutical and personal care product (PPCP) ingredient, substantial amounts of TCS are discharged into wastewater treatment plants (WWTPs). Studies on the fate of TCS during wastewater treatment indicated that TCS can be removed by wastewater treatment plant with a high efficiency of 80%-96% (Bester, 2003; Winkler et al., 2007). However, residues of TCS are still detected in effluents, leading to discharge in surface water. The U.S. Geological Survey reported that TCS was among the seven most frequently detected organic contaminants in 139 streams sampled across 30 states with the median concentration of 0.14 $\mu\text{g/L}$ (Kolpin et al., 2002). In addition, the TCS removed by activated sludge was not degraded by biomass, the antimicrobials distributed themselves into carbon- and lipid-rich sewage sludge, and accumulated in the biosolids (Heidler and Halden, 2007; Winkler et al., 2007).

There is growing concerns raised over TCS's persistence in the environment and its potential risk to aquatic lives and humans. TCS is concerned as an endocrine disrupting chemical and reported to have adverse effects on thyroid hormone homeostasis (Veldhoen et al., 2006). Moreover, TCS, which was found to accumulate in various

aquatic organisms, is highly toxic to certain types of algae and fish (Ishibashi et al., 2004; Orvos et al., 2002). Orvos et al. (2002) reported that 96 h median lethal concentration values of TCS for *Pimephales promelas* and *Lepomis macrochirus* were 260 and 370 µg/L, respectively. As an antibiotic, TCS may induce the bacterial resistance development (McMurry et al., 1998). Of particular concern is sewage sludge, where an abundance of pathogens and multiple antibiotics coexist, and thus creating a large risk of drug resistance for the pathogens (Halden, 2014). In addition, TCS may form highly toxic chlorodioxins during incineration or under sunlight (Kanetoshi et al., 1987; 1988).

Various oxidation treatment processes were applied to degrade TCS in drinking water and wastewater plants including chlorine oxidation, ozonation, and sunlight or UV irradiation. However, these technologies produce more toxic byproducts (Inaba et al., 2006; Klammer et al., 2010; Latch et al., 2005; Rule et al., 2005). Therefore, other techniques are needed to investigate to decrease the toxicity of TCS.

Hydrodechlorination (HDC) is a method of reductive degradation of chlorinated organic compounds by hydrogen gas with release of inorganic chloride ions. Catalytic HDC appears as an attractive technology for its complete destruction and elimination of the toxicity of the chlorinated aliphatic and aromatic compounds with minimum activation energy requirement (Janiak and Okal, 2009; Pizarro et al., 2014; Srebowata et al., 2014; Zhang et al., 2013; Zhou et al., 2013). For instance, Schuth and Reinhard (1998) demonstrated that an alumina supported palladium (Pd) was able to catalytic HDC of aromatic compounds. They reported chlorinated benzenes and lindane were completely hydrodechlorinated to benzene, and biphenyl and polycyclic aromatic hydrocarbons (PAHs) were partially or completely hydrogenated to cleave the double bond of benzene

ring. One of the most frequently used catalysts in catalytic HDC was Pd for its high efficiency in catalysis and its activity under ambient pressure and temperature. The mechanism of Pd in HDC is considered to facilitate C-Cl bond cleavage and formation of highly reactive atomic hydrogen (Chen et al., 2002; Lowry and Reinhard 2001).

To enhance metal dispersion and achieve recycle use of catalysts, Pd is often loaded on supports. Among various support materials, the most common ones are activated carbon (AC) and alumina (Al_2O_3) (Chaplin et al., 2012; Diaz et al., 2011; Zhang et al., 2013). In spite of many advantages of catalytic HDC, in many cases the catalysts suffered from loss of catalytic activity. The deactivation of Pd catalysts on supporting materials is commonly due to Pd leaching, chloride poisoning, sintering, or accumulation of products on the catalyst surface (Concibido et al., 2007; Diaz et al., 2011; Janiak and Okal, 2009; Yuan and Keane, 2003; 2004). Conventionally, Pd particles are prepared in the ionic form in solution and then loaded on a support via the incipient wetness impregnation method. However, due to the lack of specific interactions between Pd and the supporting materials, the loaded Pd catalysts are prone to leach, leading to loss of catalytic activity. For instance, Yuan and Keane (2004) tested carbon and alumina supported Pd activity in HDC of dichlorophenol, and observed a 34% of Pd leaching with carbon support compared to 10% with alumina support, and suggested a stronger metal support interactions between Pd and alumina. To enhance Pd interaction with supporting material further to reduce Pd leaching, Gasparovicova et al. (2006) prepared a Pd-Cu catalyst supported on strong cationic resins to reduce nitrates, and found undetectable of Pd leaching from the supports. They observed a better selectivity to N_2 production with

resin-supported catalyst, but lower activity than those obtained with inorganic supports (Al_2O_3).

Compare to conventional supports such as alumina and AC, functional polymers may offer some advantages when used for preparing supported catalysts. First, the polymer resin may form strong specific interaction with Pd through chemical binding (ionic bounds) or physical size exclusion (porosity), and therefore reduce Pd leaching from the support. Second, the chemical interaction between resin and Pd allows a different loading method (e.g., ion-exchange and then reduce under normal temperature) from the incipient wetness impregnation approach. This method may eliminate calcination and thereby save energy and reduce cost. Moreover, there have been diverse types of ion exchange resins available on the market with a wide range of physical-chemical characteristics (functionality, porosity, matrix hydrophobicity, and surface area), which allow researchers to choose different resins for different purpose.

In this study, a new class of Pd catalysts supported on two strong basic anion (SBA) exchange resins Amberlite IRA-900 and Amberlite IRA-958 were prepared by ion-exchange and subsequent reduction method, and the liquid phase catalytic HDC of TCS on the catalysts was investigated. The specific objectives of this study were to: 1) Prepare and characterize of the resin-supported Pd catalysts; 2) Determine the effects of Pd loading, type of resin matrix, and dissolved organic matter (DOM) on the effectiveness of HDC of TCS; and 3) Identify the reaction pathway of catalytic HDC of TCS. To the best of our knowledge, this has been the first study on degradation of TCS using a reduction method.

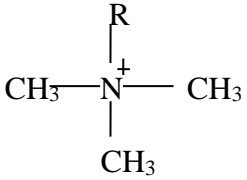
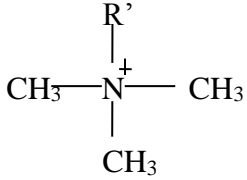
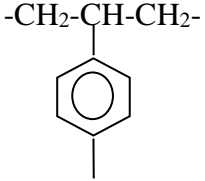
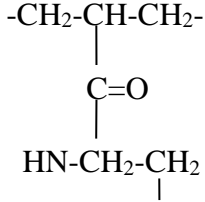
4.2. Materials and methods

4.2.1 Materials

The following chemicals of analytical or higher grade were used: triclosan (5-chloro-2-(2,4-dichlorophenoxy)phenol, $C_{12}H_7Cl_3O_2$, purity >99%, Alfa Aesar, Ward Hill, MA, USA), sodium tetrachloropalladate (II) trihydrate ($Na_2PdCl_4 \cdot 3H_2O$, 99%, Strem Chemicals, Newburyport, MA, USA), sodium borohydride ($NaBH_4$, ICN Biomedicals, Aurora, OH, USA), dichloromethane (CH_2Cl_2 , Honeywell, Muskegon, MI, USA), and Fluka humic acid No. 53680 (Sigma-Aldrich, St. Louis, MO, USA). Methanol (CH_4O , Alfa Aesar) and acetonitrile (CH_3CN , EMD Millipore, Billerica, MA, USA) were of HPLC grade (>99% purity). A stock solution of triclosan was prepared at 0.01 M in methanol. All other solutions were prepared using deionized (DI) water (18.2 M Ω -cm).

Two ion exchange resins, Amberlite IRA-900 and IRA-958 (both are in Cl^- form) (Rohm & Haas, Philadelphia, PA, USA) were purchased from Sigma-Aldrich. Both resins are macroporous SBA exchange resins, possessing identical functional group and ion exchange capacity, but different in the polymer matrix. **Table 4-1** lists the salient properties of the two resins. Before use, the resins were conditioned following procedure of cyclic exhaustion with 1 N sodium hydroxide, 1 N hydrochloric acid, 1 N NaCl, rinsing successively with DI water, and then air-dried (Xiong et al., 2007).

Table 4-1. Salient properties of ion exchange resins used in this study.

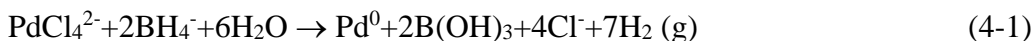
Sorbent	IRA 900	IRA 958
Description	SBA resin	SBA resin
Functional Group		
Matrix	 Polystyrene, macroporous	 Polyacrylic, macroporous
Bead size (mm)	0.65-0.82	0.63-0.85
IE Capacity (meq/g)	3.1 ^a	2.2 ^a
Water Content (%)	58-64	66-72
BET Surface Area (m ² /g)	22 ^b	2.03 ^c
Average pore diameter (nm)	37.2 ^d	6.46 ^e
Operating temperature (°C)	< 60	< 80

* All data obtained from Rohm and Haas Technical Bulletins unless specified otherwise;

^a From this work, determined by ion-exchange of Cl⁻ with SO₄²⁻. ^b From Delgado et al (2007). ^c From Kolodynska (2010). ^d From Schouten et al. (2007). ^e From Greluk and Hubicki (2010).

4.2.2 Catalyst preparation

The resin-supported Pd catalysts were prepared by a two-step process of ion-exchange and subsequent reduction. In brief, an anionic form of Pd ($[\text{PdCl}_4]^{2-}$) was first absorbed on the resins through ion-exchange process via batch tests. Typically, to prepare 2.0 wt.% Pd loading catalysts, a solution containing of 21.5 mg/L of Pd and 1 g/L NaCl was mixed with the resins with a solution-to-resin ratio of 1 (L):1 (g) until reach ion-exchange equilibrium (shaking mixture at 150 rpm for 72 h). The addition of NaCl is to maintain the Pd in the anionic form (form ligands with Cl⁻). Then the supernatant was decanted and a 0.86 g/L of borohydride solution (3 times of stoichiometric amount of Pd) was added in the Pd-adsorbed resins dropwise with a solution-to-resin ratio of 50 (mL):1 (g). After reaction (150 rpm shaking) for 20 min, the PdCl_4^{2-} on the ion exchange resins was reduced to Pd⁰ via reaction



The resin-supported Pd catalysts (i.e., Pd/IRA-900 and Pd/IRA-958) were washed with 100 mL of DI water three times to remove residual borohydride and air dried for 12 h before being used for TCS HDC. Pd loading on the resins was calculated based on the Pd contents in aqueous solution before and after ion exchange, and Pd concentration in solution was analyzed using an Inductive Coupled Plasma–Optical Emission Spectrometer (Varian ICP 710-ES, Varian Inc., Walnut Creek, CA) with a detection limit of ~0.03 mg/L.

4.2.3 Catalyst characterization

The topography of the resin-supported Pd catalysts was investigated by scanning electron microscopy (SEM, JSM-7000F, JEOL, USA) coupled with an energy-dispersive

X-ray spectroscopy (EDXS, INCA x-sight, Oxford Instruments) for elemental composition analysis. The supported Pd catalysts were first vacuum dried at room temperature for 5 days, then coated with a thin layer of gold before SEM analysis. To explore the Pd internal distribution in resins and the morphology of the internal resins, the Pd loaded resins were bisected and analyzed in selected cases using SEM and EDXS. The powder X-ray diffraction (XRD) patterns of catalysts were obtained with a Bruker D2 PHASER powder diffractometer (Bruker AXS, Germany) using Cu $K\alpha$ radiation ($\lambda = 1.5418 \text{ \AA}$) at a scan rate (2θ) of $4^\circ/\text{min}$. The XRD analyses were performed on the resin only (i.e., IRA-900 and IRA-958) and resin catalysts (i.e., Pd/IRA-900 and Pd/IRA-958) before and after 8 reaction cycles of HDC.

4.2.4 Catalytic hydrodechlorination of TCS

Duplicate batch experiments were conducted to test the effectiveness of the supported Pd catalysts for HDC of TCS in the aqueous phase. First, 0.1 g of resin-supported Pd catalysts were mixed with 100 mL of DI water in a 127 mL amber serum bottle. Then the mixtures were purged with hydrogen gas for 25 min to obtain a H_2 -saturated solution (H_2 solubility $\approx 1.6 \text{ mg/L}$ at 20°C) and H_2 -filled headspace of the reactor ($\sim 27 \text{ mL}$). Upon saturation, the bottle was quickly capped with an open-top screw cap equipped with PTFE-lined septa. The HDC of TCS was then initiated by injecting of $100 \text{ }\mu\text{L}$ of TCS stock solution to yield an initial TCS concentration of $10 \text{ }\mu\text{M}$ (2.9 mg/L). The reactor was then flat mounted to a shaker and mixed at 150 rpm at room temperature to achieve a homogeneous mixture. At selected times, 0.5 mL of the solution was withdrawn into a 2 mL of HPLC amber vial using a syringe. The TCS concentration was analyzed with an HP Agilent 1260 Infinity HPLC system equipped with a Poroshell 120

EC-C18 column (4.6×50mm, 2.7 μm) and a UV detector. The analysis of TCS was followed Zhang and Huang's method (Zhang and Huang, 2003) with a detection limit of 2.5×10^{-8} M. To avoid TCS adsorption on resins, duplicate control tests were conducted without both Pd and resins and under the same hydrogen conditions.

Because of the hydrophobicity of the resins, TCS loss in aqueous phase may due to degradation or adsorption. To quantify TCS adsorbed on resins, ~99 mL of aqueous supernatant was withdrawn at predetermined times and replaced with 30 mL of methanol. After release of hydrogen gas, the HDC process was terminated, and the TCS adsorbed on resin-supported catalysts were extracted using methanol by shaking at 250 rpm for 24 h. After extraction, 0.5 mL of the extract was transferred into a HPLC vial containing 0.5 mL of DI water for HPLC analysis. The extraction efficiency using this method was determined to be 96 ± 3 %, and 97 ± 2 % for IRA-900, and IRA-958, respectively.

4.2.5 Catalyst lifetime

The lifetime and reusability of the resin-supported catalysts were tested in the batch experiments with the same catalysts were repeatedly used in 8 consecutive cycles without any treatment. Each cycle of the batch test was carried out in the same manner as mentioned above. After saturation with hydrogen gas, a new reaction cycle was initiated by injection the same volume of TCS stock solution. In each cycle, a total volume of 2.5 mL of aqueous phase was withdrawn (each sample time 0.5 mL was withdrawn) to monitor TCS degradation until TCS was undetectable ($< 2.5 \times 10^{-8}$ M). After each cycle, 2.5 mL of DI water was added into the duplicate bottles to maintain a total volume of 100 mL. To analyze the Pd bleeding during HDC, aqueous samples were acidified and analyzed for total Pd after the last reaction cycle.

4.2.6 Analysis of hydrodechlorination byproducts

To determine the HDC byproducts of TCS, sacrificed batch tests were conducted under the identical experiment condition with HDC of TCS. At selected times, 100 mL of the reaction suspensions containing the organic reactant and resin-supported Pd catalysts were extracted by vigorous shaking with 20 mL of dichloromethane (MeCl_2) for 10 min. The extract was then dehydrated with anhydrous sodium sulfate and then filtered through a 0.22 μM PTFE syringe filter. Controls with only TCS and Pd loaded resins but without hydrogen gas purge were also extracted in the same way and only TCS was detected, yielding an extraction efficiency > 90%. The HDC byproducts were analyzed by a Gas Chromatography/Mass Spectrometry (GC/MS) HP7890A/HP5975C system (Agilent Technologies Inc., Santa Clara, CA) with a HP-5MS column (30 m \times 0.25 mm \times 0.25 μm). The GC/MS conditions were programmed as follows: splitless injection at 280 $^\circ\text{C}$ and oven temperature raised from 70 $^\circ\text{C}$ to 280 $^\circ\text{C}$ at 6 $^\circ\text{C}/\text{min}$ following by a 10 min holding at 280 $^\circ\text{C}$. Helium was used as the carrier gas at a flow rate of 1.2 mL/min. Electron ionization (EI) with the mass scan range from 35 to 550 m/z and temperature of MS source of 250 $^\circ\text{C}$ was conducted.

4.2.7 Analysis of Cl balance

To check the total chlorine balance in the system, chloride ion production in the process of HDC was analyzed. Because the reaction pathway is the same for the two type of resins, thus, this test was only conducted with the IRA-958 supported Pd catalysts. In order to avoid Cl^- adsorption on the anion exchange resins or release from the chloride form resins, after loading with Pd (i.e., just before HDC test) the resins were pretreated to replace Cl^- with SO_4^{2-} in a column run using 5 mM SO_4^{2-} to exchange the Cl^- (also use

this method to determine the ion exchange (IE) capacity of the resins). Until no Cl^- was detected in the outflow, the resins were completely saturated with SO_4^{2-} . Then the pretreated Pd/IRA-958 catalysts were used for HDC test. Here the HDC were carried out in batch sacrifice tests. At predetermined times, duplicate of bottles were terminated reaction, and supernatant was withdrawn to analyze TCS and Cl^- concentration in the aqueous phase. After completely removing the supernatant, the resins were added in 100 mL of 5 mM SO_4^{2-} solution, then the mixture was allowed to shake for 1 day to completely exchange with Cl^- adsorbed on the resins in the HDC process. The supernatant was sampled to analyze Cl^- . After the supernatant was replaced by another 100 mL of SO_4^{2-} solution, the exchange process was repeated again until no Cl^- was detected in the supernatant. At the end of experiment, the total chlorine in the system at each time point was the sum of chlorine in TCS, chloride ion in aqueous solution, and chloride ion adsorbed on resins. The chloride ion concentration in solution was analyzed using a Dionex Ion Chromatograph (DX-120, Dionex, Sunnyvale, CA) with a detection limit <0.05 mg/L.

4.3. Results and discussion

4.3.1 Catalysts characterization

The XRD patterns of either resins only (i.e., IRA-900, IRA-958) or resin-supported Pd catalysts (i.e., Pd/IRA-900 and Pd/IRA-958) before and after eight reaction cycles of HDC were analyzed, and the results are shown in **Figure 4-1**. No peaks were detected in the diffractogram of the two types of resins, and three peaks were observed in the XRD pattern at 2θ around 40° , 46° , and 68° of Pd loaded resins. These peaks are assigned to the 111, 200 and 220 planes of the face centered cubic (fcc) crystallographic

structure of Pd, respectively (JCPDS No. 05-0681). Comparing the freshly prepared Pd catalysts with the catalysts after eight consecutive HDC cycles, there is no change or shift of the Pd peaks of the XRD analysis, which indicate the catalysts composition and crystallographic structure did not change in the reaction.

The dry state morphology of the cross-section of investigated resins is illustrated in **Figure 4-2** at low (**Figure 4-2(a)-(b)**) and high (**Figure 4-2(c)-(d)**) magnification. The high magnification SEM images show a macroreticular internal structure of the resins, and the macropores (pore diameter larger than 50 nm) result from “glueing” of a mass of polymer nodules. It is noted that the porosity is higher for IRA-900 which contains much more mesopores between the nodules while the nodules are more glued for IRA-958. Consistent with the SEM images, the BET surface area of the IRA-900 (22 m²/g) (Delgado et al., 2007) is much higher than IRA-958 (2.03 m²/g) (Kolodynska, 2010). The dry state BET surface area of the resins is small compared to inorganic supports (e.g., 92 m²/g for Al₂O₃ and 1011 m²/g for AC) (Diaz et al., 2011; Zhang et al., 2013). However, it was suggested that the BET surface area has little relevance to the actual performance of the polymer-supported catalyst due to the swelling phenomenon of the resins under aqueous phase conditions (Biffis et al., 2000; D'Archivio et al., 2000).

Radial distribution of Pd at the cross-section of the resins was analyzed by EDXS via 11 point scan, where the 11 points were distributed along the radius in upper and right direction (points position were shown in **Figure 4-2(a)-(b)**), and the EDXS results are shown in **Figure 4-3**. The EDXS analysis gave the Pd atomic percentage relative to other elements, and based on the hypothesis that the Cl⁻ was evenly distributed in the whole resins (the resins are in Cl⁻ form and saturated with Cl⁻), Pd distribution was plotted as Pd

to Cl percentage. From the results we can see the Pd distribution was symmetric along the distance from the center of the sphere, and the Pd was almost homogeneously distributed in the resins, with only a little higher at the surface (5% and 10% for IRA-900, and IRA-958, respectively) than inner part of the resins. Similar observations were reported by Zecca et al. (1998) and Biffis et al. (2000). The macroreticular structure of the resins and the long time adsorption equilibrium (3 days) may contribute to the homogeneous dispersion of Pd. The total concentration of Cl^- in the resins (i.e., ion exchange capacity) was determined to be 3.14 meq/g and 2.21 meq/g for IRA-900 and IRA-958, respectively, through ion-exchange of Cl^- with SO_4^{2-} . Interior of the resin IRA-900 and IRA-958, the average Pd to Cl atomic ratio is 7% and 9%, which is a 23 and 22 milligram Pd loading per gram of resins, respectively. This result is reasonable compared with the 2.0 wt.% Pd loading mass.

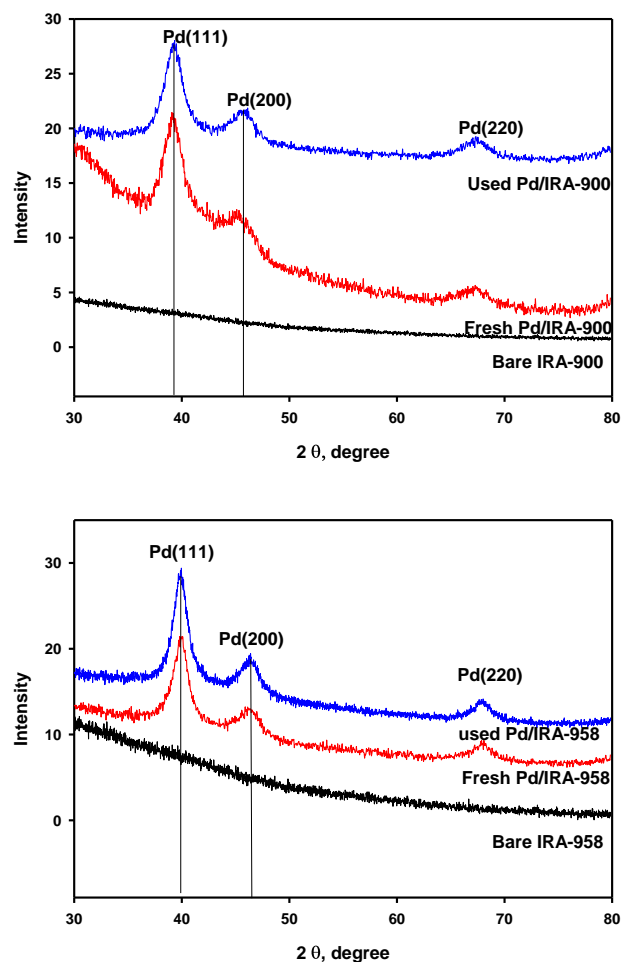


Figure 4-1. XRD patterns of bare resins, freshly prepared resin-supported Pd catalysts, and used catalysts after 8 consecutive runs of HDC of TCS. Bragg angles (2θ) from 30° to 80° were scanned at a scan rate of $4^\circ/\text{min}$. Pd loading is 2.0 wt.% of resins.

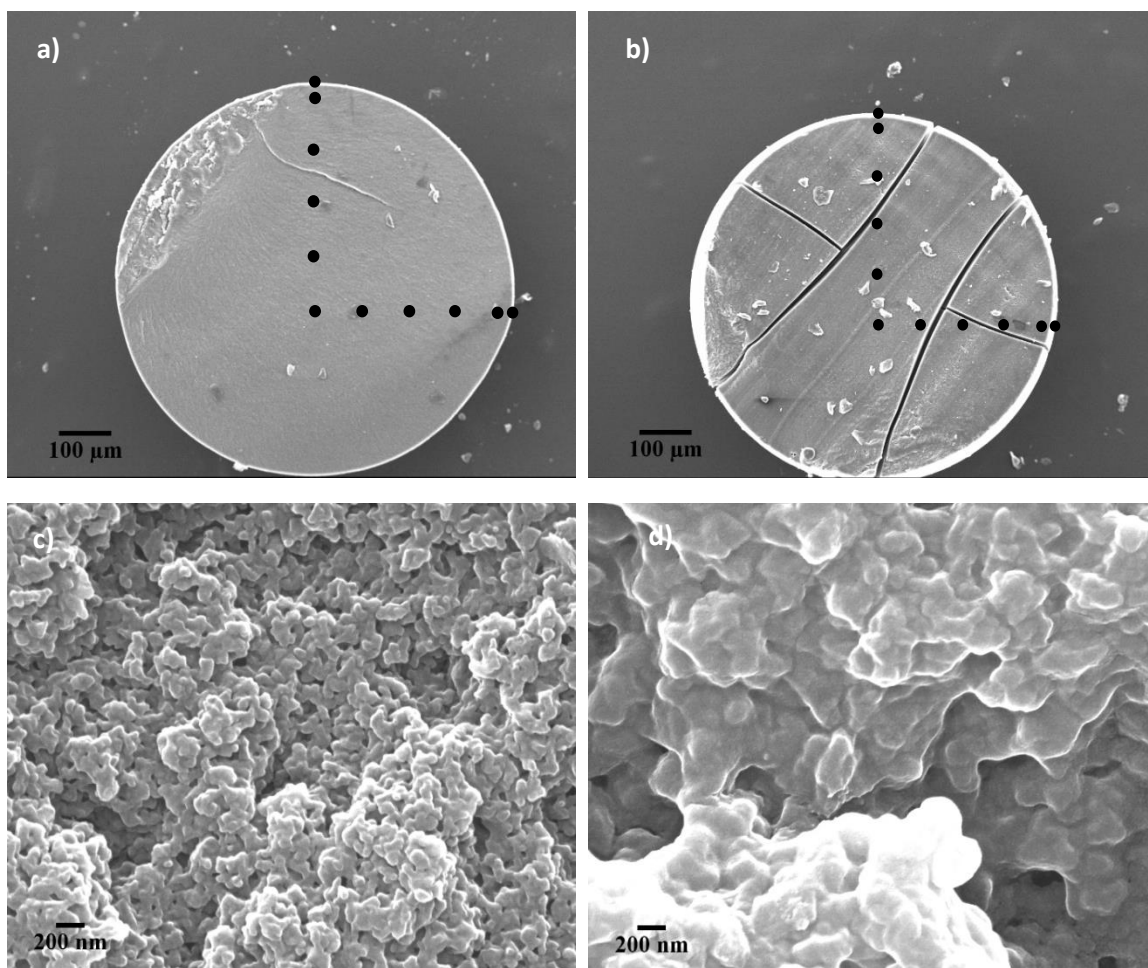


Figure 4-2. SEM images of resin-supported Pd catalysts: cross-section of (a) IRA-900 and (b) IRA-958 at low magnification, and internal of (c) IRA-900 and (d) IRA-958 at high magnification. Pd loading is 2 wt.% of resins. The points in (a) and (b) are EDXS scanning positions.

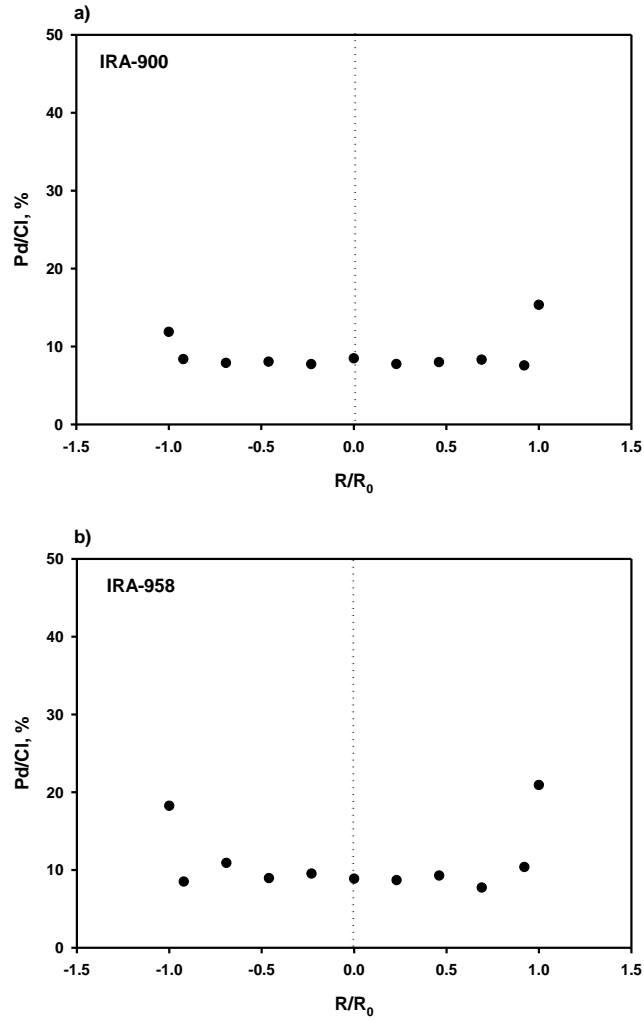


Figure 4-3. Radial distribution of Pd at the cross-section of the (a) IRA-900 and (b) IRA-958 analyzed by EDXS. The $R/R_0 > 0$ and $R/R_0 < 0$ scanning positions are along the radius in right and upper direction shown in Figure 4-2. Pd distribution is plotted as Pd to Cl atomic percentage.

4.3.2 Effect of Pd loading on the rate of hydrodechlorination reaction

Batch kinetic tests of HDC of TCS were carried out under different Pd loadings. **Figure 4-4(a)-(b)** compares the catalytic activity of the two resins with different Pd loadings. In both cases, the total mass of resins was kept identical as 1 g/L. Control tests were conducted without resin-supported Pd, and the result indicates without catalyst H₂ gas can reduce 7% of TCS in 2 hours. **Figure 4-4(c)-(d)** plots the kinetic data according to the linearized pseudo first-order rate equation as follows (Lowry and Reinhard, 1999):

$$-\frac{dC_{\text{TCS}}}{dt} = k_{\text{app}}C_{\text{TCS}} \quad (4-2)$$

$$k_{\text{app}}C_{\text{TCS}} = k_{\text{obs}}C_{\text{Pd}}C_{\text{TCS}} \quad (4-3)$$

Where C_{TCS} (mg/L) is the aqueous phase concentration of TCS, k_{app} (min⁻¹) is the apparent rate constant. Eqn. 4-2 represents the pseudo first-order rate degradation of TCS. k_{obs} (L/g/min) is the observed rate constant normalized to Pd catalyst concentration (C_{Pd} (g/L)), so in Eqn. 4-3, the apparent rate constant is given as a product of observed rate constant k_{obs} times Pd concentration C_{Pd} .

The pseudo first-order rate constants are provided in **Table 4-2**. For Pd/IRA-900, when increasing the Pd loading from 0.2 wt.% to 17.6 wt.%, the apparent rate constant was kept identical approximate to 0.026±0.004 min⁻¹. Based on the fact that without Pd loading (0 wt.% Pd) the TCS concentration in aqueous phase was still reduced quickly with the apparent constant rate of 0.021±0.001 min⁻¹, the TCS loss in aqueous phase could be attributed to adsorption of TCS on the resins. Therefore, as long as TCS adsorption rate was comparable to reaction rate, increasing of Pd loading would not change the reduction rate of TCS in aqueous phase. In contrast, for IRA-958, when the Pd loading increased from 0.2 wt.% to 11.2 wt.%, the apparent constant rate increased from

0.024±0.003 min⁻¹ to 0.037±0.004 min⁻¹. At 0 wt.% Pd loading, the aqueous phase TCS was slightly decreased by 20%, indicating a weaker adsorption of TCS on IRA-958 than IRA-900. This observation corroborates that the resin matrix, i.e., matrix hydrophobicity, contributes to the adsorption of the organic compounds. Between polystyrene (IRA-900) and polyacrylic (IRA-958) matrices, the latter one is less hydrophobic due to the open-chain aliphatic structure containing carbonyl groups. Thus, the hydrophobic TCS ($\log K_{OC}$ is 3.8-4.0) (Lindstrom et al., 2002) is more easily adsorbed on IRA-900 through π - π reaction. The observed rate constants k_{obs} all decreased with an increase of Pd loading for both type of resins, so use of low concentration of Pd has higher efficiency from both cost and reaction rate aspects.

For Pd/IRA-958, the apparent first order rate constant (k_{app}) was estimated to be 0.024±0.003 min⁻¹, 0.031±0.002 min⁻¹, 0.033±0.001 min⁻¹, 0.037±0.001 min⁻¹, and 0.037±0.004 min⁻¹ containing 0.2 wt.%, 2.0 wt.%, 4.9 wt.%, 7.8 wt.%, and 11.2 wt.% Pd, respectively. At a loading level below 7.8 wt.%, the catalytic activity on HDC of TCS increased with the Pd loading, while a further increase in Pd loading could not enhance the reaction rate any more. The observation suggests that the higher Pd loadings, the greater of the catalysts activity, until a peak Pd loading is reached. Similar results were observed by other researchers. Nutt et al. (2005) studied effect of Pd loading on TCE degradation rate with a Pd-on-Au bimetallic catalyst, and found formation of multiple layers of Pd particles at the support surface at elevated Pd loadings. The multiple surface Pd layers may block the accessibility of the interior Pd sites of a porous support, which resulted in a decrease in the specific surface area and the overall catalytic activity at extremely high metal loadings. Zhou et al. (2013) determined that the optimal Pd loading

for HDC of chloroacetic acids over Pd/ZrO₂ catalysts was 1.74 wt.%, and they attributed the catalytic activity decrease to Pd particle size increase with elevation of Pd loadings. They found Pd particle size was increased with Pd loading and suggested that the increase of size resulted from aggregation of Pd particles on ZrO₂ surface. As a result, the catalyst surface area was not increased anymore with increasing of Pd loading.

Yuan and Keane (2004) reported an observed rate constant k_{obs} of 6.78 L/min/g and 7.20 L/min/g for HDC of 2,4 chlorophenol catalyzed by 1.0 wt.% Pd supported on alumina and AC, respectively. In our case, at 0.2 wt.% and 2.0 wt.% Pd loading, the k_{obs} was determined to be 12 ± 2 L/min/g and 1.6 ± 0.1 L/min/g, respectively. With increasing Cl substitution, the HDC rate was reported to decrease (Chaplin et al., 2012). As a result, the resin-supported Pd catalysts have relative high catalytic activity toward HDC of TCS.

Table 4-2. Reaction rate constants for HDC of TCS catalyzed by resin-supported Pd

Support	Pd content (wt.%)	k_{app}, min^{-1}	$k_{obs}, \text{L/g/min}$	R^2
IRA-900	0	0.021±0.001		0.995
	0.2	0.026±0.002	13±1	1.000
	2.0	0.025±0.001	1.25±0.06	0.999
	4.9	0.026±0.002	0.53±0.04	0.998
	10.8	0.028±0.002	0.26±0.02	0.999
	17.6	0.027±0.003	0.15±0.02	0.999
IRA-958	0	0.002±0.000		0.702
	0.2	0.024±0.003	12±2	0.998
	2.0	0.031±0.002	1.6±0.1	1.000
	4.9	0.033±0.001	0.67±0.02	0.999
	7.8	0.037±0.001	0.46±0.01	1.000
	11.2	0.037±0.004	0.31±0.03	0.999

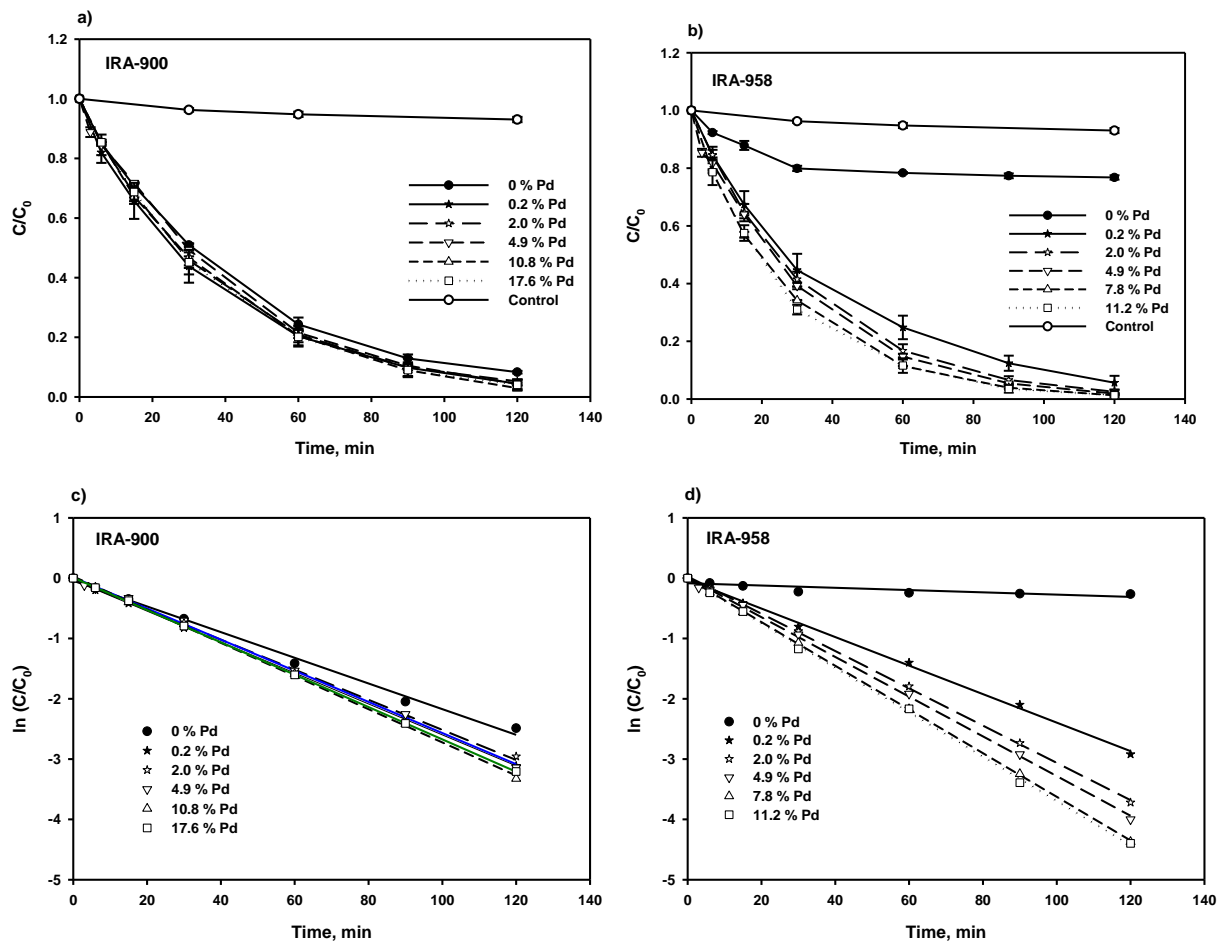


Figure 4-4. Kinetic profiles of catalytic HDC of TCS with different Pd loadings on resin (a) IRA-900 and (b) IRA-958, and linearized pseudo first-order plot for (c) IRA-900 and (d) IRA-958. Initial [TCS] = 2.9 mg/L, resin = 1 g/L.

4.3.3 Effect of support on the rate of TCS adsorption and reaction

For a heterogeneous catalytic reaction, reactant adsorption to catalyst surface is a prerequisite step, and the catalytic reaction rate is reported to relate to the adsorption rate of the reactant (Andersin and Honkala, 2011; Zhou et al., 2013). To quantify the TCS loss in aqueous phase due to adsorption instead of reaction, methanol was used to extract TCS from resins in each reaction point, and TCS remaining in the aqueous phase and resin phase was separately plotted in **Figure 4-5**.

Figure 4-5(a)-(b) shows TCS in aqueous phase, on resins, and total TCS remaining (addition of TCS in aqueous phase and on resins) for Pd/IRA-900 and Pd/IRA-958, respectively, when loading of 0.2 wt.% Pd. For IRA-958 there is no TCS remaining on the resins, indicating of the reduction of TCS in aqueous phase was due to degradation. For IRA-900, TCS was detected on the resins, so the TCS reduction in aqueous phase was partially due to degradation and partially due to adsorption by resin support. From **Figure 4-5(a)** (Pd/IRA-900), it is noted that the concentration of TCS on the resins was increased in the first hour, and then decreased after that, with a peak amount of 20% of initial TCS at 60 min. As the adsorption rate was faster than HDC rate in the first hour, TCS increased on the resin surface, however, with TCS accumulation, adsorption rate decreased and HDC rate exceeded, which resulted in a decreasing amount of TCS on the resins. When the Pd loading was increased to 2.0 wt.%, the HDC rate increased, and there was no more TCS detected on the resins (**Figure 4-5(c)**), which indicates the adsorption may become the rate-limiting step.

Considering the reactant adsorption affinity on the two resins is different, the HDC rate of TCS over 0.2 wt.% supported Pd catalysts (i.e., the total TCS remaining in

the system) with different resins was compared in **Figure 4-5(d)**. These results show the TCS reduction rate due to HDC reaction was comparable for the two resins, which indicate adsorption of TCS on the catalysts is not a key role in this reaction. The HDC rate of the TCS was controlled by formation of highly reactive atomic hydrogen ($H\cdot$) or C-Cl cleavage. This observation is different from Zhou et al. (2013). They studied catalytic HDC of chloroacetic acids over supported Pd catalysts with different supports including ZrO_2 , SiO_2 , and AC, and found a much higher reactivity of Pd supported by ZrO_2 than the other two supports. They attributed this high reactivity to the strong electrostatic attraction between chloroacetic acids and ZrO_2 , which leads to an enhanced adsorption and thus elevated HDC rate. However, in their study they only analyzed chloroacetic acids concentration in aqueous phase and considered the “superficial” decreasing rate as HDC rate, however, this may count the adsorption of chloroacetic acids into the HDC removal.

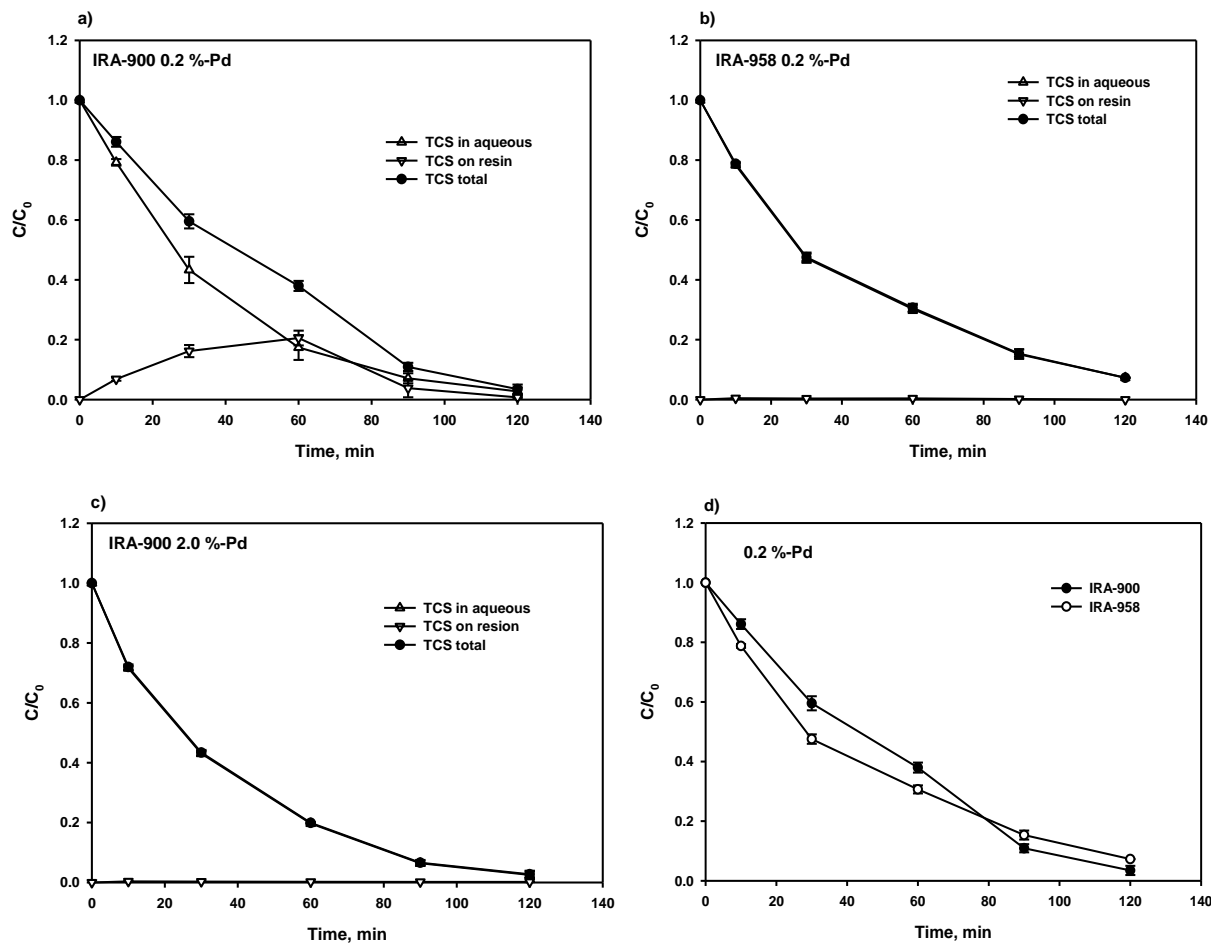


Figure 4-5. TCS adsorbed and degraded in the process of catalytic HDC with (a) 0.2 wt.% Pd/IRA-900, (b) 0.2 wt.% Pd/IRA-958, (c) 2.0 wt.% Pd/IRA-900, and (d) comparison of the degradation rate of TCS over catalysts of 0.2 wt.% Pd loading on two resins. Initial [TCS] = 2.9 mg/L, resin = 1 g/L.

4.3.4 Lifetime of the catalyst

The lifetime and reusability of the resin-supported Pd catalysts were tested with a 2.0 wt.% Pd loading, through eight consecutive runs of HDC of TCS where the same catalysts were repeatedly used without any treatment. The HDC kinetics of TCS in run 2, 4, 6, and 8 are shown in **Figure 4-6(a)-(b)**, where data for run 1, 3, 5, and 7 are not shown for brevity. The results show only 1.8 % and 0.4 % reactivity loss at the end of 2 hours after eight exhausting runs for IRA-900 and IRA-958, respectively. At the end of 8 consecutive runs, Pd bleeding in the aqueous phase was undetectable (i.e., < 0.03 mg/L or <0.2 % of initial Pd). This result confirms that the synthesized catalyst could reduce Pd leaching from the resin support because of the strong specific interaction between the resins and Pd.

Figure 4-6(c)-(d) shows the linearized kinetic profile by fitting the pseudo-first-order rate equation. The k_{obs} values for runs 2, 4, 6, 8 were determined to be 1.26 ± 0.01 L/g/min, 1.20 ± 0.01 L/g/min, 1.16 ± 0.01 L/g/min, 1.09 ± 0.01 L/g/min for Pd/IRA-900, and 1.45 ± 0.04 L/g/min, 1.55 ± 0.06 L/g/min, 1.40 ± 0.02 L/g/min, 1.40 ± 0.02 L/g/min for Pd/IRA-958, respectively. After 8 cycles of reuse, Pd/IRA-958 almost has no catalytic activity loss. Compared to IRA-958, IRA-900 has a little higher catalytic activity decrease after 8 exhausting runs, which may be due to organic products fouling (Concibido et al., 2007; Yuan and Keane, 2003). Yuan and Keane (2003) used Pd/Al₂O₃ and Pd/AC as catalysts to HDC of dichlorophenol, and found a loss of 50% surface area in used Pd/AC. Considering the AC is a good adsorbent for organic products, and after a temperature programmed reduction (TPR) the surface area was almost recovered, they suggested the organic reactant and products fouling on the AC supported catalysts is the

reason that cause deactivation of the catalysts. At similar situation, IRA-900 is easier to adsorb reaction products because its high affinity to organic compounds, and thus, the catalytic activity loss for Pd/IRA-900 may be due to products poisoning.

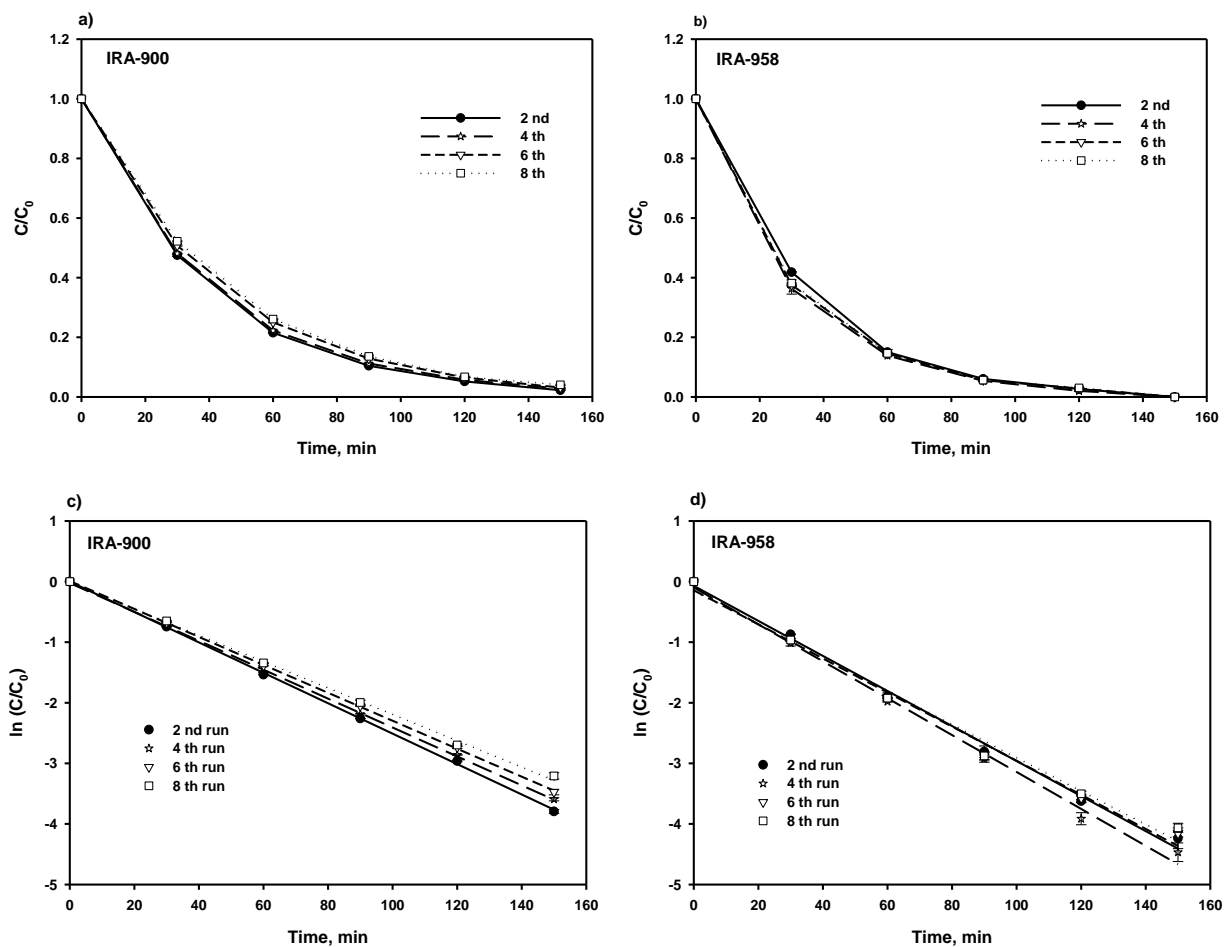


Figure 4-6. Catalytic HDC of TCS in eight consecutive batch tests where the Pd catalysts supported on resins (a) IRA-900 and (b) IRA-958 were repeatedly used, and linearized pseudo first-order plot for (c) IRA-900 and (d) IRA-958. Initial [TCS] = 2.9 mg/L, resin = 1 g/L, Pd = 2.0 wt.% of resin.

4.3.5 Effect of humic acid

Dissolved natural organic matter inhibition has been reported to be an issue for Pd-based catalysts (Chaplin et al., 2006; Kopinke et al., 2010; Zhang et al. 2013). For the amphiphilic resins, organic matter fouling of the catalysts is a concern. Humic acid (HA) is the major natural organic matter existing in soil, surface water, and groundwater (Stevenson, 1994). **Figure 4-7(a)-(b)** shows HDC kinetics of TCS with supported Pd (2.0 wt.%) catalysts at various concentrations of HA measured as TOC. At a TOC concentration of 10 mg/L, there is no significant impact on the HDC rate of TCS. The k_{obs} values were only reduced from 1.25 ± 0.06 L/g/min to 1.18 ± 0.04 L/g/min for Pd/IAR-900, and 1.6 ± 0.1 L/g/min to 1.5 ± 0.2 L/g/min for IRA-958. When the TOC concentration was increased to 20 mg/L, inhibition was exhibited, and k_{obs} values decreased to 0.95 ± 0.04 L/g/min and 1.24 ± 0.01 L/g/min for IRA-900 and IRA-958, respectively. With the addition of 30 mg/L TOC, the k_{obs} values further decreased to 0.9 ± 0.2 L/g/min and 1.17 ± 0.06 L/g/min for IRA-900 and IRA-958, respectively.

In the presence of HA, HA could compete with TCS to serve as an atomic hydrogen (H \cdot) acceptor by carboxyl or ketone group, inhibiting the HDC rate of the reactant (Zhu et al., 2008). In addition, HA can adsorb onto the catalyst surface sites causing catalyst fouling (Chaplin et al., 2006). Zhang et al. (2013) investigated HDC of trichloroethylene with alumina-supported Pd catalysts, and reported a ~88% reduction of reaction rate constant with presence of 30 mg/L TOC. Chaplin et al. (2006), reported the rate constants of NO $_3^-$ reduction decreased 84% on addition of 3.3 mg/L TOC of HA with the Pd-Cu/Al $_2$ O $_3$ catalyst. However, in our case, the HDC rate constants was only

reduced 28 % and 25 % in the presence of 30 mg/L TOC as HA for IRA-900, and IRA-958, respectively.

The probable reason of less inhibition by natural organic matter for resin-supported catalysts is that HA is less adsorbed on resins compared to other supports. Total organic carbon (TOC) analysis showed that 37% and 24% of HA was adsorbed on the Pd/IRA-900 and Pd/IRA-958, respectively, after 2 h of reaction in the presence of 30 mg/L TOC. Zhang et al. (2013) reported the Pd/Al₂O₃ catalysts adsorbed 59% in 5 min and 63% in 30 min of the 30 mg/L TOC. Our resin support adsorbed less HA than alumina may be because that the HA powder contains significant quantities of Ca (1.07 wt.%) and Fe (1.09 wt.%) (Chaplin et al., 2006), and these metal oxides are easily adsorbed by inorganic supports such as alumina.

To further investigate the natural organic matter inhibition effect, consecutive exhausting runs of catalytic HDC were conducted in presence of 30 mg/L TOC. **Figure 4-7(c)-(d)** shows kinetic profiles of HDC of TCS using Pd/IRA-900 and Pd/IRA-958 catalysts in presence of 30 mg/L TOC through six consecutive runs. The k_{obs} values for runs 2, 4, 6 were 0.7 ± 0.2 L/g/min, 0.6 ± 0.1 L/g/min, 0.57 ± 0.07 L/g/min for Pd/IRA-900, and 0.98 ± 0.07 L/g/min, 0.93 ± 0.01 L/g/min, 0.90 ± 0.03 L/g/min for Pd/IRA-958, respectively. After 6 exhausting runs, the observed rate constants decreased 39% and 27% compared with the first run for Pd/IRA-900 and Pd/IRA-958, respectively. The TOC analysis shows that after 10 h, 67% and 37% of HA (30 mg/L as TOC) was adsorbed by Pd/IRA-900 and Pd/IRA-958 respectively. Resin IRA-900 has higher affinity to natural organic matter, which leads to an easier organic fouling.

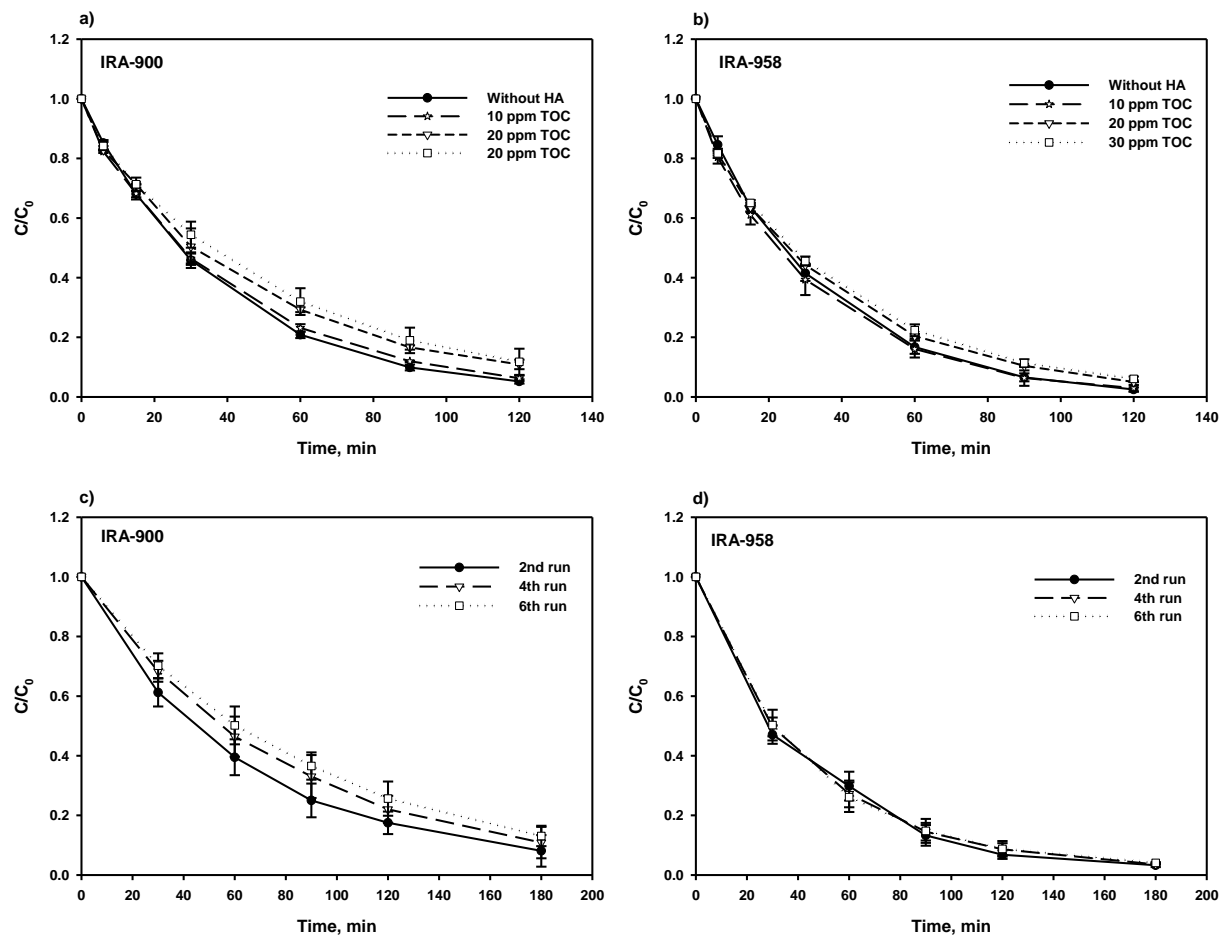


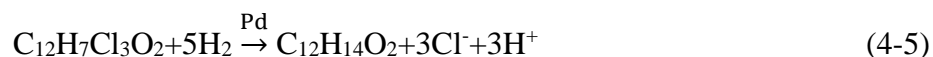
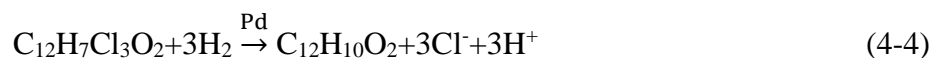
Figure 4-7. HDC of TCS using resin (a) IRA-900 and (b) IRA-958 supported Pd catalysts in the presence of various concentrations of humic acid, and HDC of TCS using (c) Pd/IRA-900 and (d) Pd/IRA-958 supported catalysts in presence of 30 mg/L HA as TOC through six consecutive runs. Initial [TCS] = 2.9 mg/L, resin = 1 g/L, Pd = 2.0 wt.% of resin.

4.3.6 Hydrodechlorination pathway of TCS in liquid phase

Oxidative degradation of TCS was reported to produce highly toxic byproducts, such as chlorodioxins and chlorophenol (Kanetoshi et al. 1987; 1988). To characterize catalytic HDC byproducts and pathway, the reaction system including liquid and solid phases was extracted by dichloromethane in selected times and analyzed using GC/MS. **Figure 4-8** shows the GC chromatography obtained from the HDC of TCS with the resin-supported Pd catalysts at 10 min, 30 min, 2 h, and 5h. As can be seen, TCS was rapidly converted and lost chlorine under ambient operation conditions. Complete dechlorination was achieved at 2 h, and after which no chlorinated organic compounds were detected by GC/MS. In the reaction process, several chlorinated byproducts were detected as three of the chlorines in the parent compound dechlorinated successively, and isomers of two chlorinated byproducts were detected. The chlorinated byproducts were present at low concentrations with the peak areas were all less than 1% of initial TCS area, which indicated a high efficiency of the HDC process catalyzed by resin-supported Pd.

The two main byproducts obtained from this process were *o*-phenoxyphenol and another byproduct. *o*-phenoxyphenol is also an antibiotic agent used as bacteriostats, fungicides, and sanitizers. The other product could not be identified, but the mass spectra shows the molecular weight of the product is 190 while the molecule contains a phenolic group. This product is suggested to be 2-(cyclohex-1-enyloxy)phenol, a ring-opening product of *o*-phenoxyphenol, but further investigation is needed to confirm this byproduct. Sun et al. (2007) also found ring-opening products in HDC of *o*-chlorophenol. The HDC pathway of TCS with resin-supported Pd as catalysts was schemed in **Figure 4-9**.

Based on the products analysis, the TCS HDC can be expressed as following Eqs:



Based on the two equations, hydrogen supply in the system (H_2 solubility ≈ 1.6 mg/L at 20°C) was more than 10 times the stoichiometric demand. The experiment system assures abundant amount hydrogen supply for catalytic HDC, so the incompletely cleaved benzene ring was not due to insufficient of hydrogen gas.

To further study dechlorination process, chlorine balance was investigated. **Figure 4-10** shows the rate of TCS degradation and chloride ion production with resin IRA-958 supported Pd and in the presence of hydrogen. It was shown that dechlorination of TCS is nearly stoichiometrically coupled with production of chloride (including in aqueous phase and adsorbed by resins). From **Figure 4-10**, it is noted that a little loss of chlorine mass occurred in the first hour of HDC, which confirms the very low concentration of chlorinated intermediate byproducts were presence in the first hour of HDC. This observation is consistent with GC/MS analysis. After about 1 h, no loss of chlorine was shown, thus confirming that no other chlorinated species were present beside TCS and chloride ions. This observation indicates that the supported Pd catalysts were able to rapid and complete HDC of TCS.

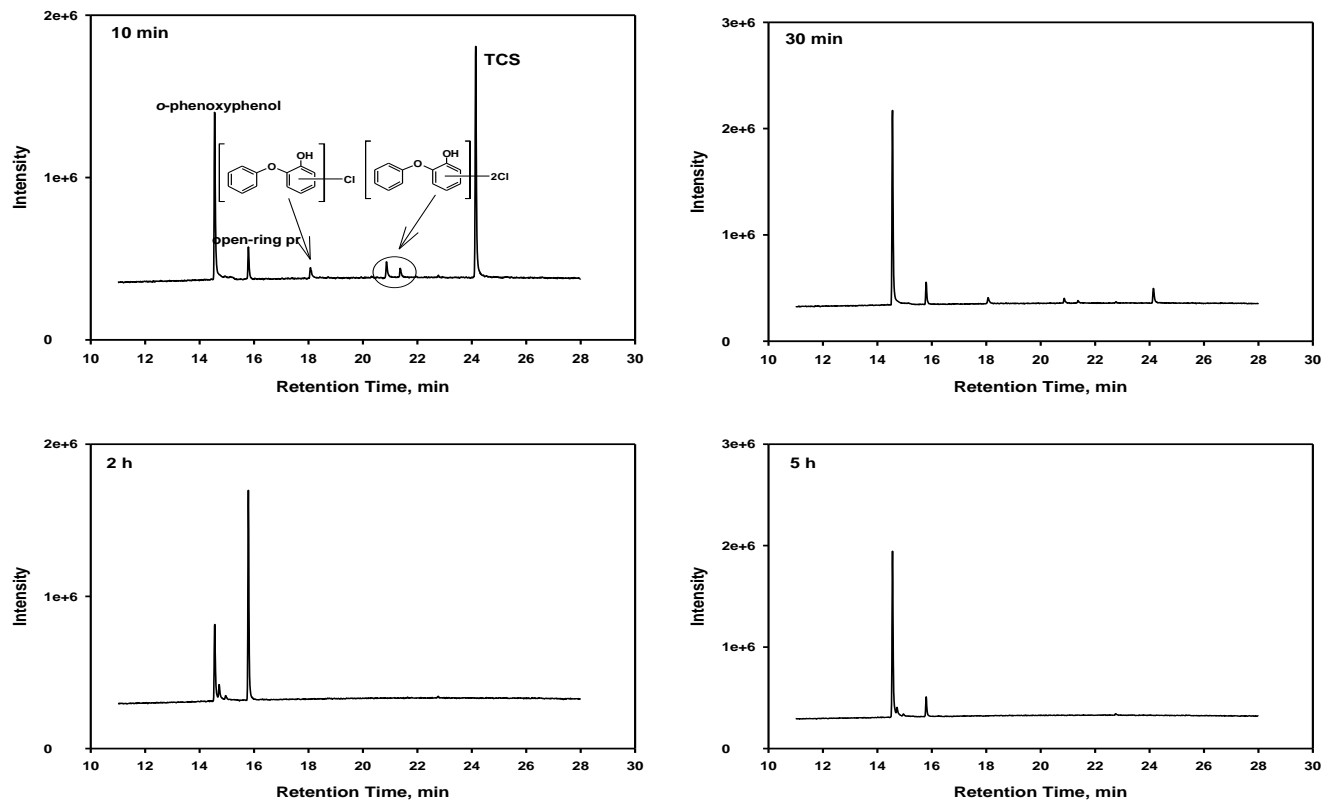


Figure 4-8. GC/MS chromatogram of TCS HDC byproducts. Initial [TCS] = 2.9 mg/L, resin = 1 g/L, Pd = 2.0 wt.% of resin.

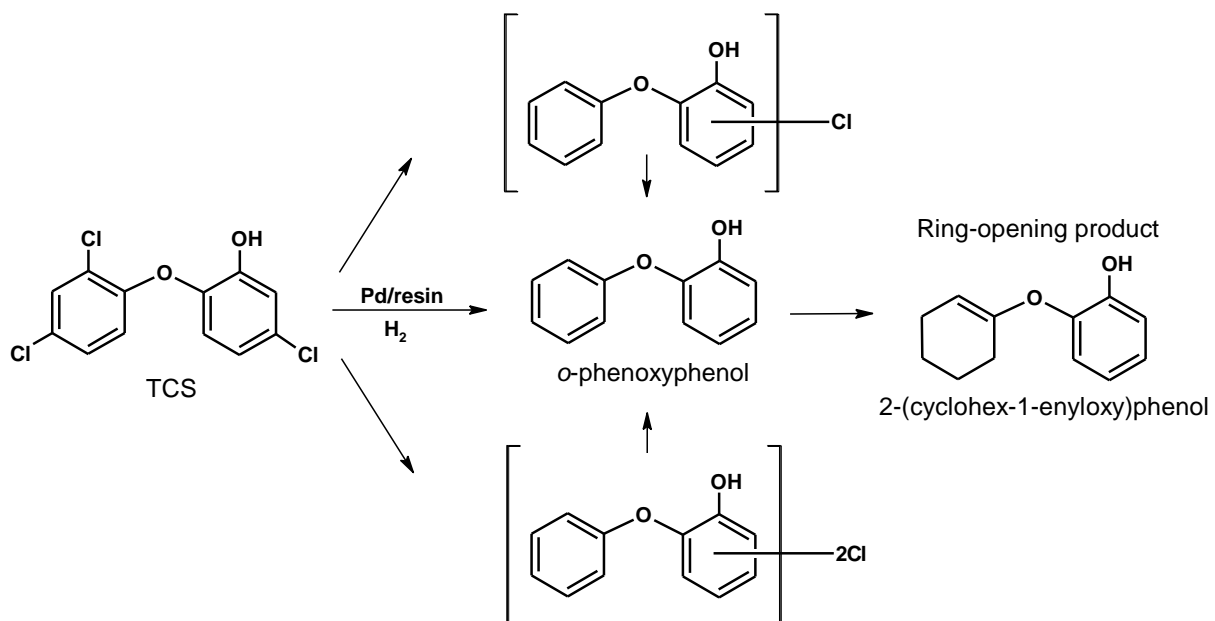


Figure 4-9. Schematic representation for catalytic HDC of TCS

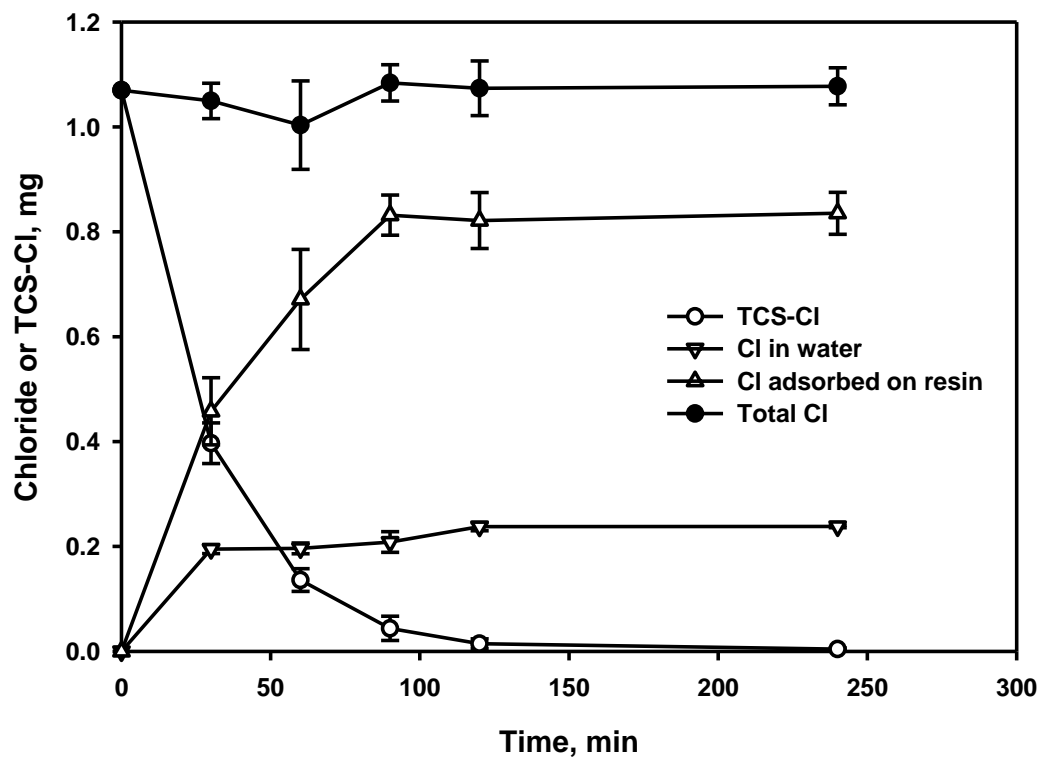


Figure 4-10. Concentration histories of Cl^- in aqueous phase, Cl^- adsorbed on resins, and TCS-Cl (i.e., TCS-bounded Cl) during HDC of TCS using IRA-958 supported Pd catalysts. Initial TCS = 2.9 mg/L, resin = 1 g/L, Pd = 2.0 wt.% of resin.

4.4. Conclusions

Two types of strong basic anion exchange resins supported Pd catalysts (Pd/IRA-900 and Pd/IRA-958) were prepared by a two-step process of ion-exchange followed by a reduction process. The ion-exchange process ensures a specific interaction between Pd and resins. At a Pd loading of 0.2 wt.%, the resin-supported Pd catalysts were able to effectively catalyze HDC of TCS with an observed pseudo-first-order reaction rate constant k_{obs} larger than 12 L/g/min. Due to different hydrophobicity of the two resins, IRA-900 supported catalysts exhibit higher adsorption affinity to TCS, however, this higher adsorption did not lead to a higher reaction rate. With an increase of Pd loading, the apparent rate constant k_{app} is increased for IRA-958 supported catalysts until an optimal Pd loading is reached. Further increase of Pd loading will cause Pd aggregation on the surface resulting in a blockage of the reactive sites of Pd particles. This resin-supported Pd catalyst has a long lifetime with minimum Pd bleeding (undetectable after 8 run cycles). In addition, this resin-supported catalyst is highly resistant to organic fouling. The observed rate constant k_{obs} was only decreased by 28 % and 25 % in the presence of 30 mg/L TOC for Pd/IRA-900 and Pd/IRA-958, respectively. The resin prevented natural organic matter (humic acid) fouling by being resistant to humic acid adsorption. GC/MS analysis showed several chlorinated intermediates with very low concentration were present in the early stage of HDC process, but complete dechlorination was achieved in about 2 hours. A non-carcinogenic or -mutagenic antibiotic *o*-phenoxyphenol and its ring-opened product were the main products of HDC of TCS. Catalytic HDC with resin-supported Pd catalysts have proved to be a promising solution for complete

dechlorination of the chlorinated pollutants and diminish highly toxic byproducts produced by other degradation methods.

CHAPTER 5. CONCLUSIONS AND SUGGESTIONS FOR FUTURE RESEARCH

5.1 Summary and conclusions

Application of various synthesized nanoparticles for environmental remediation has attracted great interest in recent years. For the first time, this research demonstrates synthesis of a new class of carboxymethyl cellulose (CMC) stabilized MnO_2 nanoparticles for oxidative degradation of pollutants in groundwater. The feasibility of using the nanoparticles for in-situ degradation of a model endocrine disrupting chemical (EDC), 17β -estradiol was investigated. This work was divided into two parts: First, we synthesized the nanoparticles and investigated the factors that could influence the nanoparticle reactivity. Second, we tested the nanoparticle deliverability in the groundwater aquifer and using column tests to simulate the in-situ remediation, allowing for investigation of operating parameters to improve degradation efficiency.

CMC was able to act as a low-cost and green stabilizer for synthesizing well-stabilized birnessite (δ - MnO_2) nanoparticles. A zeta potential of -34 ± 2 mV for CMC- MnO_2 ($\text{MnO}_2 = 0.017$ g/L, pH = 5.1, $I \cong 2.4 \times 10^{-4}$ M) indicates good stabilization of the nanoparticles due to electrostatic repulsion. While conventional non-stabilized MnO_2 particles aggregate rapidly, CMC-stabilized nanoparticles remain well-dispersed in aqueous suspension for one year. The most desired particles (small size and narrow size distribution) were obtained at a CMC/ MnO_2 molar ratio of 1.39×10^{-3} , which yielded a mean hydrodynamic size of 39.5 nm and a narrowest size distribution (SD=0.8 nm) with about 90% of the particles falling between 20 and 50 nm. The TEM image confirms that

the CMC stabilization resulted in fully stabilized discrete nanoparticles with a mean size of 37 ± 10 nm.

At natural pH (6-7), CMC-stabilized MnO_2 exhibited faster degradation kinetics for oxidation of E2 than non-stabilized MnO_2 in both aqueous phase and soil phase. The high reactivity of CMC- MnO_2 , compared to non-stabilized MnO_2 in degradation of water soluble E2, was due to the large surface reactive sites of the nanoparticles. This reactivity advantage becomes more evident when used for treating soil-sorbed E2 owing to the ability of CMC to complex with metal ions and shield the reactive sites from binding with soil metal ions that inhibit E2 oxidation. The more negative zeta potential of CMC-stabilized MnO_2 forecasts a less favorable sorption potential to the soil, i.e., less reactivity loss. Overall, CMC-stabilized MnO_2 displayed much greater resistance to soil inhibitive effects such as soil-released metals and soil- MnO_2 interactions than non-stabilized MnO_2 .

The direct injection of nanoparticles into contaminated aquifers has been suggested as a promising technology for in-situ remediation of contaminants. This work has tested the deliverability of the nanoparticles in column transport tests using three natural sandy loams (SL1, SL2, and SL3) as model soils. The nanoparticles can be well delivered through the three soils of with a full breakthrough level C/C_0 of 0.90, 0.93, and 0.66. The retention of the nanoparticles in the soils may influenced by several factors concerning 1) nanoparticle surface chemistry, 2) soil surface chemistry and geochemical heterogeneities, and 3) groundwater hydrology. MnO_2 nanoparticle deposition is much higher in soils that offer more favorable deposition sites than those are unfavorable for deposition, which could be predicted based on the collector average surface potential.

Higher MnO₂ nanoparticle deposition could occur in soils that offer high charge heterogeneities which contain high clay fraction, and in low groundwater flow conditions.

This study used laboratory column degradation tests to simulate the in-situ degradation conditions, and results showed that the degradation efficiency of the nanoparticles may be influenced by several factors, such as soil properties, particle injection velocity, and particle injection concentration. The combination of these factors affects the nanoparticle degradation behavior in one key aspect, i.e., the contact time of the nanoparticles with the contaminants. The nanoparticles are more effective for soils of moderate or high organic contents that offer slow estradiol desorption rate and faster MnO₂ breakthrough, which allowed sufficient contact and reaction time to complete the degradation. For the same soil, reducing injection velocity could increase particle and contaminant contact time, but on the other hand, reducing velocity could also increase nanoparticle retention by the soil. Therefore, choosing an optimal nanoparticle injection velocity is important. Results obtained from this research show that it is very promising to apply the CMC-stabilized MnO₂ nanoparticles for the in-situ oxidative degradation of estradiol in various contaminated soils.

Triclosan is a broad-spectrum antibacterial contained in personal care and household products. For the first time, this research investigates the destruction of TCS by dechlorination, using two types of strong basic anion exchange resin-supported Pd as catalysts. The catalysts were prepared by a two-step process of ion-exchange and subsequent reduction. The ionic binding between the Pd anion and resins ensures a specific interaction between Pd and resins, thus suppressing the Pd bleeding from the resin supports. These resin-supported Pd catalysts show a high catalytic activity. At a Pd

loading of 0.2 wt.%, the synthesized Pd catalysts were able to effectively catalyze HDC of TCS with an observed pseudo-first-order reaction rate constant k_{obs} larger than 12 L/g/min. With an increase of Pd loading, the apparent rate constant k_{app} is increased until an optimal Pd loading is reached. Further increase of Pd loading will cause Pd aggregation on the surface resulting in a blockage of reactive sites of Pd particles. These resin-supported catalysts are highly resistant to organic fouling. The observed rate constant, k_{obs} in presence of 30 mg/L TOC for Pd/IRA-900, and Pd/IRA-958, was only decreased 28 % and 25 % respectively. Because of the minimum Pd bleeding and high resistance to organic fouling, these synthesized catalysts have long lifetimes with only 1.8 % and 0.4 % reactivity loss after 8th exhausting runs for IRA-900 and IRA-958, respectively. GC/MS analysis showed that several chlorinated intermediates with very low concentrations were present in the early stage of HDC process, but complete dechlorination was achieved in about 2 hours. A non-carcinogenic or -mutagenic antibiotic *o*-phenoxyphenol and its ring-open product were the main products of HDC of TCS. Catalytic HDC with resin-supported Pd catalysts has proved to be a promising solution for complete dechlorination of the chlorinated pollutants and diminish highly toxic byproducts produced by other degradation method.

5.2 Suggestions for future work

Injection of nanomaterial is suggested to offer a powerful strategy for remediation of contaminants in groundwater that are not accessible by conventional technologies. However, to the best of our knowledge, just a few pilot- or field scale studies have been performed to investigate a full analysis of the effectiveness, practicability, capital and operating costs of this nanomaterial remediation technology. More future field-scale

demonstrations need to be conducted to enable engineers to make more informed decisions on this new technology choice and operation.

In addition to efficiency and cost consideration, it is also important that the ultimate environmental sustainability of this technology is considered for site cleanup. Taking long term environmental impact into consideration, two questions remain unanswered: One being the long-term fate and transport of the nanoparticles in environment, and the other being the environmental impacts of the applied nanoparticles.

Research on nanoparticle toxicology, and on their fate and transport have been two common research priorities since the beginning of development of nanotechnology. In a review discussing the toxicology of nanoparticles (Oberdorster et al., 2005), it was demonstrated that various small nanoparticles increased toxicity due to an increase in surface area. Stefanescu et al. (2009) examined the toxicity of Mn oxide nanomaterials in a neuronal precursor cell model, and found that for the same material (Mn_3O_4 nanoparticles), the cytotoxicity was dependent on size, and larger specific surface area nanoparticles were observed to have higher toxicity. But for different nanomaterials, the toxicity was not proportional to particle size. Dunphy et al. (2006) also suggested particle structure and composition may also play a role in toxicity other than particle size. When exposed to Mn oxide nanomaterials, reactive oxygen species are generated, and cell death occurred resulting from oxidative stress (Stefanescu et al., 2009).

The overall understanding of the environmental impact of nanoparticles is dependent on the application of environmental conditions, such as, pressure, biochemical reaction, solution chemistry, and aquifer properties. Also, more information is needed in order to determine the unknown toxicity and environmental impact, which is necessary to

establish nanotechnology application regulations and gain the public acceptance for using nanomaterial for in-situ remediation.

Future work on Pd-based catalytic HDC, complemented with advanced characterization techniques and atomistic simulations is necessary in order to understand the macroscopic reaction rate and reaction transformation from molecular-scale process. Experimental work should also focus on the catalyst structure and its relation to the observed catalytic activity. In addition, the relationships between contaminant structure and reactivity of the catalytic HDC should be a primary focus in the future work. Further efforts are needed to conduct pilot- and field scale of investigations, to identify the catalytic HDC technology barriers and to develop the practical treatment strategies.

REFERENCES

- Adamczyk, Z., Siwek, B., Zembala, M. and Belouschek, P., 1994. Kinetics of localized adsorption of colloid particles. *Adv. Colloid Interfac.* 48, 151-280.
- An, B., Liang, Q.Q. and Zhao, D.Y., 2011. Removal of arsenic(V) from spent ion exchange brine using a new class of starch-bridged magnetite nanoparticles. *Water Res.* 45(5), 1961-1972.
- Andersin, J. and Honkala, K., 2011. First principles investigations of Pd-on-Au nanostructures for trichloroethene catalytic removal from groundwater. *Phys. Chem. Chem. Phys.* 13(4), 1386-1394.
- Aranami, K. and Readman, J.W., 2007. Photolytic degradation of triclosan in freshwater and seawater. *Chemosphere* 66(6), 1052-1056.
- Arye, G., Dror, I. and Berkowitz, B., 2011. Fate and transport of carbamazepine in soil aquifer treatment (SAT) infiltration basin soils. *Chemosphere* 82(2), 244-252.
- Barnes, K.K., Kolpin, D.W., Furlong, E.T., Zaugg, S.D., Meyer, M.T. and Barber, L.B., 2008. A national reconnaissance of pharmaceuticals and other organic wastewater contaminants in the United States - I) Groundwater. *Sci. Total Environ.* 402(2-3), 192-200.
- Basnet, M., Di Tommaso, C., Ghoshal, S. and Tufenkji, N., 2015. Reduced transport potential of a palladium-doped zero valent iron nanoparticle in a water saturated loamy sand. *Water Res.* 68, 354-363.

- Bedoux, G., Roig, B., Thomas, O., Dupont, V. and Le Bot, B., 2012. Occurrence and toxicity of antimicrobial triclosan and by-products in the environment. *Environ. Sci. Pollut. R.* 19(4), 1044-1065.
- Bester, K., 2003. Triclosan in a sewage treatment process - balances and monitoring data. *Water Res.* 37(16), 3891-3896.
- Bennett, P., He, F., Zhao, D.Y., Aiken, B. and Feldman, L., 2010. In situ testing of metallic iron nanoparticle mobility and reactivity in a shallow granular aquifer. *J. Contam. Hydrol.* 116(1-4), 35-46.
- Bergendahl, J. and Grasso, D., 2000. Prediction of colloid detachment in a model porous media: hydrodynamics. *Chem. Eng. Sci.* 55(9), 1523-1532.
- Biffis, A., Landes, H., Jerabek, K. and Corain, B., 2000. Metal palladium dispersed inside macroporous ion-exchange resins: the issue of the accessibility to gaseous reactants. *J. Mol. Catal. A-Chem.* 1 151(1-2), 283-288.
- Bolster, C.H., A.L. Mills, G.M. Hornberger, and Herman, J.S., 1999. Spatial distribution of bacteria experiments in intact cores. *Water Resour. Res.* 35,1797–1807.
- Bouyoucos, G.J., 1962. Hydrometer method improved for making particle size analyses of soils. *Agron. J.* 54, 464-465.
- Chaplin, B.P., Reinhard, M., Schneider, W.F., Schueth, C., Shapley, J.R., Strathmann, T.J. and Werth, C.J., 2012. Critical review of Pd-based catalytic treatment of priority contaminants in water. *Environ. Sci. Technol.* 46(7), 3655-3670.
- Chaplin, B.P., Roundy, E., Guy, K.A., Shapley, J.R. and Werth, C.J., 2006. Effects of natural water ions and humic acid on catalytic nitrate reduction kinetics using an alumina supported Pd-Cu catalyst. *Environ. Sci. Technol.* 40(9), 3075-3081.

- Chen, N., Rioux, R.M. and Ribeiro, F.H., 2002. Investigation of reaction steps for the hydrodechlorination of chlorine-containing organic compounds on Pd catalysts. *J. Catal.* 211(1), 192-197.
- Clarke, C.E. and Johnson, K.L., 2010. Oxidative breakdown of acid orange 7 by a manganese oxide containing mine waste: Insight into sorption, kinetics and reaction dynamics. *Appl. Catal. B-Environ.* 101(1-2), 13-20.
- Colborn, T., Saal, F.S.V. and Soto, A.M., 1993. Developmental effects of endocrine-disrupting chemicals in wildlife and humans. *Environ. Health Persp.* 101(5), 378-384.
- Concibido, N.C., Okuda, T., Nishijima, W. and Okada, M., 2007. Deactivation and reactivation of Pd/C catalyst used in repeated batch hydrodechlorination of PCE. *Appl. Catal. B-Environ.* 71(1-2), 64-69.
- D'Archivio, A.A., Galantini, L., Tettamanti, E., Panatta, A. and Corain, B., 2000. Metal palladium dispersed inside macroporous ion-exchange resins: rotational and translational mobility inside the polymer network. *J. Mol. Catal. A-Chem.* 157(1-2), 269-273.
- Delgado, J.A., Uguina, M.A., Sotelo, J.L., Ruiz, B. and Rosario, M., 2007. Separation of carbon dioxide/methane mixtures by adsorption on a basic resin. *Adsorption* 13(3-4), 373-383.
- Desbrow, C., Routledge, E.J., Brighty, G.C., Sumpter, J.P. and Waldock, M., 1998. Identification of estrogenic chemicals in STW effluent. 1. Chemical fractionation and in vitro biological screening. *Environ. Sci. Technol.* 32(11), 1549-1558.

- Diamanti-Kandarakis, E., Bourguignon, J.P., Giudice, L.C., Hauser, R., Prins, G.S., Soto, A.M., Zoeller, R.T. and Gore, A.C., 2009. Endocrine-disrupting chemicals: An endocrine society scientific statement. *Endocr. Rev.* 30(4), 293-342.
- Diaz, E., Mohedano, A.F., Casas, J.A., Calvo, L., Gilarranz, M.A. and Rodriguez, J.J., 2011. Comparison of activated carbon-supported Pd and Rh catalysts for aqueous-phase hydrodechlorination. *Appl. Catal. B-Environ.* 106(3-4), 469-475.
- Drewes, J.E., Heberer, T., Rauch, T. and Reddersen, K., 2003. Fate of pharmaceuticals during ground water recharge. *Ground Water Monit. Remediat.* 23(3), 64-72.
- Dunphy Guzman, K.A., Taylor, M.R., and Banfield, J.F., 2006. Environmental risks of nanotechnology: national nanotechnology initiative funding, 2000-2004. *Environ. Sci. Technol.*, 40(5), 1401-1407.
- Feng, Y., Wang, C., Liu, J., Zhang, Z., 2010. Electrochemical degradation of 17-alpha-ethinylestradiol (EE2) and estrogenic activity changes. *J. Environ. Monit.* 12,404–408.
- Finlay-Moore, O., Hartel, P.G. and Cabrera, M.L., 2000. 17 beta-estradiol and testosterone in soil and runoff from grasslands amended with broiler litter. *J. Environ. Qual.* 29(5), 1604-1611.
- Gasparovicova, D., Kralik, M., Hronec, M., Biffis, A., Zecca, M. and Corain, B., 2006. Reduction of nitrates dissolved in water over palladium-copper catalysts supported on a strong cationic resin. *J. Mol. Catal. A-Chem.* 244(1-2), 258-266.
- Gong, Y.Y., Liu, Y.Y., Xiong, Z., Kaback, D. and Zhao, D.Y., 2012. Immobilization of mercury in field soil and sediment using carboxymethyl cellulose stabilized iron sulfide nanoparticles. *Nanotechnology* 23(29).

- Greluk, M. and Hubicki, Z., 2010. Kinetics, isotherm and thermodynamic studies of Reactive Black 5 removal by acid acrylic resins. *Chem. Eng. J.* 162(3), 919-926.
- Halden, R.U., 2014. On the need and speed of regulating triclosan and triclocarban in the United States. *Environ. Sci. Technol.* 48(7), 3603-3611.
- Halden, R.U. and Paull, D.H., 2005. Co-occurrence of triclocarban and triclosan in US water resources. *Environ. Sci. Technol.* 39(6), 1420-1426.
- Han, B., Zhang, M., Zhao, D.Y. and Feng, Y.C., 2015. Degradation of aqueous and soil-sorbed estradiol using a new class of stabilized manganese oxide nanoparticles. *Water Res.* 70, 288-299.
- Havlikova, L., Novakova, L., Matysova, L., Sicha, J. and Solich, P., 2006. Determination of estradiol and its degradation products by liquid chromatography. *J. Chromatogr. A* 1119 (1-2), 216-223.
- He, F., Zhang, M., Qian, T.W. and Zhao, D.Y., 2009. Transport of carboxymethyl cellulose stabilized iron nanoparticles in porous media: Column experiments and modeling. *J. Colloid Interface Sci.* 334(1), 96-102.
- He, F. and Zhao, D.Y., 2007. Manipulating the size and dispersibility of zerovalent iron nanoparticles by use of carboxymethyl cellulose stabilizers. *Environ. Sci. Technol.* 41(17), 6216-6221.
- He, F., Zhao, D.Y., Liu, J.C. and Roberts, C.B., 2007. Stabilization of Fe-Pd nanoparticles with sodium carboxymethyl cellulose for enhanced transport and dechlorination of trichloroethylene in soil and groundwater. *Ind. Eng. Chem. Res.* 46(1), 29-34.

- He, F., Zhao, D.Y. and Paul, C., 2010. Field assessment of carboxymethyl cellulose stabilized iron nanoparticles for in situ destruction of chlorinated solvents in source zones. *Water Res.* 44(7), 2360-2370.
- Heidler, J. and Halden, R.U., 2007. Mass balance assessment of triclosan removal during conventional sewage treatment. *Chemosphere* 66(2), 362-369.
- Hildebrand, C., Londry, K.L. and Farenhorst, A., 2006. Sorption and desorption of three endocrine disrupters in soils. *Journal of Environmental Science and Health Part B- Pesticides Food Contaminants and Agricultural Wastes* 41(6), 907-921.
- Hohenblum, P., Gans, O., Moche, W., Scharf, S. and Lorbeer, G., 2004. Monitoring of selected estrogenic hormones and industrial chemicals in groundwaters and surface waters in Austria. *Sci. Total Environ.* 333(1-3), 185-193.
- Huber, M.M., Canonica, S., Park, G.Y. and Von Gunten, U., 2003. Oxidation of pharmaceuticals during ozonation and advanced oxidation processes. *Environ. Sci. Technol.* 37(5), 1016-1024.
- Inaba, K., Doi, T., Isobe, N. and Yamamoto, T., 2006. Formation of bromo-substituted triclosan during chlorination by chlorine in the presence of trace levels of bromide. *Water Res.* 40(15), 2931-2937.
- Ishibashi, H., Matsumura, N., Hirano, M., Matsuoka, M., Shiratsuchi, H., Ishibashi, Y., Takao, Y. and Arizono, K., 2004. Effects of triclosan on the early life stages and reproduction of medaka *Oryzias latipes* and induction of hepatic vitellogenin. *Aquat.Toxicol.* 67(2), 167-179.

- Janiak, T. and Okal, J., 2009. Effectiveness and stability of commercial Pd/C catalysts in the hydrodechlorination of meta-substituted chlorobenzenes. *Appl. Catal. B-Environ.* 92(3-4), 384-392.
- Ji, L., Liu, F., Xu, Z., Zheng, S. and Zhu, D., 2010. Adsorption of pharmaceutical antibiotics on template-synthesized ordered micro- and mesoporous carbons. *Environ. Sci. Technol.* 44(8), 3116-3122.
- Jiang, L.Y., Chen, J.M., Zhu, R.Y., Huang, C. and Ji, H., 2010. Degradation kinetics and estrogenic activity of 17-estradiol removal by aqueous manganese dioxide. *J. Environ. Sci. Heal. A.* 45(8), 938-945.
- Jiang, L.Y., Huang, C., Chen, J.M. and Chen, X., 2009. Oxidative transformation of 17 beta-estradiol by MnO₂ in aqueous solution. *Arch. Environ. Contam. Toxicol.* 57(2), 221-229.
- Jiang, J.-Q., Zhou, Z. and Sharma, V.K., 2013. Occurrence, transportation, monitoring and treatment of emerging micro-pollutants in waste water - a review from global views. *Microchem. J.* 110, 292-300.
- Johnson, P.R., Sun, N. and Elimelech, M., 1996. Colloid transport in geochemically heterogeneous porous media: Modeling and measurements. *Environ. Sci. Technol.* 30(11), 3284-3293.
- Jones, E.H. and Su, C., 2014. Transport and retention of zinc oxide nanoparticles in porous media: Effects of natural organic matter versus natural organic ligands at circumneutral pH. *J. Hazard. Mater.* 275, 79-88.

- Joo, S.H. and Zhao, D. Y., 2008. Destruction of lindane and atrazine using stabilized iron nanoparticles under aerobic and anaerobic conditions: Effects of catalyst and stabilizer. *Chemosphere* 70(3), 418-425.
- Kanetoshi, A., Ogawa, H., Katsura, E. and Kaneshima, H., 1987. Chlorination of irgasan dp300 and formation of dioxins from its chlorinated derivatives. *J. Chromatog.* 389(1), 139-153.
- Kanetoshi, A., Ogawa, H., Katsura, E., Kaneshima, H. and Miura, T., 1988. Formation of polychlorinated dibenzo-para-dioxins upon combustion of commercial textile products containing 2,4,4'-trichloro-2'-hydroxydiphenyl ether (irgasan dp300). *J. Chromatog.* 442, 289-299.
- Kasprzyk-Hordern, B., Dinsdale, R.M. and Guwy, A.J., 2009. Illicit drugs and pharmaceuticals in the environment - forensic applications of environmental data. Part 1: Estimation of the usage of drugs in local communities. *Environ. Pollut.* 157(6), 1773-1777.
- Khanal, S.K., Xie, B., Thompson, M.L., Sung, S.W., Ong, S.K. and Van Leeuwen, J., 2006. Fate, transport, and biodegradation of natural estrogens in the environment and engineered systems. *Environ. Sci. Technol.* 40(21), 6537-6546.
- Kirsten, W.J., 1979. Automated methods for the simultaneous determination of carbon, hydrogen, nitrogen, and sulfur, and sulfur alone in organic and inorganic materials. *Anal. Chem.* 51, 1173-1179.
- Klamerth, N., Malato, S., Maldonado, M.I., Aguera, A. and Fernandez-Alba, A.R., 2010. Application of Photo-Fenton as a Tertiary Treatment of Emerging Contaminants in Municipal Wastewater. *Environ. Sci. Technol.* 44(5), 1792-1798.

- Ko, C.H. and Elimelech, M., 2000. The "shadow effect" in colloid transport and deposition dynamics in granular porous media: Measurements and mechanisms. *Environ. Sci. Technol.* 34(17), 3681-3689.
- Kolodynska, D., 2010. Cu(II), Zn(II), Ni(II), and Cd(II) Complexes with Hedp removal from industrial effluents on different ion exchangers. *Ind. Eng.Chem. Res.* 49(5), 2388-2400.
- Kolodziej, E.P., Harter, T. and Sedlak, D.L., 2004. Dairy wastewater, aquaculture, and spawning fish as sources of steroid hormones in the aquatic environment. *Environ. Sci. Technol.* 38(23), 6377-6384.
- Kolpin, D.W., Furlong, E.T., Meyer, M.T., Thurman, E.M., Zaugg, S.D., Barber, L.B. and Buxton, H.T., 2002. Pharmaceuticals, hormones, and other organic wastewater contaminants in us streams, 1999-2000: A national reconnaissance. *Environ. Sci. Technol.* 36(6), 1202-1211.
- Kopinke, F.-D., Angeles-Wedler, D., Fritsch, D. and Mackenzie, K., 2010. Pd-catalyzed hydrodechlorination of chlorinated aromatics in contaminated waters-Effects of surfactants, organic matter and catalyst protection by silicone coating. *Appl. Catal. B-Environ.* 96(3-4), 323-328.
- Kummerer K, Al-Ahmad A., 1997. Biodegradability of the anti-tumour agents 5-fluorouracil, cytarabine, and gemcitabine: impact of the chemical structure and synergistic toxicity with hospital effluent. *Acta Hydrochim. Hydrobiol.* 25,166–172.
- Latch, D.E., Packer, J.L., Stender, B.L., VanOverbeke, J., Arnold, W.A. and McNeill, K., 2005. Aqueous photochemistry of triclosan: Formation of 2,4-dichlorophenol, 2,8-

- dichlorodibenzo-p-dioxin, and oligomerization products. *Environ. Toxicol. Chem.* 24(3), 517-525.
- Laws, B.V., Dickenson, E.R.V., Johnson, T.A., Snyder, S.A. and Drewes, J.E., 2011. Attenuation of contaminants of emerging concern during surface-spreading aquifer recharge. *Sci. Total Environ.* 409(6), 1087-1094.
- Lee, L.S., Strock, T.J., Sarmah, A.K. and Rao, P.S.C., 2003. Sorption and dissipation of testosterone, estrogens, and their primary transformation products in soils and sediment. *Environ. Sci. Technol.* 37(18), 4098-4105.
- Li, W.C., 2014. Occurrence, sources, and fate of pharmaceuticals in aquatic environment and soil. *Environ. Pollut.* 187, 193-201.
- Li, Y., Wang, Y., Pennell, K.D. and Abriola, L.M., 2008. Investigation of the transport and deposition of fullerene (C60) nanoparticles in quartz sands under varying flow conditions. *Environ. Sci. Technol.* 42(19), 7174-7180.
- Lin, K.D., Liu, W.P. and Gan, J., 2009a. Reaction of tetrabromobisphenol a (TBBPA) with manganese dioxide: Kinetics, products, and pathways. *Environ. Sci. Technol.* 43(12), 4480-4486.
- Lin, K.D., Liu, W.P. and Gan, J., 2009b. Oxidative removal of bisphenol A by manganese dioxide: efficacy, products, and pathways. *Environ. Sci. Technol.* 43(10), 3860-3864.
- Lin, A.Y.C. and Reinhard, M., 2005. Photodegradation of common environmental pharmaceuticals and estrogens in river water. *Environ. Toxicol. Chem.* 24(6), 1303-1309.

- Lindstrom, A., Buerge, I.J., Poiger, T., Bergqvist, P.A., Muller, M.D. and Buser, H.R., 2002. Occurrence and environmental behavior of the bactericide triclosan and its methyl derivative in surface waters and in wastewater. *Environ. Sci. Technol.* 36(11), 2322-2329.
- Lowry, G.V. and Reinhard, M., 1999. Hydrodehalogenation of 1-to 3-carbon halogenated organic compounds in water using a palladium catalyst and hydrogen gas. *Environ. Sci. Technol.* 33(11), 1905-1910.
- Lowry, G.V. and Reinhard, M., 2001. Pd-catalyzed TCE dechlorination in water: Effect of H₂ (aq) and H₂-utilizing competitive solutes on the TCE dechlorination rate and product distribution. *Environ. Sci. Technol.* 35(4), 696-702.
- Lozano, N., Rice, C.P., Ramirez, M. and Torrents, A., 2010. Fate of triclosan in agricultural soils after biosolid applications. *Chemosphere* 78(6), 760-766.
- Mansell, B.L. and Drewes, J.E., 2004. Fate of steroidal hormones during soil-aquifer treatment. *Ground Water Monit. Remediat.* 24(2), 94-101.
- Marcano-Martinez, E. and McBride, M.B., 1989. Comparison of the titration and ion adsorption methods for surface charge measurement in oxisols. *Soil Sci. Am. J.* 1989, 53, 1040-1045.
- Mashtare, M.L., Khan, B. and Lee, L.S., 2011. Evaluating stereoselective sorption by soils of 17 alpha-estradiol and 17 beta-estradiol. *Chemosphere* 82(6), 847-852.
- McClellan, K. and Halden, R.U., 2010. Pharmaceuticals and personal care products in archived us biosolids from the 2001 EPA national sewage sludge survey. *Water Res.* 44(2), 658-668.

- McMurry, L.M., Oethinger, M. and Levy, S.B., 1998. Triclosan targets lipid synthesis. *Nature* 394(6693), 531-532.
- Mendez-Diaz, J.D., Prados-Joya, G., Rivera-Utrilla, J., Leyva-Ramos, R., Sanchez-Polo, M., Ferro-Garcia, M.A. and Medellin-Castillo, N.A., 2010. Kinetic study of the adsorption of nitroimidazole antibiotics on activated carbons in aqueous phase. *J. Colloid Interface Sci.* 345(2), 481-490.
- Mestre, A.S., Pires, R.A., Aroso, I., Fernandes, E.M., Pinto, M.L., Reis, R.L., Andrade, M.A., Pires, J., Silva, S.P. and Carvalho, A.P., 2014. Activated carbons prepared from industrial pre-treated cork: Sustainable adsorbents for pharmaceutical compounds removal. *Chem. Eng. J.* 253, 408-417.
- Murray, J.W., 1974. Surface chemistry of hydrous manganese-dioxide. *J. Colloid Interface Sci.* 46(3), 357-371.
- Nichols, D.J., Daniel, T.C., Edwards, D.R., Moe, P.A. and Pote, D.H., 1998. Use of grass filter strips to reduce 17 beta-estradiol in runoff from fescue-applied poultry litter. *J. Soil Water Conserv.* 53(1), 74-77.
- Nutt, M.O., Hughes, J.B. and Wong, M.S., 2005. Designing Pd-on-Au bimetallic nanoparticle catalysts for trichloroethene hydrodechlorination. *Environ. Sci. Technol.* 39(5), 1346-1353.
- Oberdorster, G., Oberdorster, E., and Oberdorster, J., 2005. Nanotoxicology: an emerging discipline evolving from studies of ultrafine particles, *Environ. Health Persp.* 113(7), 823-839.

- Onesios, K.M., Yu, J.T. and Bouwer, E.J., 2009. Biodegradation and removal of pharmaceuticals and personal care products in treatment systems: a review. *Biodegradation* 20, 441-466.
- Orvos, D.R., Versteeg, D.J., Inauen, J., Capdevielle, M., Rothenstein, A. and Cunningham, V., 2002. Aquatic toxicity of triclosan. *Environ. Toxicol. Chem.* 21(7), 1338-1349.
- Pal, A., Gin, K.Y.-H., Lin, A.Y.-C. and Reinhard, M., 2010. Impacts of emerging organic contaminants on freshwater resources: Review of recent occurrences, sources, fate and effects. *Sci. Total Environ.* 408(24), 6062-6069.
- Puma, G.L., Puddu, V., Tsang, H.K., Gora, A. and Toepfer, B., 2010. Photocatalytic oxidation of multicomponent mixtures of estrogens (estrone (E1), 17 beta-estradiol (E2), 17 alpha-ethynylestradiol (EE2) and estriol (E3)) under UVA and UVC radiation: Photon absorption, quantum yields and rate constants independent of photon absorption. *Appl. Catal. B-Environ.* 99(3-4), 388-397.
- Quevedo, I.R. and Tufenkji, N., 2012. Mobility of functionalized quantum dots and a model polystyrene nanoparticle in saturated quartz sand and loamy sand. *Environ. Sci. Technol.* 46(8), 4449-4457.
- Rao, P.S.C., Lee, L.S. and Pinal, R., 1990. Cosolvency and sorption of hydrophobic organic-chemicals. *Environ. Sci. Technol.* 24(5), 647-654.
- Rivera-Utrilla, J., Sanchez-Polo, M., Angeles Ferro-Garcia, M., Prados-Joya, G. and Ocampo-Perez, R., 2013. Pharmaceuticals as emerging contaminants and their removal from water. A review. *Chemosphere* 93(7), 1268-1287.

- Pizarro, A.H., Molina, C.B., Casas, J.A. and Rodriguez, J.J., 2014. Catalytic HDC/HDN of 4-chloronitrobenzene in water under ambient-like conditions with Pd supported on pillared clay. *Appl. Catal. B-Environ.* 158, 175-181.
- Rizwan, T. and Bhattacharjee, S., 2009. Particle deposition onto charge-heterogeneous substrates. *Langmuir* 25(9), 4907-4918.
- Rosal, R., Rodriguez, A., Perdigon-Melon, J.A., Mezcua, M., Hernando, M.D., Leton, P., Garcia-Calvo, E., Aguera, A. and Fernandez-Alba, A.R., 2008. Removal of pharmaceuticals and kinetics of mineralization by O₃/H₂O₂ in a biotreated municipal wastewater. *Water Res.* 42(14), 3719-3728.
- Rosenfeldt, E.J. and Linden, K.G., 2004. Degradation of endocrine disrupting chemicals bisphenol a, ethinyl estradiol, and estradiol during UV photolysis and advanced oxidation processes. *Environ. Sci. Technol.* 38(20), 5476-5483.
- Rubert, K.F. and Pedersen, J.A., 2006. Kinetics of oxytetracycline reaction with a hydrous manganese oxide. *Environ. Sci. Technol.* 40(23), 7216-7221.
- Rule, K.L., Ebbett, V.R. and Vikesland, P.J., 2005. Formation of chloroform and chlorinated organics by free-chlorine-mediated oxidation of triclosan. *Environ. Sci. Technol.* 39(9), 3176-3185.
- Ryan, C.C., Tan, D.T. and Arnold, W.A., 2011. Direct and indirect photolysis of sulfamethoxazole and trimethoprim in wastewater treatment plant effluent. *Water Res.* 45(3), 1280-1286.
- Sakulchaicharoen, N., O'Carroll, D.M. and Herrera, J.E., 2010. Enhanced stability and dechlorination activity of pre-synthesis stabilized nanoscale fepd particles. *J. Contam. Hydrol.* 118(3-4), 117-127.

- Sasidharan, S., Torkzaban, S., Bradford, S.A., Dillon, P.J. and Cook, P.G., 2014. Coupled effects of hydrodynamic and solution chemistry on long-term nanoparticle transport and deposition in saturated porous media. *Colloid. Surface. A* 457, 169-179.
- SCCS Scientific Committee on Consumer Safety, 2010. Opinion on: Triclosan antimicrobial, resistance (SCCP/1251/09). Adopted by the SCCP during the 7th plenary on 22 June 2010.
- Schouten, N., van der Ham, L.G.J., Euverink, G.-J.W. and de Haan, A.B., 2007. Selection and evaluation of adsorbents for the removal of anionic surfactants from laundry rinsing water. *Water Res.* 41(18), 4233-4241.
- Schuth, C. and Reinhard, M., 1998. Hydrodechlorination and hydrogenation of aromatic compounds over palladium on alumina in hydrogen-saturated water. *Appl. Catal. B-Environ.* 18(3-4), 215-221.
- Sheng, G.D., Xu, C., Xu, L., Qiu, Y.P. and Zhou, H.Y., 2009. Abiotic oxidation of 17 beta-estradiol by soil manganese oxides. *Environ. Pollut.* 157(10), 2710-2715.
- Shore, L.S. and Shemesh, M., 2003. Naturally produced steroid hormones and their release into the environment. *Pure Appl. Chem.* 75(11-12), 1859-1871.
- Simunek, J., and van Genuchten, M. Th., 1995. Numerical model for simulating multiple solute transport in variably-saturated soils, *Proc. Water Pollution III: Modelling, Measurement, and Prediction*, Ed. L. C. Wrobel and P. Latinopoulos, Computation Mechanics Publication, Ashurst Lodge, Ashurst, Southampton, UK, 21-30.
- Simunek, J., van Genuchten, M.Th. and Sejna, M., 2005. The HYDRUS-1D software package for simulating the one-dimensional movement of water, heat, and multiple solutes in variably-saturated media-version 3.0, HYDRUS software series,

- Department of Environmental Sciences, University of California Riverside,
Riverside, CA. 240 pp.
- Srebowata, A., Baran, R., Casale, S., Kaminska, I.I., Lomot, D., Lisovytskiy, D. and Dzwigaj, S., 2014. Catalytic conversion of 1,2-dichloroethane over bimetallic Cu-Ni loaded BEA zeolites. *Appl. Catal. B-Environ.* 152, 317-327.
- Stefanescu, D.M., Khoshnan, A., Patterson, P.H. and Hering, J.G., 2009. Manganese Oxide nanoparticles are toxic to neuronal precursor cells. *J. Nanopart. Res.* 11,1957-1969.
- Stevenson, F.J., 1994. *Humus chemistry: Genesis, composition, reactions.* Wiley: New York, New York.
- Stuart, M., Lapworth, D., Crane, E. and Hart, A., 2012. Review of risk from potential emerging contaminants in UK groundwater. *Sci. Total Environ.* 416, 1-21.
- Stumm, W. and Morgan, J.J., 1996. *Aquatic chemistry*, 3rd ed., Wiley: New York, New York.
- Su, C., Puls, R.W., Krug, T.A., Watling, M.T., O'Hara, S.K., Quinn, J.W. and Ruiz, N.E., 2012. A two and half-year-performance evaluation of a field test on treatment of source zone tetrachloroethene and its chlorinated daughter products using emulsified zero valent iron nanoparticles. *Water Res.* 46(16), 5071-5084.
- Sun, Z., Takahashi, F., Odaka, Y., Fukushi, K., Oshima, Y. and Yamamoto, K., 2007. Effects of potassium alkalis and sodium alkalis on the dechlorination of o-chlorophenol in supercritical water. *Chemosphere* 66(1), 151-157.
- Tabata, A., Kashiwada, S., Ohnishi, Y., Ishikawa, H., Miyamoto, N., Itoh, M. and Magara, Y., 2001. Estrogenic influences of estradiol-17 beta, p-nonylphenol and bis-

- phenol-A on japanese medaka (*oryzias latipes*) at detected environmental concentrations. *Water Sci. Technol.* 43(2), 109-116.
- Ternes, T.A., Stumpf, M., Mueller, J., Haberer, K., Wilken, R.D. and Servos, M., 1999. Behavior and occurrence of estrogens in municipal sewage treatment plants - i. Investigations in germany, canada and brazil. *Sci. Total Environ.* 225(1-2), 81-90.
- Torkzaban, S., Kim, Y., Mulvihill, M., Wan, J. and Tokunaga, T.K., 2010. Transport and deposition of functionalized CdTe nanoparticles in saturated porous media. *J. Contam. Hydrol.* 118(3-4), 208-217.
- Veldhoen, N., Skirrow, R.C., Osachoff, H., Wigmore, H., Clapson, D.J., Gunderson, M.P., Van Aggelen, G. and Helbing, C.C., 2006. The bactericidal agent triclosan modulates thyroid hormone-associated gene expression and disrupts postembryonic anuran development. *Aquat. Toxicol.* 80(3), 217-227.
- Wang, Y.G., Li, Y.S., Costanza, J., Abriola, L.M. and Pennell, K.D, 2012. Enhanced mobility of fullerene (C-60) nanoparticles in the presence of stabilizing agents. *Environ. Sci. Technol.* 46(21), 11761-11769.
- Wang, Y.G., Li, Y.S., Fortner, J.D., Hughes, J.B., Abriola, L.M. and Pennell, K.D., 2008. Transport and retention of nanoscale C60 aggregates in water-saturated porous media. *Environ. Sci. Technol.* 42(10), 3588-3594.
- Weber, W.J., Jr.2001. *Environmental systems and processes: Principles, modeling, and design*, Wiley-Interscience, New York.
- Wei, Y.T., Wu, S.C., Chou, C.M., Che, C.H., Tsai, S.M. and Lien, H.L., 2010. Influence of nanoscale zero-valent iron on geochemical properties of groundwater and vinyl chloride degradation: A field case study. *Water Res.* 44(1), 131-140.

- Winkler, G., Fischer, R., Krebs, P., Thompson, A. and Cartmell, E., 2007. Mass flow balances of triclosan in rural wastewater treatment plants and the impact of biomass parameters on the removal. *Eng. Life Sci.* 7(1), 42-51.
- Xiong, Z., He, F., Zhao, D.Y. and Barnett, M.O., 2009. Immobilization of mercury in sediment using stabilized iron sulfide nanoparticles. *Water Res.* 43(20), 5171-5179.
- Xiong, Z., Zhao, D. and Harper, W.F., Jr., 2007. Sorption and desorption of perchlorate with various classes of ion exchangers: A comparative study. *Ind. Eng. Chem. Res.* 46(26), 9213-9222.
- Xu, L., Xu, C., Zhao, M.R., Qiu, Y.P. and Sheng, G.D., 2008. Oxidative removal of aqueous steroid estrogens by manganese oxides. *Water Res.* 42(20), 5038-5044.
- Yoshihara, S., Murugananthan, M., 2009. Decomposition of various endocrine disrupting chemicals at boron-doped diamond electrode. *Electrochim. Acta* 54, 2031–2038.
- Yu ,J.T., Bouwer, E.J. and Coelhan, M., 2006. Occurrence and biodegradability studies of selected pharmaceuticals and personal care products in sewage effluent. *Agric. Water Manag.* 86,72–80.
- Yuan, G. and Keane, M.A., 2003. Catalyst deactivation during the liquid phase hydrodechlorination of 2,4-dichlorophenol over supported Pd: influence of the support. *Catal. Today* 88(1-2), 27-36.
- Yuan, G. and Keane, M.A., 2004. Liquid phase hydrodechlorination of chlorophenols over Pd/C and Pd/Al₂O₃: a consideration of HCl/catalyst interactions and solution pH effects. *Appl. Catal. B-Environ.* 52(4), 301-314.
- Zecca, M., Kralik, M., Boaro, M., Palma, G., Lora, S., Zancato, M. and Corain, B., 1998. Metal palladium supported on amphiphilic microporous synthetic organic supports.

- Part I. Material preparation and textural characterization. *J. Mol. Catal. A-Chem.* 129(1), 27-34.
- Zhang, M., Bacik, D.B., Roberts, C.B. and Zhao, D.Y., 2013. Catalytic hydrodechlorination of trichloroethylene in water with supported CMC-stabilized palladium nanoparticles. *Water Res.* 47(11), 3706-3715.
- Zhang, H.C. and Huang, C.H., 2003. Oxidative transformation of triclosan and chlorophene by manganese oxides. *Environ. Sci. Technol.* 37(11), 2421-2430.
- Zhang, M., He, F., Zhao, D.Y. and Hao, X.D., 2011. Degradation of soil-sorbed trichloroethylene by stabilized zero valent iron nanoparticles: Effects of sorption, surfactants, and natural organic matter. *Water Res.* 45(7), 2401-2414.
- Zhang, M. and Zhao D.Y., 2013. In situ dechlorination in soil and groundwater using stabilized zero-valent iron nanoparticles: Some field experience on effectiveness and limitations. *Novel Solutions to Water Pollution, Chapter 6, ACS Symposium Series*, 1123, 79-96.
- Zhou, J., Han, Y., Wang, W., Xu, Z., Wan, H., Yin, D., Zheng, S. and Zhu, D., 2013. Reductive removal of chloroacetic acids by catalytic hydrodechlorination over Pd/ZrO₂ catalysts. *Appl. Catal. B-Environ.* 134, 222-230.
- Zhu, B.W., Lim, T.T. and Feng, J., 2008. Influences of amphiphiles on dechlorination of a trichlorobenzene by nanoscale Pd/Fe: Adsorption, reaction kinetics, and interfacial interactions. *Environ. Sci. Technol.* 42(12), 4513-4519.

APPENDIX A. HYDRUS-1D model for nanoparticle transport simulation

For the nonequilibrium transport of solutes involved problem, there are two key modules need to be set up by users in HYDRUS-1D. The first one is the water flow module, and the second one which is also the most important is the solute transport module.

The water flow module requires the porous media properties parameters (such as porosity and hydraulic conductivity), water flow condition of the experiment (such as boundary flow condition and flow velocity), and the numerical calculation parameters (such as iteration criteria and time step control). The default values of numerical calculation parameters were used in this work, and porosity and hydraulic conductivity was measured and entered by user. The boundary conditions were chosen according to experiment conditions, and in this work constant flux was set for both upper and lower boundary conditions.

In the solute transport module, there are one equilibrium model and five non-equilibrium models were given in this software. In this work two kinetic sites model for particle transport using attachment/detachment was being used. The two kinetic sites of convection-dispersion equation was as below (Wang et al., 2008; Simunek et al., 2005;):

$$\frac{\partial C}{\partial t} = \lambda v_p \frac{\partial^2 C}{\partial z^2} - v_p \frac{\partial C}{\partial z} - \frac{\rho_b}{\theta_w} \left(\frac{\partial S_1}{\partial t} + \frac{\partial S_2}{\partial t} \right) - \mu_w \theta C - \mu_s \rho (S_1 + S_2) \quad (\text{A-1})$$

where C is the particle concentration in the aqueous phase ($\text{N}_c \text{L}^{-3}$), S is the particle concentration in the solid phase ($\text{N}_c \text{M}^{-1}$), subscripts 1 and 2 represent two kinetic sorption sites, respectively, N_c is the number of particles, M is the mass of solid phase, z (L^{-1}) is

the distance along the column from the inlet, t is the time (T), λ is the dispersivity (L), v_p is the average pore velocity (LT⁻¹), ρ_b is the porous media bulk density (ML⁻³), θ_w is the water content, which is equal to porosity under saturation condition, and μ_w (T⁻¹) and μ_s (T⁻¹) are first-order degradation coefficients in the liquid and solid phases, respectively (Simunek et al., 2005).

For this work, as MnO₂ nanoparticle could not diminish due to inactivation and degradation, thus μ_w and μ_s are equal to zero. Note there is much fewer sites of soil could be instantaneous sorption (site 1) by MnO₂ nanoparticles compared to a kinetic sorption (site 2), the two kinetic sites model was reduced to one site model. Thus, the Eqn A-1 is reduced to Eqn A-2:

$$\frac{\partial C}{\partial t} = \lambda v_p \frac{\partial^2 C}{\partial z^2} - v_p \frac{\partial C}{\partial z} - \frac{\rho_b}{\theta_w} \frac{\partial S}{\partial t} \quad (\text{A-2})$$

Set “Frac”=0 in the solute transport and reaction parameter to turn off the instantaneous sorption site, and set “SinkWater”=0 and “SinkSolid”=0 to turn off the inactivation and degradation term.

Particle mass transfer between the aqueous and solid phases can be described as (Bolster et al., 1999):

$$\frac{\rho_b}{\theta_w} \frac{\partial S}{\partial t} = k_{dep} \psi C - \frac{\rho_b}{\theta_w} k_{det} S \quad (\text{A-3})$$

where k_{dep} is the first-order deposition coefficient of CMC-MnO₂ [T⁻¹], k_{det} is first-order detachment coefficient [T⁻¹], and ψ is a dimensionless blocking function to describe the change of the available fraction of deposition surface sites.

In this work, as the BTCs are showed almost no tailing, which indicate a negligible detachment of the particle from the soil. As a result, k_{det} was set to zero.

A simple Langmuirian blocking function, which was derived from the Langmuir adsorption model, was used to account for the dynamic blocking (Adamczyk et al., 1994):

$$\psi = \frac{S_{max}-S}{S_{max}} \quad (\text{A-4})$$

where S_{max} is the maximum MnO_2 deposition capacity [N_cM^{-1}].

Substitute Eqn. A-4 to A-3, we get:

$$\frac{\rho_b}{\theta_w} \frac{\partial S}{\partial t} = k_{dep} \left(\frac{S_{max}-S}{S_{max}} \right) C - \frac{\rho_b}{\theta_w} k_{det} S \quad (\text{A-5})$$

The HYDRUS-1D code was used to solve Eqs. (A-2) and (A-5). In these two equations, dispersivity λ was obtained by fitting tracer BTCs using an equilibrium model. Therefore, there are only two parameters, deposition coefficient k_{dep} and maximum MnO_2 deposition capacity S_{max} , which need to be predict by model fitting. In the software, the two parameters are “DetachSolid” and “SMax” shown in solute transport and reaction parameters. Upon choosing fitting these two parameters, HYDRUS-1D would predict the two parameters by fitting the experiment data to this model.